PNPLA3^{I148M}-Associated MASLD Susceptibility: The Pivotal Role of Microbiota-Driven Metabolic Dysregulation

Von der Fakultät für Mathematik und Naturwissenschaften der RWTH Aachen University zur Erlangung des akademischen Grades einer Doktorin der Naturwissenschaften genehmigte Dissertation

vorgelegt von

Madhuri Haque, M.Sc.

aus Dhaka, Bangladesch

Berichter:

Universitätsprofessor Dr. Lars Blank

Universitätsprofessor Dr. med. Dr. rer. nat. Kai Markus Schneider

Tag der mündlichen Prüfung: 04. Dezember 2025

To my beloved family —

For every silent sacrifice you made,
every doubt you helped me evade,
every page your love engraved.

This story is ours. ♥

TABLE OF CONTENTS

LIST OF ABBREVIATIONS

12α-OH	12α-hydroxylated bile acids
16S rRNA	16S ribosomal RNA
AB	Antibiotic
AB-PAS	Alcian blue-periodic acid-schiff
Aacs	Acetoacetyl-CoA synthetase
Akk	*Akkermansia muciniphila*
ALD	Alcohol-associated liver disease
ALT	Alanine aminotransferase
Amuc_1100	Outer membrane protein of *Akkermansia muciniphila*
ANOVA	Analysis of variance
AUC	Area under the curve
BAT	Brown adipose tissue
BMI	Body mass index
bp	Base pair
BSA	Bovine serum albumin
BSH	Bile salt hydrolase
CD	Cluster of differentiation (e.g., CD4, CD8, CD11b, CD45)
CDCA	Chenodeoxycholic acid
cDNA	Complementary DNA
CerS6	Ceramide synthase 6
Ces1d	Carboxylesterase 1D
CFU	Colony-forming units
CHOW	Standard laboratory diet
Col1a	Collagen type 1 alpha
Cyp27a1	Sterol 27-hydroxylase
Cyp7a1	Cholesterol 7α-hydroxylase
DCA	Deoxycholic acid
DEPC	Diethylpyrocarbonate

dFMT	Dysbiotic fecal microbiota transplantation
DTT	Dithiothreitol
ECL	Enhanced chemiluminescence
EDTA	Ethylenediaminetetraacetic acid
Fabp4	Fatty acid-binding protein 4
eFMT	Eubiotic fecal microbiota transplantation
F4/80	Macrophage marker
FACS	Fluorescence-activated cell sorting
FFA	Free fatty acids
FGF15	Fibroblast growth factor 15
FISH	Fluorescent in situ hybridization
FITC	Fluorescein isothiocyanate
FMT	Fecal microbiota transplantation
FSC	Forward scatter
FXR	Farnesoid X receptor
GCA	Glycocholic acid
H&E	Hematoxylin and eosin
HCC	Hepatocellular carcinoma
HDL	High-density lipoprotein
HFD	High-fat diet
IL-1β	Interleukin-1 beta
IL-6	Interleukin-6
LDL	Low-density lipoprotein
Ly6C/G	Lymphocyte antigen 6 complex
MAGs	Metagenome-assembled genomes
MASH	Metabolic dysfunction-associated steatohepatitis
MASLD	Metabolic dysfunction-associated steatotic liver disease
MRM	Multiple reaction monitoring
MTBE	Methyl tert-butyl ether

MUFA	Monounsaturated fatty acids
Nlrp6$^{-/-}$	NOD-like receptor family pyrin domain-containing 6 knockout
OGTT	Oral glucose tolerance test
ORO	Oil Red O
PBS	Phosphate-buffered saline
PCoA	Principal coordinate analysis
PCR	Polymerase chain reaction
PERMANOVA	Permutational multivariate analysis of variance
PNPLA3/Pnpla3	Patatin-like phospholipase domain-containing protein 3
PNPLA3$^{I148M/}$ Pnpla3^{I148M}	PNPLA3 variant (isoleucine to methionine at position 148)
PPAR	Peroxisome proliferator-activated receptor
PUFA	Polyunsaturated fatty acids
qPCR	Quantitative real-time polymerase chain reaction
rcf	Relative centrifugal force (×g)
RIN	RNA integrity number
ROS	Reactive oxygen species
rpm	Revolutions per minute
SDS	Sodium dodecyl sulfate
SR	Sirius red
SSC	Side scatter
TAE	Tris-acetate-EDTA
TBS	Tris-buffered saline
TBST	TBS with Tween-20
TCA	Taurocholic acid
TCDCA	Taurochenodeoxycholic acid
TDCA	Taurodeoxycholic acid
TG	Triglyceride

TLCA	Taurolithocholic acid
TMAO	Trimethylamine N-oxide
TNFα	Tumor necrosis factor alpha
TPM	Transcripts per million
Ucp2	Uncoupling protein 2
UPLC-MS/MS	Ultra-performance liquid chromatography-tandem mass spectrometry
VLDL	Very low-density lipoprotein
WAT	White adipose tissue
WB	Western blot
WT	Wild-type
ZO-1	Zonula occludens-1
zOTUs	Zero-radius operational taxonomic units
αSMA	Alpha smooth muscle actin
β-oxidation	Mitochondrial fatty acid oxidation
ω-3 fatty acids	Omega-3 fatty acids

LIST OF FIGURES

LIST OF TABLES

ZUSAMMENFASSUNG

Die genetische Variante *PNPLA3*^{I148M} gilt als bedeutender Risikofaktor für MASLD (metabolisch assoziierte Steatose-Lebererkrankung), weist jedoch eine variable Penetranz auf, was auf zusätzliche Umweltfaktoren hinweist. Eine intestinale Dysbiose wird zunehmend mit der Pathogenese von MASLD in Verbindung gebracht, doch die Wechselwirkung zwischen *PNPLA3*^{I148M} und mikrobieller Fehlbesiedlung ist bislang nicht vollständig verstanden. Ziel dieser Arbeit war es, die synergistische Wirkung von *PNPLA3*^{I148M} und Darmdysbiose auf die metabolische Gesundheit und die Progression von MASLD zu untersuchen. Dafür wurden zunächst Mikrobiomprofile von 146 MASLD-Patientinnen analysiert. Ergänzend wurde ein murines ‘Dual-Hit’-Modell etabliert, das *Pnpla3*^{I148M} mit einem *Nlrp6*-Mangel kombiniert. Die Tiere erhielten entweder eine Standard- oder fettreiche Diät und wurden umfassend metabolisch, mikrobiell und lipidomisch charakterisiert. Therapeutische Interventionen umfassten eine Antibiotikabehandlung, fäkale Mikrobiota-Transplantationen sowie die Supplementierung mit *Akkermansia muciniphila* bzw. dem Oberflächenprotein Amuc_1100. Die Ergebnisse zeigen, dass bei *PNPLA3*^{I148M}-Trägerinnen eine adipositasabhängige Dysbiose mit erhöhten Triglyzeridwerten assoziiert ist. Im Mausmodell führte die Kombination aus *Pnpla3*^{I148M} und *Nlrp6*-Defizienz selbst unter Normaldiät zu einer spontanen MASLD, begleitet von Darmbarrierestörung, Dysbiose, mitochondrialer Dysfunktion und gestörter Lipidhomöostase. Die Anreicherung gallensäuremetabolisierender und ceramidproduzierender Bakterien resultierte in einer metabolischen Reprogrammierung der Leber über die Darm-Leber-Achse. Therapeutische Modulationen, insbesondere eine vollständige Mikrobiom-Wiederherstellung, verbesserten die metabolische Gesundheit signifikant. Diese Arbeit zeigt, dass *PNPLA3*^{I148M} und Darmdysbiose gemeinsam als pathogene Treiber von MASLD wirken. Die gezielte mikrobielle Intervention stellt einen vielversprechenden Ansatz für die Präzisionsmedizin bei genetisch vorbelasteten Risikopersonen dar.

ABSTRACT

Rationale:

The *PNPLA3*^{I148M} variant is a major genetic risk factor for MASLD, yet its variable penetrance suggests additional environmental triggers. Gut microbial dysbiosis is implicated in MASLD pathogenesis, yet its interaction with *PNPLA3*^{I148M} remains uncertain. This study explores how dysbiosis synergizes with *PNPLA3*^{I148M} to drive metabolic dysfunction and MASLD progression.

Methods:

Gut microbiota profiles from 146 MASLD patients were analyzed. To mechanistically model the gene-diet-microbiome interaction, a murine "dual-hit" model combining *Pnpla3*^{I148M} and *Nlrp6* deficiency was developed. Mice were fed a CHOW or HFD, and subsequently subjected to metabolic, lipidomic, and microbial profiling. Interventions included antibiotic treatment, fecal microbiota transplantation, and *Akkermansia muciniphila* supplementation.

Results:

In MASLD patients, gut dysbiosis significantly correlated with metabolic variance in *PNPLA3*^{I148M}-carriers, manifesting as an adiposity-dependent rise in serum triglycerides. In mice, *Pnpla3*^{I148M} alone caused mild steatosis under obesogenic conditions, whereas combined with *Nlrp6* deficiency it induced spontaneous MASLD even on CHOW diet, worsened by HFD. This phenotype featured gut barrier dysfunction, dysbiosis, hepatic lipid remodeling, and mitochondrial impairment. Mechanistically, dysbiosis enriched bile acid-transforming and ceramide-producing bacteria signature (e.g., *Clostridium scindens*, *Alistipes finegoldii*, *Oscillibacter*), elevating hydrophobic secondary bile acids and ceramides in portal circulation. These metabolites impaired hepatic mitochondrial oxidative phosphorylation, increased ROS, suppressed bile acid synthesis (*Cyp7a1*, *Cyp27a1*), and activated lipid uptake pathways (*Srebf2*/*Ldlr*, *Cd36*). Upregulation of ceramide synthase 6 (*CerS6*) and lipid droplet stabilizers (*Plin2*, *Lipa*) promoted intracellular lipid retention, establishing a self-amplifying gut–liver metabolic loop. Antibiotic depletion

disrupted this axis, reversing metabolic dysfunction. Dysbiotic FMT transferred pathology to healthy mice, while complete microbiome restoration robustly improved metabolic health; single-strain *Akkermansia* treatment was partially effective.

Conclusion:

My findings establish *PNPLA3*^{I148M} and dysbiosis as synergistic drivers of MASLD, with microbial dysregulation exacerbating genetic susceptibility through gut-liver axis disruption. Therapeutic modulation of the microbiome may offer a targeted strategy for high-risk *PNPLA3*^{I148M}-carriers.

THE LIVER-GUT-MICROBIOTA AXIS IN METABOLIC REGULATION

The liver acts as the central hub of the body’s metabolic processes, regulating nutrient processing, energy storage, and detoxification of harmful substances. Its unique anatomical and functional connection to the gastrointestinal tract via portal vein establishes a tightly regulated and bidirectional communication system, known as the gut-liver axis.

Blood from the gastrointestinal tract, enriched with nutrients, microbial metabolites, and potentially harmful substances, is directed to the liver through the portal vein. This allows the liver to serve as the first line of defense, filtering and processing substances absorbed from the gut before they reach systemic circulation. Hepatocytes (the liver's primary functional cells) metabolize nutrients, convert toxins into less harmful forms, and produce bile acids, which are secreted into the bile ducts and stored in the gallbladder. Upon food intake, bile is released into the intestine to aid in the emulsification and absorption of dietary fats.

In return, bile acids and other hepatically derived molecules exert significant effects on the gut environment. They shape the composition and function of the gut microbiota and help maintain the integrity of the intestinal barrier. This barrier, formed by epithelial cells and a protective mucus layer, prevents the translocation of pathogens and toxins into circulation while allowing selective absorption of nutrients.

Integral to this axis is the gut microbiota-the vast community of microbes that metabolize indigestible fibers, produce beneficial metabolites, and help maintain metabolic homeostasis. Together, the liver, gut, and microbiota form a tightly coordinated network that influences digestion, nutrient absorption, immune function, and overall metabolic health (Figure 1), with disruptions in this axis linked to conditions like metabolic syndrome and liver disease.

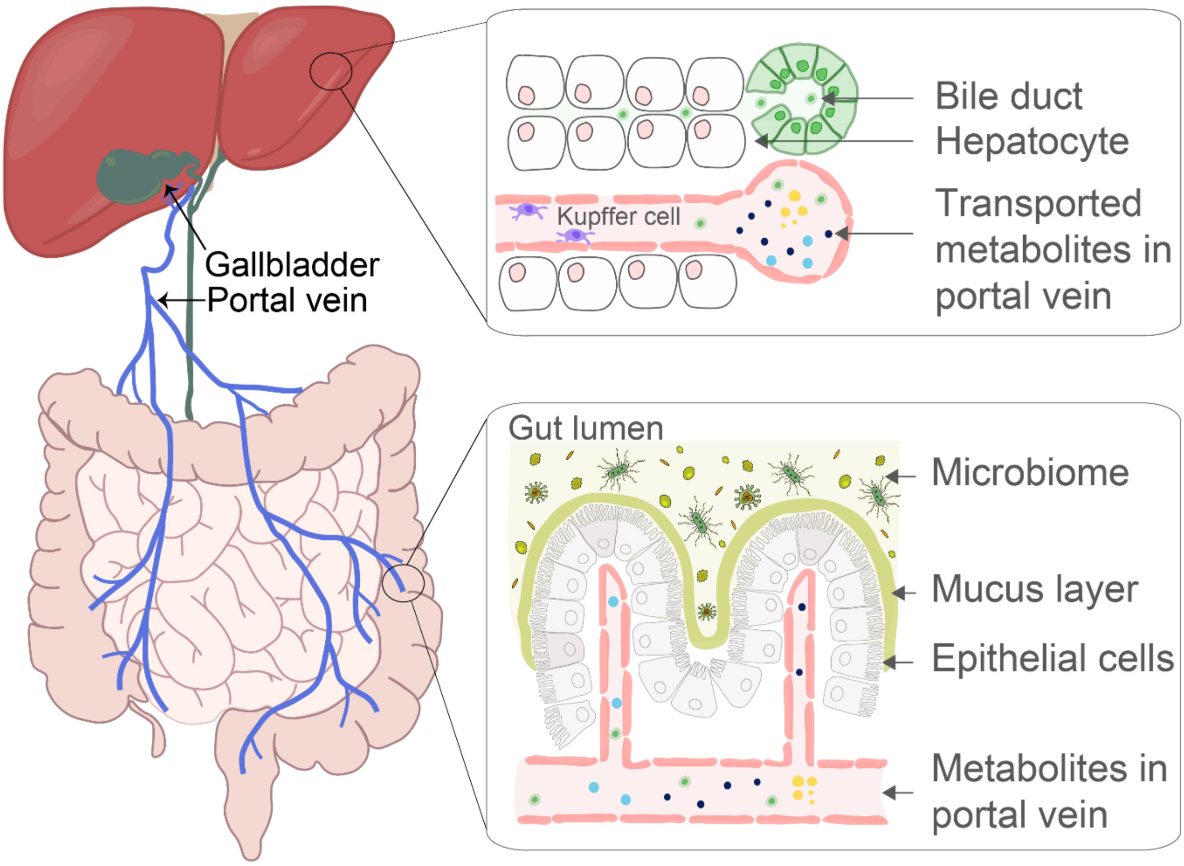

Figure 1: Bidirectional metabolic communication in the liver-gut-microbiota axis. The gut lumen harbors a complex microbiota, releasing metabolites into the portal circulation. The portal vein transports microbial metabolites, nutrients, and potential toxins from the gut lumen to the liver. Within the liver, hepatocytes process these substances, while bile is secreted back into the gut to aid in digestion. This bidirectional crosstalk underpins metabolic homeostasis, detoxification, and immune regulation.

1. INTRODUCTION

1.1. Hepatic metabolic regulation: central role in systemic homeostasis

The liver serves as the body's metabolic command center, with hepatocytes, its primary functional units, executes four vital functions: (1) detoxification of xenobiotics and metabolic byproducts, (2) precise regulation of carbohydrate, lipid, and protein metabolism, (3) immunomodulation, and (4) synthesis of plasma proteins [1]. These key functions enable the liver to maintain systemic homeostasis while dynamically adapting to nutritional, toxicological, and immunological challenges - a capacity critical for survival during feast-famine cycles and pathogen exposure [2].

As the central regulator of lipid metabolism, the liver acts as the principal regulatory hub for maintaining cholesterol homeostasis through the synthesis and catabolism of lipoproteins [3]. It also processes fatty acids, partitioning them between mitochondrial β-oxidation for energy production and esterification into triglycerides for storage when energy demands are low [4, 5]. Notably, the liver's role in triglycerides handling is particularly crucial as it serves as both the primary site of synthesis and the central distributor, allowing peripheral tissues to either utilize them as immediate energy sources or store them in adipose tissue [6, 7]. The liver also supports lipid metabolism by producing bile from cholesterol, a crucial digestive fluid stored in the gallbladder and secreted into the duodenum, where it emulsifies dietary fats and enhances their digestion and absorption [8].

The liver's metabolic processes exhibit remarkable adaptability to nutritional status. During fasting states, it coordinates the mobilization of adipose-derived fatty acids for hepatic energy production, while postprandial insulin signaling promotes lipid storage in both hepatocytes and adipocytes [9, 10]. This bidirectional regulation ensures energy homeostasis across fluctuating metabolic demands.

1.2. Hepatic metabolic dysfunction: global epidemiological shifts and pathophysiological consequences

Given the multifaceted role of liver in metabolic regulation, its dysfunction has far-reaching consequences, accounting for approximately 2 million annual deaths worldwide (representing 4% of global mortality) [11]. The past three decades have witnessed a dramatic epidemiological transition in liver disease etiology. Where viral hepatitis once accounted for most liver-related morbidity, its burden has now become concentrated in resource-limited regions of Africa and Asia where healthcare access remains challenging [12]. In contrast, metabolic dysfunction-associated steatotic liver disease (MASLD) and alcohol-associated liver disease (ALD) have emerged as the leading causes of chronic liver disease globally [13, 14]. This shift is most pronounced in industrialized nations, such as the United States, where a threefold increase in obesity-related liver disease incidence occurred between 1988-2016, paralleling the worldwide rise in metabolic syndrome [15].

This epidemiological shift reflects four interconnected societal changes: (1) urbanization and sedentary lifestyles driving obesity epidemics and glucose intolerance; (2) widespread consumption of processed diets high in sugar and saturated fats, promoting hepatic lipid accumulation; (3) the normalization of alcohol consumption as a mainstream form of social activity; and (4) aging populations with accumulating metabolic comorbidities, which accelerate liver disease progression [16, 17, 18, 19]. These factors have contributed to the rise of metabolic liver diseases, making them one of the most important public health challenges today [20]. The liver's central role at the crossroads of metabolism and inflammation makes it particularly vulnerable to these modern lifestyle factors, while simultaneously amplifying their systemic consequences [21, 22].

1.3. Metabolic dysfunction-associated steatotic liver disease (MASLD): epidemiology, pathogenesis, and clinical progression

Metabolic Dysfunction-Associated Steatotic Liver Disease (MASLD) has rapidly emerged as a major global health concern, now affecting nearly 30% of adults worldwide, a prevalence that parallels the rising epidemics of obesity and type 2 diabetes [23, 24]. Characterized by hepatic steatosis (fat accumulation in the liver) in the setting of metabolic dysfunction, MASLD represents a spectrum of liver disorders that can progress to more severe conditions, including Metabolic Dysfunction-Associated Steatohepatitis (MASH), fibrosis, and cirrhosis, ultimately leading to hepatocellular carcinoma (HCC) or liver failure [25, 26] (Figure 2). The rising fatalities from MASLD are alarming, with an estimated 280,000 deaths globally in 2019 alone, making it one of the fastest-growing causes of liver-related mortality [27, 28]. Due to its escalating prevalence and severe outcomes, MASLD is projected to surpass viral hepatitis as the leading cause of liver transplantation by 2030 [29, 30].

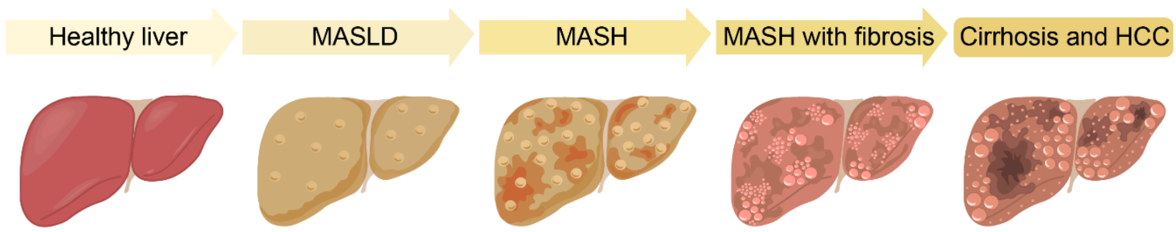

Figure 2: Sequential progression of liver pathology from MASLD to cirrhosis. The spectrum begins with MASLD (>5% hepatic steatosis), progressing to MASH (steatohepatitis with inflammation and mild fibrosis). As fibrosis advances, extensive scarring develops, and progression to cirrhosis represents the end-stage of chronic liver disease, characterized by architectural distortion and impaired liver function.

According to current guidelines, MASLD is diagnosed when hepatic steatosis (detected via imaging or biopsy) coexists with at least one of five cardiometabolic risk factors: overweight or obesity, dysglycaemia or type 2 diabetes, blood pressure, plasma triglycerides or HDL-cholesterol [31] (Figure 3). These metabolic disturbances create a vicious cycle: glucose intolerance promotes lipolysis in adipose tissue, flooding the liver with free fatty acids that drive both steatosis and inflammation [32, 33]. While early-stage MASLD is often asymptomatic, up to 30% of patients develop MASH, where persistent inflammation triggers fibrosis (scarring) [34]. Notably, fibrosis stage, not steatosis severity, is the strongest predictor of liver-related mortality, emphasizing the need for early detection [35].

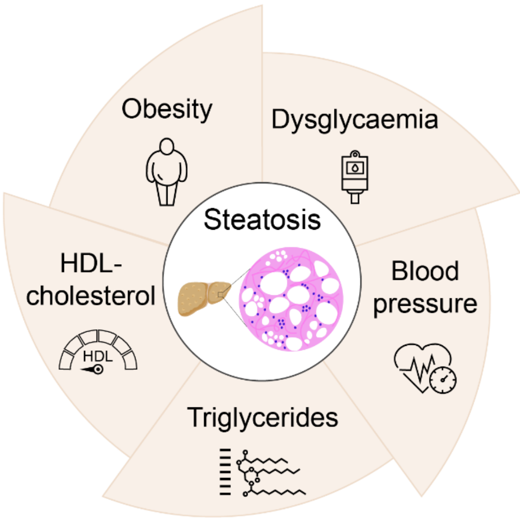

Figure 3: Clinical criteria for MASLD diagnosis based on hepatic steatosis and cardiometabolic risk factors.

1.4. Genetic determinants of MASLD: the *PNPLA3*^{I148M} variant and its pathogenic mechanisms

Emerging research highlights the heterogeneity of MASLD progression, with genetic risk variants now recognized as pivotal drivers that significantly influence disease severity and trajectory [36]. Among these, the *PNPLA3*^{I148M} variant (rs738409) stands out as the most impactful common genetic determinant of MASLD pathogenesis [36]. Homozygous carriers of this polymorphism exhibit a 2–3-fold increased risk of progressing to hepatic fibrosis compared to non-carriers [37] (Figure 4).

This polymorphism alters the function of patatin-like phospholipase domain-containing protein 3 (PNPLA3), a lipid droplet-associated hydrolase critical for triglyceride metabolism in hepatocytes [38]. While likely evolutionarily conserved for its energy-thrifty benefits during feast-famine cycles, the I148M variant (allele frequency: 23-49% across populations) now paradoxically exacerbates MASLD in obesogenic environments through impaired triglyceride hydrolysis, creating a permissive milieu for lipid accumulation and disease progression [39, 40].

Clinically, this manifests as a striking threshold effect in *PNPLA3*^{I148M} homozygotes: advanced disease typically develops only when metabolic stressors, such as glucose intolerance or hypertriglyceridemia, overwhelm compensatory lipophagy [41]. This explains why 17% of lean homozygous carriers still progress to cirrhosis, while 38% of obese non-carriers remain stable [42, 43]. Such observations underscore that *PNPLA3*^{I148M}-mediated pathogenesis requires synergistic metabolic insults to trigger hepatocellular injury, likely via the accumulation of toxic lipid intermediates and disruption of energy production through mitochondrial β-oxidation [43, 44].

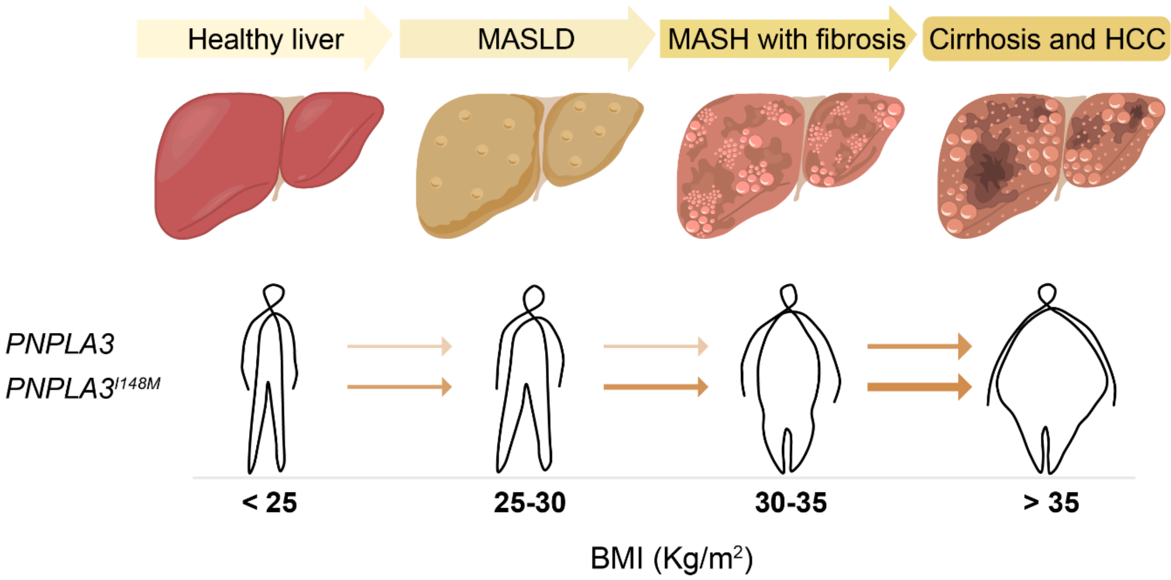

Figure 4: Association between the *PNPLA3*^{I148M} variant and liver disease severity and progression. The genetic contribution to hepatic triglyceride content and the risk of progressive liver disease increases stepwise with rising BMI, as illustrated by the increasing thickness of the brown arrow.

1.5. Gut microbiome dysbiosis and the gut-liver axis in MASLD pathogenesis

Emerging evidence underscores the gut microbiome as a critical modulator of MASLD pathogenesis through the gut-liver axis [45]. Disruptions in the normal balance of gut bacteria (dysbiosis) can contribute to liver fat accumulation and inflammation in several ways. First, harmful bacterial products like endotoxins can trigger liver inflammation by activating immune cells [46]. Second, changes in microbial metabolism affect how the body processes fats and sugars, potentially worsening glucose tolerance [47]. Third, alterations in gut barrier function (leaky gut) may allow bacterial components to reach the liver more easily, further driving disease progression [48].

Research shows that people with MASLD tend to have different gut bacteria compositions compared to healthy individuals, with decreases in beneficial species and increases in potentially harmful ones [45]. These microbial changes appear to correlate with disease severity, suggesting the microbiome could serve as both a contributor to and indicator of MASLD progression [49, 50]. While promising, this area of research still requires further study to fully understand cause-and-effect relationships and to develop effective microbiome-targeted treatments.

1.6. Unresolved mechanistic links: *PNPLA3^{I148M}*, hypertriglyceridemia, and microbial interactions in MASLD progression

Emerging research highlights a potentially critical, yet poorly understood, interaction between the *PNPLA3^{I148M}* genetic variant and gut microbiota in accelerating MASLD progression. While the variant's direct effects on hepatic lipid metabolism are well-established, its potential interplay with gut microbial communities represents a significant knowledge gap. Notably, hypertriglyceridemia, a hallmark metabolic abnormality in both MASLD and *PNPLA3^{I148M}* carriers, may serve as a key modifier in this relationship. Clinical and preclinical studies demonstrate a biangular association where: (1) the *PNPLA3^{I148M}* variant promotes triglyceride accumulation [38], and (2) elevated triglycerides correlate with specific dysbiotic microbial patterns [51].

Despite these associations, critical gaps remain in understanding *PNPLA3^{I148M}*-driven MASLD: (a) how gut microbiota influences *PNPLA3^{I148M}*-associated hypertriglyceridemia to worsen hepatic steatosis, (b) which microbial metabolites are most consequential in genetically susceptible hosts, particularly in promoting inflammation and fibrosis, (c) whether microbiota-directed therapies (such as probiotics or fecal microbiota transplantation) could specifically benefit *PNPLA3^{I148M}* carriers, especially those with concurrent hypertriglyceridemia, a high-risk subgroup. Addressing these gaps could uncover novel precision medicine approaches for MASLD, moving beyond generic metabolic management to strategies that account for both genetic and microbial contributions to disease progression.

2. RATIONALE AND RESEARCH DESIGN

2.1. Theoretical Foundations

The pathogenesis and progression of MASLD can be understood through three interconnected theoretical frameworks that explain how genetic predisposition, metabolic dysregulation, and microbial imbalances disrupt hepatic homeostasis.

First, the “multiple-hit” hypothesis proposes that chronic metabolic stress such as glucose intolerance and hypertriglyceridemia, initiates hepatic steatosis as the “first hit.” This is subsequently compounded by inflammatory, genetic, and environmental insults (“second hits”) that promote fibrosis and cirrhosis [52]. Lipotoxicity plays a central role, as excess free fatty acids from adipose tissue exceed hepatic β-oxidation capacity, leading to the accumulation of toxic intermediates like diacylglycerols and ceramides, ultimately impairing mitochondrial function [53].

Second, the gut-liver axis theory emphasizes the bidirectional communication between gut microbiota and hepatic metabolism [54, 55]. Dysbiosis modulates immunity by depleting beneficial commensals (e.g., *Akkermansia*) and encouraging pathogenic blooms. Increased intestinal permeability (“leaky gut”) further permits the translocation of microbial products into the portal circulation, triggering an inflammatory cascade in the liver marked by elevated TNF-α and IL-6 [56, 57].

Third, the gene-environment interaction model applies the “thrifty genotype” hypothesis to MASLD, suggesting that evolutionarily advantageous traits (e.g., lipid storage via $PNPLA3^{I148M}$) become maladaptive in obesogenic contexts [58, 59]. The effects of this variant are metabolically gated, with high BMI or hypertriglyceridemia unlocking its fibrogenic potential while the microbiome serves as a disease modifier [60, 49]. Importantly, the synergy between genotype and dysbiosis may breach a pathogenic threshold, accelerating progression from steatosis to MASH and fibrosis.

The convergence of these conceptual frameworks establishes *PNPLA3*^{I148M}-associated MASLD as a complex, multifaceted disorder. What makes this particularly intriguing, yet clinically challenging, is the threshold effect observed in carriers of this risk variant. While the genetic predisposition is ever-present, its pathogenic potential often lies dormant until possibly 'triggered' by microbial and metabolic disturbances. This explains why some individuals with the variant develop severe liver disease while others remain unaffected.

The key unresolved question, and perhaps the next frontier in MASLD research, is identifying the precise molecular dialogue between gut-derived signals and genetically susceptible hepatocytes. Unlocking this crosstalk could shift our therapeutic strategies from broad-based management to precision interventions that target the root causes of disease in susceptible individuals.

2.2. Aim of the Study

While *PNPLA3*^{I148M} variant and gut microbiota independently contribute to MASLD pathogenesis, their synergistic interactions, particularly in the context of hypertriglyceridemia, remain poorly characterized. To address this gap, the present study combines MASLD patient data with a novel 'dual-hit' mouse model to:

→ elucidate the tripartite interaction among *PNPLA3*^{I148M}, gut microbial dysbiosis, and hypertriglyceridemia in exacerbating hepatic steatosis, inflammation, and fibrosis

→ identify specific microbial metabolites that modulate disease severity and may serve as mechanistic links between microbiota composition and hepatic injury

→ evaluate the therapeutic potential of microbiota-targeted interventions (e.g., probiotics, restoration of microbial diversity) to attenuate MASLD progression in genetically predisposed hosts, with a particular focus on those with coexisting hypertriglyceridemia.

2.3. Approach

To unravel this intricate interplay between *PNPLA3*^{I148M}–associated genetic susceptibility, gut microbiota, and metabolic dysfunction in MASLD, I employed clinical, translational, and experimental methodologies. This approach was structured around three key pillars.

First, clinical and epidemiological analysis were conducted by leveraging cohorts of biopsy-confirmed MASLD patients, stratified by *PNPLA3*^{I148M} genotype and metabolic parameters such as BMI and triglycerides. Through comprehensive phenotyping, including 16S rRNA sequencing, the modulatory effect of dysbiosis on the variant penetrance in hypertriglyceridemia was explored.

Second, mechanistic investigations were performed using *Pnpla3*^{I148M}*_Nlrp6*$^{-/-}$ mice as a 'dual-hit' model, exposed to obesogenic diets with and without targeted microbiome alterations via antibiotics or dysbiotic fecal microbiota transplant (dFMT) from obesogenic donors. These models enabled profiling of microbial metabolites in the portal circulation and facilitated the investigation of how variant–microbiome interactions promote hepatic lipid accumulation and fibrogenesis.

Finally, the therapeutic potential of beneficial commensal microbes was explored through microbiome-targeted interventions. These included the administration of *Akkermansia muciniphila*-based therapies, which involved either direct supplementation with pasteurized *A. muciniphila* or the use of a purified protein derived from its outer membrane, Amuc_1100. Simultaneously, eubiotic fecal microbiota transplantation (eFMT) was performed using stool samples obtained from healthy donors.

Collectively, this tripartite approach (Figure 5) resolved a fundamental paradox in MASLD pathogenesis: while common genetic variants like *PNPLA3*^{I148M} remain clinically silent under normal metabolic conditions, their pathogenic potential is unmasked by metabolic stressors (e.g., dyslipidemia) through microbiome-mediated mechanisms.

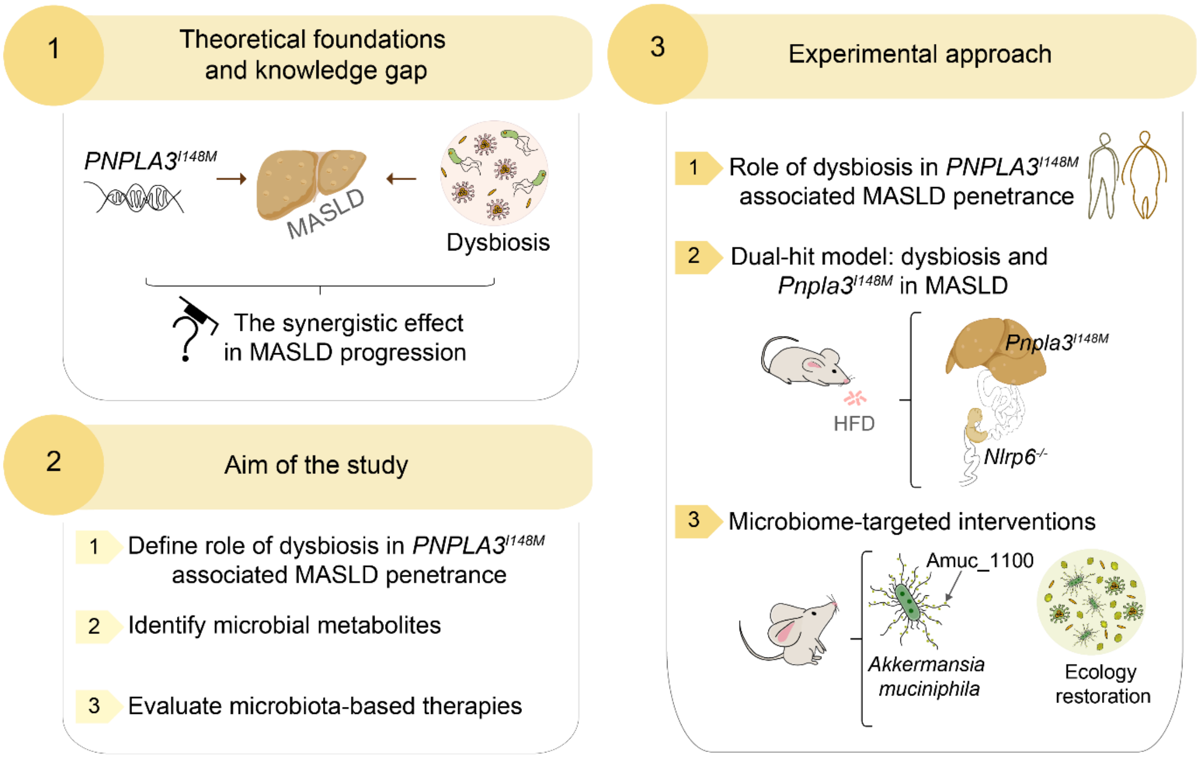

Figure 5: Dissecting the tripartite interplay in MASLD - from theory to therapeutic strategy. A comprehensive experimental framework that integrates genetic predisposition (*PNPLA3*^{I148M}), gut microbial dysbiosis (*Nlrp6*$^{-/-}$), and metabolic stress to address critical knowledge gaps through targeted research objectives and guide experimental interventions in MASLD.

3. MATERIALS AND METHODS

3.1. Standard laboratory equipment and supplies

Routine laboratory consumables

100% Ethanol	17740239, Fisher Scientific
100% Glycerol	6962.5, Roth
100% Isopropanol/2-Propanol	A3465, PanReac AppliChem
Chloroform	133101.1612, PanReac AppliChem
Formaldehyde	27236, Otto Fischar GmbH
Formamide	17899, Thermo Fisher scientific
Glacial acetic acid	131008.1211
H_2O_2	131077.1211, PanReac AppliChem
HCL	4625.1, Roth
Methanol	0082.3, Roth
NaOH	1.09137.1000, Merck
Nuclease-free water (DEPC-treated)	AM9906, Invitrogen
Nuclease-free water (not DEPC-treated)	AM9937, Invitrogen
Xylol	1.08298.4000, VWR

Agencourt AMPure XP, 60 mL	A63881, Beckman Coulter
Bromophenol blue	114391-5G, Merck
BSA	A2153-100G, Sigma-Aldrich
D-sucrose	A3935, PanReac AppliChem
DTT	R0861, Thermo Fisher scientific
EDTA (powder)	A1103, PanReac AppliChem
EDTA (solution)	A4892,0500, PanReac AppliChem
Glycogen	AM9510, Invitrogen
NaCl	A2942,1000, PanReac AppliChem
NaF	S7920, Merck
Ponceau S	A1405,0010, PanReac Applichem
Restore™ western blot stripping-buffer	21059, Thermo Scientific
RNase inhibitor	N8080119, Applied Biosystems
SDS	CN30.3, Roth

Sucrose	4621.1, Roth
Tris	A1379, PanReac AppliChem
Triton™ X-100	X100-100ML, Merck
Tween-20	A4974,0500, PanReac Applichem

1 mL syringe	303172, BD Plastic
1.5 mL eppendorf tube	EP0030120086, Eppendorf
15 mL falcon tube	02-502-8001, Nerbe plus
2 mL eppendorf tube	EP0030120094, Eppendorf
20 mL syringe	4606205V, BRAUN
20G oral gavage needle	18060-20, Fine Science Tools
27G x 3/4” needle	4657705, BRAUN
5 mL eppendorf tube	EP0030119401, Eppendorf
50 mL falcon tube	62.547.254, SARSTEDT
6-well plate	353046, FALCON
70 µm strainer	352350, FALCON
96-well Plate	655101, Greiner
Cover slips (24 x 50 mm)	1871.2, Roth
Cryomolds	4557, Sakura Finetek Europe
Cryo-tubes	375353, Thermo scientific
Eppendorf twin.tec® PCR Plate 96, semi-skirted, 250 µL	47744-106, VWR
FACs tube	352008, Corning
Hand gloves	942190, Hartmann
Histology slides	PR-S-001, Klinipath
ImmEdge Pen	H-4000, VECTOR
Magnetic Stand-96	AM10027, Invitrogen
MicroAmp® Fast 96-Well Reaction Plate (0.1 mL)	4346907, Applied Biosystems
MicroAmpTM Optical Adhesive Film	4311971, Applied Biosystems
Microseal 'B' adhesive film	MSB1001, BIORAD
PCR-strips	72.991.002, SARSTEDT

Pipet tips (with filter and no filter)	StarLab
Serological pipettes (5/10/25/50ml)	Corning
Serum tube for routine analysis	60.614.010, SARSTEDT
Stainless steel beads (5mm)	69989, Qiagen
Syringe Filters, 0.2 µm Pore	431224, Corning
Tissue embedding cassettes	Simport
Transfer pipette (3.5 mL)	86.1171.001, SARSTEDT
Vwr® Disposable Pipetting Reservoirs	89094-658, VWR
Whatman paper	A799.1, Roth

Routine laboratory devices

Agarose gel chamber	Bio-Rad
Axio Imager.Z1 Fluorescence Microscope	Zeiss
BioDocAnalyze	Biometra
Blotting Trans-Blot® Cell	Bio-Rad
Bright Field Microscope	Zeiss
Centrifuge 5424 R	Eppendorf
Centrifuge 5810 R	Eppendorf
Cryostat HM550	Thermo Scientific
Eppendorf Research pipettes 2.5/10/20/100/200/1000µl	Eppendorf
Hirschmann® pipetus	Hirschmann Laborgeräte GmbH
Magnetic stirring hotplate 3001	Heidolph
Mini centrifuge	Roth
NanoDrop	Thermo Scientific
PCR plate spinner	VWR
pH-Meter	Mettler Toledo
SDS PAGE electrophoresis system	peqLab
Shaker Rocker 25	Labnet international
Surgical tools	Fine Science Tools
Thermocycler	Biometra
Thermomixer	Eppendorf

TissueLyser II	Qiagen
Vortex Reax top	Heidolph
Waterbath 1002	GFL

Routine laboratory softwares

Adobe Illustrator	version 2024
AxioVision	version 4.9.1
Fiji	version 1.54p
FlowJo	version 10.9
GraphPad Prism	version 10.4.1
Microsoft Office Suite	Microsoft 365
Miniconda	version 24.11.1
Phenomaster	version 8.4.2
Python	Version 3.13.3
R	version 4.5.0
R studio	version 4.4.3

3.2. Charité-MASLD cohort

The patient data was kindly provided by Münevver Demir from Charité – University of Medicine. Details of the patients included in this study are provided in Table 1.

Table 1: Patient information concerning Charité-MASLD cohort

Parameter	Non-carrier	Heterozygous carrier	Homozygous carrier
Demographics			
Male:Female	38 (65.5%):20 (34.5%)	32 (48.5%):34 (51.5%)	10 (45.5%):12 (54.5%)
Age (years)	47.29 ± 15.06	49.44 ± 12.93	43.46 ± 16.78
Bodyweight (KG)	93.56 ± 16.99	93.09 ± 18.84	85.46 ± 23.31
BMI	30.86 ± 5.25	31.73 ± 5.36	29.54 ± 7.03

Metabolic Markers			
ALT (U/l)	62.1 ± 45.67	65.68 ± 36.26	77 ± 50.64
Triglyceride (mg/dL)	156.45 ± 88.01	159.24 ± 100.63	192.11 ± 153.37
Cholesterol (mg/dL)	47.72 ± 11.3	47.46 ± 14.5	56.29 ± 18.18
Medications (*Data presented as frequency [%] of patients using each drug class*)			
Antidiabetics (Metformin)	12%	18%	20%
Antihypertensives (Ramipril)	25%	23%	30%
Statins (Simvastatin)	15%	14%	18%
Thyroid Therapy (L-Thyroxin)	10%	14%	18%
Gastroprotective Agents (PPIs like Pantoprazol)	8%	12%	14%

3.3. Mice

Pnpla3^{I148M} knock-in mice (I148M mutation was introduced into mouse *Pnpla3* gene) on C57BL/6J genetic background were generated using genetically modified embryonic stem cells (VelociGene method [61]) in which the codon for isoleucine 148 (ATT) was replaced with a methionine codon (ATG) [62]. *Nlrp6* constitutive knockout mice on a C57BL/6J genetic background were obtained from Eicke Latz (University Hospital Bonn, Bonn, Germany). Mouse line with wild-type (*WT*), *Nlrp6*$^{-/-}$, homozygous *Pnpla3*^{I148M} knock-in (*Pnpla3*^{I148M}) and combination of homozygous *Pnpla3*^{I148M} knock-in with *Nlrp6*$^{-/-}$ (*Pnpla3*^{I148M}_*Nlrp6*$^{-/-}$) were attained from an initial breeding pair of heterozygous *Pnpla3*^{I148M} knock-in and *Nlrp6*$^{+/-}$. Homozygous offspring of this line were used to create individual *WT*, *Pnpla3*^{I148M}, *Nlrp6*$^{-/-}$ and *Pnpla3*^{I148M}_*Nlrp6*$^{-/-}$ breeding pairs. All littermates were weaned at 3 weeks of age and were kept in individually ventilated cages with free access to food (V1534-300, ssniff

Spezialdiäten GmbH) and water within the same room of the animal facility of the University Hospital RWTH Aachen. To avoid cross-transmission of microbiome, no exchange of mice, cages, or nesting materials was permitted among these four genotypic groups unless mentioned otherwise. The mice were maintained in a controlled environment (12h day-light cycle) and all experiments were approved by the appropriate German authorities for Animal Welfare (LANUV, Recklinghausen, North Rhine-Westphalia, Germany; File Ref. 81-02-04.2021.A311).

Cohorts of 8 weeks old male mice were randomly allocated in each experiment where each genotypic group contained mice from two litters coming from two different breeding pairs (4 mice/cage from each litter), and litters from individual breeding pair were used in at least three different experiments. Prior to the start of experiment, mice went through an acclimation phase of 7 days within the 'experiment room'. All mice received humane care according to the criteria outlined in the "Guide for the Care and Use of Laboratory Animals" (8th edition, 2011), prepared by the National Academy of Sciences [63].

DNA for genotyping was extracted from mouse ear tissue using 50 µL of DirectPCR (102-T, VIAGEN) and 0.5 µL of Proteinase K (A4392,0010, PanReac AppliChem), followed by incubation at 56 °C for 1 hour and then at 95 °C for 20 minutes. The extracted DNA was stored at −20 °C until used.

Genotyping was performed using the specific primers and master mix, with the corresponding PCR (polymerase chain reaction) cycling conditions provided in Table 2-3.

Table 2: *Pnpla3^{I148M}* genotyping

Pnpla3^{I148M}	
Distilled water	9.5 µL
ALLInTM HS Red (Taq Mastermix, 2X) (HSM0301c1, HighQu)	12.5 µL
Forward Primer (1: 10 dilution) (CCTAATCCCTCCTTCCTTCCG)	1 µL
Reverse Primer (1: 10 dilution) (CAGTGTATCCAACAGACAGCAGGC)	1 µL

+ 1 µL of DNA

PCR cycle:

	Preheat lid	99°C
1	95°C	3 minutes
2	95°C	5 seconds
3	56°C	10 seconds
4	72°C	15 seconds (go to 2 and add 35 loops)
5	72°C	5 minutes
6	8°C	Pause

Following PCR amplification, 25 µL of PCR product was combined with 2 µL of nuclease-free water, 3 µL of CutSmart Buffer (B6004S, New England BioLabs), and 0.1 µL of NheI restriction enzyme (R3131S, New England BioLabs), resulting in a total enzyme reaction volume of 5.1 µL. The mixture (25 µL PCR product + 5.1 µL enzyme solution) was then incubated at 37°C in the PCR machine overnight for complete digestion before gel electrophoresis.

Table 3: *Nlrp6$^{-/-}$* genotyping

Nlrp6$^{-/-}$	
Distilled water	13 µL
My-Budget (5X PCR Mastermix) (80-620XXXXX, Bio-Budget)	4 µL
NLRP6 MIL060-21 Primer (1: 10 dilution) (TCAAGCCCATCTTCTATGTC)	0.5 µL
NLRP6 MIL060-22 Primer (1: 10 dilution) (CATGGTTAGTCTTTCTGCGTCTTT)	0.5 µL
NLRP6 MIL060-23 Primer (1: 10 dilution) (TGATCTTCACAGAGCGAGCATTCC)	0.5 µL
NLRP6 MIL060-23 (NEO3a) Primer (1: 10 dilution) (GCAGCGCATCGCCTTCTATC)	0.5 µL

+ 1 µL of DNA

PCR cycle:

	Preheat lid	99°C
1	95°C	3 minutes
2	94°C	1 minute
3	58°C	1 minute
4	72°C	1 minute (go to 2 and add 34 loops)
5	8°C	Pause

For gel electrophoresis, a 2% (for *Nlrp6$^{-/-}$*) or 3% (for *Pnpla3^{I148M}*) agarose gel was prepared by dissolving agarose (16500-500, Invitrogen) in 1X TAE buffer (A1691, PanReac AppliChem). PeqGREEN nucleic acid stain (37-5010, Peqlab) was added at a concentration of 12 µL per 200 mL or 18 µL per 300 mL of gel solution. For molecular weight estimation, 8 µL of a '1 Kb Plus DNA Ladder' mix consisting of 10% 1 Kb Plus DNA Ladder (10787018, Invitrogen), 10% 10X BlueJuice™ Gel Loading Buffer (10816015, Invitrogen), and 80% distilled water was loaded per lane. The gel was run at 130 V for 1 hour.

The resulting band patterns for the *Pnpla3*^{I148M} genotyping were as follows: wild-type (*WT*) homozygotes displayed a single band at 232 bp; heterozygous mutants showed three bands at 232 bp, 143 bp, and 87 bp; and homozygous mutants exhibited two bands at 143 bp and 87 bp. For *Nlrp6* genotyping, *WT* homozygotes displayed a single band at 300 bp, whereas homozygous knockouts (*Nlrp6*$^{-/-}$) showed a single band at 525 bp.

3.4. Diet

The mice were either fed with standard CHOW diet (V1534-300, ssniff Spezialdiäten GmbH) or high fat diet (HFD) with mostly Primex Shortening-Z (non-trans-fat) as fat source (40 kcal % fat, 20 kcal % fructose, 2% cholesterol) (D16022301, Research Diets) until the end of experimental duration. All diets were fresh and within their shelf life, and the HFD was replaced twice weekly to maintain palatability and prevent spoilage.

3.5. Antibiotics treatment

The mice were treated for 8 weeks with a combination of four broad-spectrum antibiotic - 1 g/L ampicillin (2036628, Ratiopharm), 500 mg/L vancomycin (4110122, Eberth Arzneimittel), 1 g/L metronidazole (436216, Braun), and 1 g/L neomycin (21810-031, Gibco) – dissolved in autoclaved drinking water. To reduce the bitterness of the antibiotics, 10 g/L of D-glucose (A1422,1000, PanReac AppliChem) was also added to the solution. The antibiotic solution was changed every two days to maintain its efficacy and prevent fungal contamination.

3.6. Fecal microbiota transfer (FMT)

On the third week following the start of HFD-feeding, the mice were treated with the antibiotics cocktail as described previously for 1 week for microbiota reduction. Following the mice from each genotype were randomly selected and cohoused in two different cages for eubiotic and dysbiotic fecal microbiota transfer (FMT) procedure. For eubiotic FMT (eFMT), the donor was 16 weeks old *WT* mice feeding on CHOW while *Pnpla3^{I148M}_Nlrp6$^{-/-}$* mice feeding on HFD for 8 weeks (16 weeks old) were the donor for dysbiotic FMT (dFMT). During the period of cohousing, the 'used bedding' from the donor cages were mixed with fresh bedding material before adding them to the respective recipient cages. The FMT media was prepared as follows: 1X PBS (P04-36500, PAN-Biotech) with 0.05% L-cysteine hydrochloride (C1276-10G, Sigma) and 1 µg/mL Resazurin Sodium salt (R7017, Sigma) in Hungate tubes was gassed with nitrogen for around 5 minutes (until the solution turned colorless) to achieve anaerobic condition and following the solution was autoclaved (20 minutes at 121°C, 205 kPa) and stored at 4°C until use. Feces from the donors were collected immediately upon defecation (7 AM – 7.10 AM) and homogenized in FMT media (0.1g/mL) via vigorous vortexing under anaerobic condition. Afterwards, the mixture was rested for 5 minutes for gravitational sedimentation and each mouse was gavaged with 200 µL of the upper layer of respective solution (7.20 AM – 7.30 AM). FMT was performed 3 times per week, beginning in the fourth week and continuing until the eighth week of the HFD-feeding period.

3.7. Treatment with pasteurized Akkermansia muciniphila and Amuc_1100

The pasteurized form of *Akkermansia muciniphila* and Amuc_1100 [64] was provided by Willem M de Vos and Anneleen Seger. Starting from the fourth week and continuing until the eighth week of the HFD-feeding period, the mice were treated daily via oral gavage with either 1×10^8 CFU of pasteurized *Akkermansia muciniphila* or 3 µg of Amuc_1100 (11 AM – 11.30 AM).

3.8. Oral glucose tolerance test (OGTT)

Mice were subjected to oral glucose tolerance test (OGTT) three weeks before the completion of respective experiments. Prior to the test, mice were fasted for six hours (7.30 AM – 1.30 PM) with access to drinking water to normalize the glycemic index. Following the fasting period, blood glucose level was measured from the tail vein using glucose meter (ACCU-Check® Aviva, Roche). Afterwards, a bolus of 40% glucose (2357742, Braun) at the concentration of 2 g/kg of body weight (weight reference was based on the average body weight of *WT* mice on CHOW diet at the given experimental duration [65]) was orally administered via gavage and blood glucose level was measured at 15, 30, 60 and 120 minutes.

3.9. In vivo measurement of intestinal permeability (FITC-Dextran)

Intestinal permeability was assessed with 4 kDa Fluorescein isothiocyanate-dextran (FITC-Dextran) (46944-500MG-F, Sigma-Aldrich) which could pass through the intestinal barrier and be detected in plasma. Two weeks prior to the completion of respective experiment, mice were fasted for six hours (7.30 AM – 1.30 PM) with access to drinking water and afterwards they were orally gavaged with FITC-Dextran (500 mg/kg body weight, 125 mg/mL dissolved in 1X PBS). The dosage was calculated using the average body weight of *WT* mice on CHOW diet at the given experimental duration. Four hours after successfully administering the FITC-dextran solution, blood from the submandibular vein was collected within heparinized microvette (20.1282.100, Sarstedt) and centrifuged at 4°C, 2000 rcf for 5 minutes to separate the plasma. The fluorescence intensity of FITC-dextran in plasma was measured using the Cytation™3 reader (BioTek) with excitation at 485 nm and emission at 528 nm and the concentration was determined using a standard curve generated by diluting 125 mg/mL FITC-Dextran in 1X PBS.

3.10. Metabolic screening

The rate of oxygen consumption and carbon dioxide release, energy expenditure, mobility, feeding and drinking behavior of mice were recorded using TSE Phenomaster. One week prior to the start of the experiment, the mice were housed individually in single cages and trained to use drinking nipples designed for Phenomaster. During this period, the mice were routinely monitored for drinking behavior and body weight, as the adjustment to new housing conditions might result in weight loss. Before measuring the metabolic parameters, the reference oxygen and carbon dioxide levels in Phenomaster were respectively calibrated to 20.9% and 0.05%, with a flow rate of 0.5 L/minute. A three-day acclimatization period was further conducted with the system running, during which data was being collected at one-minute intervals. The light schedule for Phenomaster was maintained as it had been previously for the mice (lights off at 7 PM and lights on at 7 AM). The data from the last three days were used for analysis. Energy expenditure was calculated using Weir formula.

3.11. Collection and processing of mouse organs

Following euthanization (8 AM – 11.30 AM) with isofluran piramal (09714675, Piramal Critical Care Deutschland GmbH), blood was immediately collected from the portal vein (100 µL) and inferior vena cava (3-5 mL) within serum-vial (41.1500.005, Sarstedt). After centrifugation at 4°C, 12,000 rpm for 10 minutes, the resulting serum was snap-frozen in liquid nitrogen. Organs were dissected (Figure 6) and their weight/length were recorded. Subsequently, the samples were snap-frozen in liquid nitrogen, embedded in OCT (4583, Tissue-Tek) and frozen in dry ice, and fixed in either 4% formaldehyde (liver and adipose tissues) or methacarn solution consisting of 60% methanol, 30% chloroform, and 10% glacial acetic acid (first 1 cm of distal colon with gut-content, distal colon and ileum segments) for at least 24 hours at room temperature. Frozen samples were stored at -80°C until analysis and formaldehyde/methacarn fixed organ-parts were paraffin embedded.

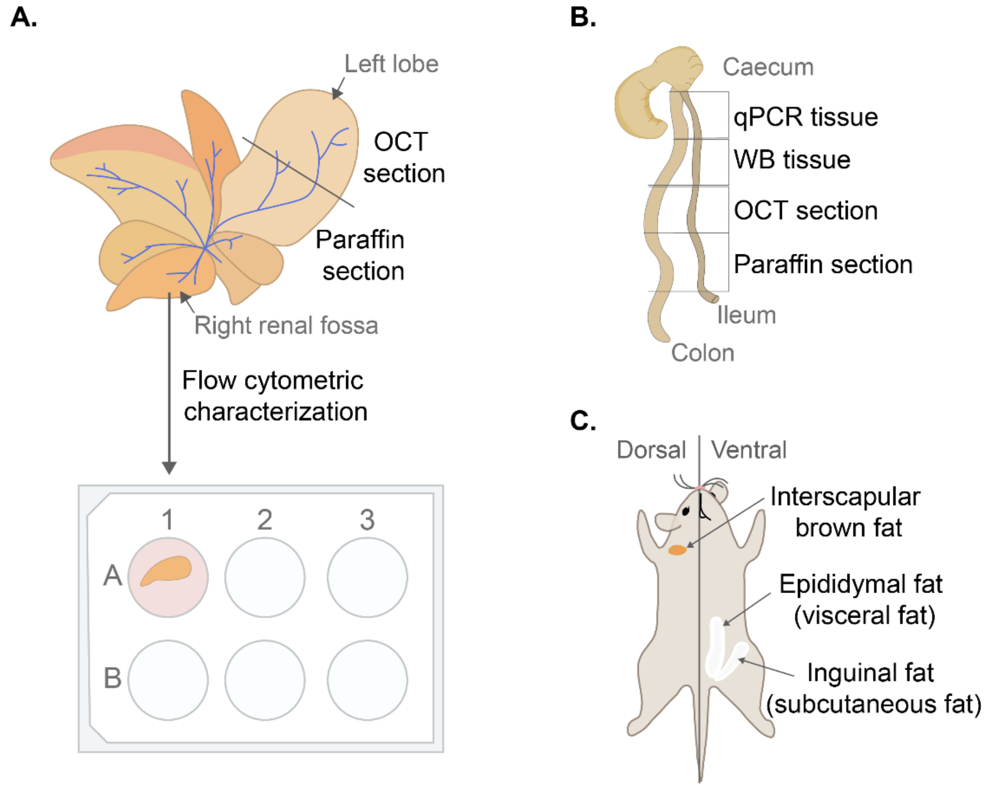

Figure 6: Tissue sampling strategy and representative biospecimens for downstream analysis. (A) The left hepatic lobe was preserved for cryopreservation (OCT) and paraffin embedding, while the right renal fossa was used for flow cytometry of intrahepatic immune cells. Remaining tissue was stored for complementary omics and molecular analysis. (B) Representative gut sections for histological and molecular analysis. (C) Representative adipose depots collected for parallel analysis.

3.12. Serum biochemistry

Following dilution with 1X PBS (1:10 for the HFD and dysbiotic FMT group, 1:5 for the others), serum triglycerides, cholesterol, and liver injury markers (AST, and ALT) were analyzed at the central laboratory of clinical chemistry, University Hospital RWTH Aachen.

3.13. Flow cytometric characterization of intrahepatic leukocytes

The liver was flushed with 1X PBS via the portal vein, and approximately 0.3 g of fresh liver tissue (right lobe) was finely chopped and enzymatically digested in DMEM (P04-03550, Pan-Biotech) containing 2 mg/mL collagenase D (11088882001, Roche) and 0.2 mg/mL DNase I (10104159001, Roche) at 37°C with shaking for 30 minutes. The digestion was stopped by adding 3 mL of cold flow-buffer (1.5 mM EDTA and 0.06% BSA in HBSS, P04-34500, Pan-Biotech). The suspension was filtered through a 70 µm strainer and centrifuged at 4°C at 50 rcf for 5 minutes. The supernatant was subsequently centrifuged at 4°C at 500 rcf for 10 minutes to pellet cells, followed by red blood cell lysis using 1 mL of RBC lysis buffer (555899, BD Pharm Lyse™) for 1 minute at room temperature. Cells were washed with 10 mL of flow-buffer, repelleted, and resuspended in 1 mL of flow-buffer. For staining, 400 µL of the cell suspension was distributed into separate tubes for lymphoid and myeloid panels, repelleted, and resuspended in a staining solution containing 12.5 µL of flow-buffer, 12.5 µL of blocking solution (prepared with 74% PBS, 20% of 10% BSA, 2% mouse serum (M5905, Merck), 2% rat serum (R9759, Merck), and 2% rabbit serum (R4505, Merck)), and 0.3 µL of the respective antibodies (Table 4). Following a 30-minute incubation in the dark at 4°C, 2 mL of flow-buffer was added to wash the samples, and the cells were repelleted. The final pellets were resuspended in 200 µL of flow-buffer containing 15,000 APC beads (340487, BD Biosciences). Data acquisition was conducted on a BD LSRFortessa flow cytometer (BD Biosciences) and analyzed using FlowJo software.

Table 4: Antibodies used in lymphoid and myeloid panel

Antibodies in lymphoid panel	Fluorochrome	Cat. No., Company
CD8a	FITC	100706, BioLegend
CD4	PerCP Cy5.5	45-0042-80, Invitrogen
NK1.1	PE-Cy7	108714, BioLegend
CD3e	APC	100312, BioLegend
CD19	Alexa Fluor 700	115528, BioLegend
CD45	APC-Cy7	557659, BD Biosciences
CD279 (PD1)	PE-Dazzle 594	135228, BioLegend
Antibodies in myeloid panel	Fluorochrome	Cat. No., Company
MHC II (I-A/I-E)	FITC	107606, BioLegend
CD11b	PE	557397, BD Biosciences
Ly6C	PerCP Cy5.5	128012, BioLegend
CD68	PE-Cy7	25-0681-80, Invitrogen
CD11c	APC	117310, BioLegend
F4/80	Alexa Fluor 700	56-4801-80, Invitrogen
CD45	APC-Cy7	557659, BD Biosciences
Ly6G	PE-CF594	562700, BD Biosciences

The gating strategy is illustrated in Figure 7. The absolute cell count was calculated using the formula: number of cells = (number of acquired cells x 15,000 x 2.5) / (number of acquired beads x weight of liver part); where 15,000 was the number of APC beads added and 2.5 was the dilution factor.

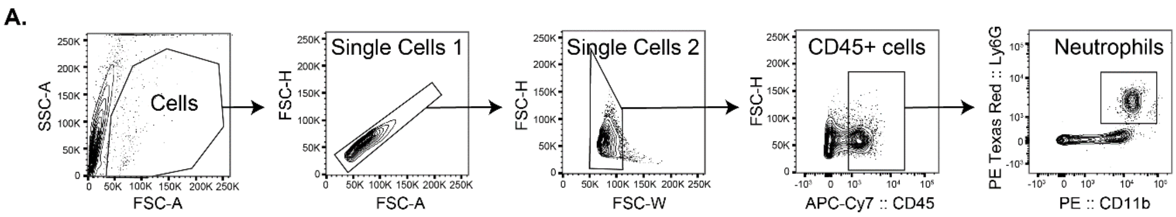

Figure 7: Gating strategy for intrahepatic immune cell subsets. (A) Neutrophils.

3.14. Hematoxylin and eosin (H&E) and Sirius red (SR) staining

Paraffin-embedded organs were sectioned at 3 μm thickness and deparaffinized by immersing in xylol for 3 minutes with two changes. Following deparaffinization, they underwent a series of ethanol baths: 100% ethanol for 2 minutes, repeated twice; 96% ethanol for 2 minutes, repeated twice; and finally, 70% ethanol for 2 minutes, to gradually rehydrate. The sections were then rinsed in distilled water for 5 minutes to complete the rehydration process.

For hematoxylin and eosin (H&E) staining, the rehydrated sections were first stained with hematoxylin (MHS32-1L, Sigma-Aldrich) for 3 minutes and then dipped twice in an acid solution (0.5% concentrated HCl in distilled water). Excess stain was washed off under running tap water for 5 minutes. Subsequently, sections were counterstained with eosin (1.09844.1000, Sigma-Aldrich) containing 2 drops of glacial acetic acid per 100 mL solution, with staining duration optimized between 2-5 minutes based on tissue type and desired intensity. After a brief rinse with distilled water (2 dips), the sections were dehydrated through a series of ethanol baths: 70% ethanol for 2 minutes, followed by 97% ethanol for 2 minutes, and then two changes of 100% ethanol for 2 minutes each. Finally, the sections were placed in xylol twice for 1 minute each and mounted using histokit (6638.1, Roth), then covered with a coverslip and allowed to dry overnight before proceeding with microscopic examination.

For Sirius red (SR) staining, rehydrated sections were stained with a 0.1% (w/v) Direct Red 80 (365548, Sigma) in Picric Acid (A2520,1000, PanReac AppliChem) at room temperature for 1 hour with gentle shaking. After staining, the sections were washed in distilled water containing 0.5% glacial acetic acid for 2 minutes, with two changes of solution. Finally, the sections were dehydrated and mounted as described earlier.

3.15. Alcian Blue & Periodic Acid-Schiff (AB-PAS) staining

Paraffin-embedded colon segment (first 1 cm of distal colon containing gut-content) was sectioned at 5 µm thickness, then deparaffinized and rehydrated as previously described. The rehydrated sections were first stained with freshly prepared 1% Alcian Blue (A3157, Sigma) dissolved in 3% acetic acid (pH = 2.5, filtered with Whatman paper followed by a 0.2-µm syringe filter) for 10 minutes. Following a rinse with tap water for 3 minutes and 20 dips in distilled water, the sections were oxidized with a 1% periodic acid solution (HP00.1, Roth) for 5 minutes. After another rinse as described earlier, the sections were incubated with Schiff's reagent (X900.1, Roth) for 10 minutes. Following a final rinse, the nuclei were counterstained with hematoxylin for 5 seconds, and the excess stain was washed off under running tap water for 5 minutes. Finally, the sections were dehydrated and mounted for microscopic observation as previously described.

3.16. Localization of bacteria by fluorescent in situ hybridization (FISH) within immunostained mucin layer

In order to analyze bacterial localization within the inner mucus layer of colon, 5 µm thick paraffin sections (first 1 cm of distal colon containing gut-content) was deparaffinized as follows: sections were preheated for 10 minutes at 60°C, followed by bathing in xylol at 60°C for 10 minutes, xylol at room temperature for 10 minutes and 99.5% ethanol at room temperature for 10 minutes. The hybridization step was performed overnight within a humidified chamber at 50°C with EUB338 probe (5'-GCTGCCTCCCGTAGGAGT-3', labeled with Alexa 647 at the 5' end) diluted in hybridization buffer (20 mM Tris-HCL at pH 7.4, 0.9 M NaCl, 0.1% SDS and 20% formamide, dissolved in nuclease free water and sterilized with 0.2-µm syringe filter) at a final concentration of 26 ng/µL for each section. After immersing the sections in freshly prepared washing buffer (20 mM Tris-HCL at pH 7.4 and 0.9 M NaCl dissolved in distilled water) at 50°C for 10 minutes and in 1X PBS at room temperature for 10 minutes (repeated thrice), they were blocked for 30 minutes at 4°C with blocking solution containing 5%

goat serum (S2007, Sigma) in 1X PBS. Mucin 2 primary antibody (sc-15334, Santa Cruz Biotechnology) was diluted in blocking solution at 1:1000 and applied overnight at 4°C. After washing with 1X PBS for 10 minutes (repeated thrice), goat anti-rabbit IgG with Alexa 488 secondary antibody (A11008, Invitrogen) diluted to 1:1000 in Blocking Solution was applied for 2 hours at 4°C. Following a final wash as described earlier, nuclei were counterstained with antifade reagent with DAPI (P36935, Invitrogen) and covered with coverslip for microscopic examination. Succeeding the hybridization step, the sections were consistently kept in darkness to protect the fluorescent signals from degradation or photo bleaching.

3.17. Oil red O (ORO) staining

To visualize hydrophobic and neutral lipids, Oil Red O (ORO) staining was performed on 12 μm thick OCT-embedded frozen liver sections. The ORO stock solution was prepared a week earlier by dissolving 0.5 g of Oil Red O (O0625, Sigma) in 100 mL of 2-Propanol. The ORO working-solution was then prepared by mixing 1.5 part of the stock solution with 1 part of distilled water. After resting for 10 minutes on ice, the working-solution was filtered through Whatman paper followed by a 0.2-μm syringe filter. Both the liver sections and ORO working-solution were equilibrated at room temperature for 10 minutes before staining. Subsequently, 200 μL of working-solution was applied to each section and incubated for 2 minutes. The excess stain was rinsed off with two changes of tap water (5 minutes each), and the nuclei were counterstained with hematoxylin for 15 seconds. After a 3 minutes rinse with tap water, the sections were mounted with an aqueous mounting medium (108562, Merck), covered with a coverslip, and examined under a microscope following 2 hours of drying at room temperature.

3.18. Measurement of liver triglyceride

Liver triglyceride was measured using TRIGLYCERIDE liquicolor^{mono} enzymatic colorimetric assay kit (10720P, Human GmbH). On the day before experiment, the homogenization buffer was prepared by dissolving 78 mg Tris, 22 mg EDTA, and 4.27 g sucrose in 50 mL distilled water and was rested overnight at 4°C. Liver samples weighing approximately 10-30 mg were excised and lysed in 1000 µL of the homogenization buffer using TissueLyser II (Qiagen) for 1 minute at 20 frequency/s. The lysates were then rested for 10 minutes on ice and centrifuged at 4°C, 3000 rcf for 10 minutes, and the resulting supernatant (700 µL) was transferred into new tubes. The enzymatic assay was conducted in a 96-well plate according to the manufacturer's instructions and the concentration of liver triglyceride was determined using a standard curve generated with standard solution provided with the kit.

3.19. Bile acid analysis

Bile acids from liver and fecal content were extracted by homogenizing approximately 50 mg of tissue in methanol (10 volumes of methanol per 1 volume of tissue) with TissueLyser II (Qiagen) for 10 minutes at 30 frequency/s. After homogenization, deuterated internal standards (d4-TCA, d4-CA, d4-CDCA, and d4-LCA) were added with a final concentration of 2.5 µM, and the samples were centrifuged at 4°C, 20,000 rcf for 10 minutes. To extract bile acids from peripheral serum, approximately 50 µL of serum was mixed with methanol (10 volumes) containing 50 nM of the respective deuterated internal standards. The mixture was then vortexed for 5 minutes and centrifuged at 4°C, 20,000 rcf for 10 minutes. The resulting supernatants from all the samples were evaporated under a nitrogen stream and the dried residues were reconstituted in 100 µL of methanol: water (1:1) and further centrifuged at 4°C, 10,000 rcf for 5 minutes to remove particulates. Approximately 5 µL of each sample was used for bile acid analysis using ultra-performance liquid chromatography-tandem mass spectrometry (UPLC-MS/MS). The bile acids were separated on a C18 column (1.7 µm, 2.1 mm x 100 mm; Kinetex, Phenomenex, U.S.A.) with water containing 7.5 mM ammonium acetate and 0.019% formic acid as mobile phase A, and acetonitrile containing 0.1% formic acid as mobile phase B. The chromatographic separation began with a 1-minute isocratic phase at 20% B, followed by a gradient increase to 35% B over 4 minutes. The B-phase was then increased to 100% over 10 minutes and maintained at 100% for 3.5 minutes before returning to 20%. The total runtime was 20 minutes. Bile acids were detected using multiple reaction monitoring (MRM) in negative mode on a QTRAP 5500 mass spectrometer (Sciex, Concord, Canada). Quantification was performed using appropriate deuterated internal standards and external individual standard curves for adjustments.

3.20. Metabolomics analysis of portal serum

The quantification of metabolites from portal-serum was carried out using the MxP Quant 500 kit (Biocrates Life Science AG, Austria). The analysis was performed on a Q-Trap API 5500 (SCIEX) coupled with a LC 1290 Infinity system (Agilent). Sample preparation and measurements were performed according to the manufacturer's instructions. The analyses were conducted using 10 µL of serum after derivatization with phenylisothiocyanate. Non-polar metabolites were analyzed using flow injection analysis (FIA) in positive ionization mode while polar analytes were separated chromatographically using the MxP Quan 500 Column System (Biocrates Life Sciences) with an oven temperature set at 50°C. Analysis of polar analytes was performed in both positive and negative ionization modes. The MetIDQ software was used for quantification and quality assurance according to the manufacturer's instructions.

3.21. Lipidomics analysis of liver tissue

Approximately 50 mg of frozen mouse liver tissue was transferred into a glass tube with a Teflon-lined cap (9826-16X, Corning) and homogenized in 200 µL of MS-grade water using a bead mill homogenizer. To the homogenate, 1.5 mL of methanol was added, and the sample was vortexed thoroughly. Next, 5 mL of methyl tert-butyl ether (MTBE) (306975, Sigma-Aldrich) was added to the mixture, followed by 1 hour of incubation at room temperature with constant shaking to facilitate lipid solubilization.

Phase separation was induced by the addition of 1.25 mL of MS-grade water, after which the mixture was allowed to incubate for 10 minutes at room temperature. The sample was then centrifuged at 1,000 × g for 10 minutes. The upper (organic) phase containing lipids was carefully collected. To maximize lipid recovery, the lower aqueous phase was re-extracted with 2 mL of a pre-equilibrated MTBE/methanol/water mixture (10:3:2.5, v/v/v). The resulting organic phases were combined and dried under vacuum in a centrifugal evaporator.

To expedite drying, 200 µL of MS-grade methanol was added after 25 minutes of centrifugation. Dried lipid extracts were reconstituted in 200 µL of chloroform/methanol/water (60:30:4.5, v/v/v) for storage at –20°C until analysis. Lipidomic profiling was subsequently performed via quadrupole time-of-flight mass spectrometry or triple quadrupole MS, depending on the required lipid class specificity and sensitivity.

3.22. 16S rRNA gene amplification and sequencing

16S rRNA gene amplification of the V4 region (F515/R806) from colonic samples was performed according to previously published protocol [66]. Demultiplexing of raw reads was executed using idemp (https://github.com/yhwu/idemp) based on the given barcodes [67] and libraries were processed to predict zero-radius operational taxonomic units (zOTUs) using the USEARCH pipeline version 11.0.667. Taxonomic annotations were assignment using the CONSTAX classifier (including SINTAX, RDP and BLAST) with the SILVA138 database [68], and results were summarized into a .biom file for analysis and visualization in Phyloseq [69] (version 1.46.0), Vegan [70] (version 2.6.4), DESeq2 [71] (version 1.42.1) and ggplot2 [72] (version 3.5.0).

3.23. Shotgun metagenome sequencing

Metagenomic libraries from colonic samples were prepared using the Illumina DNA PCR-Free Library Kit and IDT for Illumina DNA/RNA UD Indexes with previously isolated community DNA. Library preparation was done according to the manufacturer's protocol and quantification of library concentrations was performed using the Qubit ssDNA Assay Kit, followed by additional quantification with the KAPA Library Quantification Kit for Illumina. Sequencing was carried out on the NovaSeq S4 PE150 platform with a depth of 25 million reads per sample. Reads were trimmed for low adapter sequences and low quality, and filtered for phiX and mouse host reads using bbmap software tools [73]. The sequencing output was analyzed using a mouse gut metagenome catalog (iMGMC) [74]. Briefly, reads were mapped with bwa-mem2 to a catalog of 3,482 isolates and metagenome-assembled genomes (MAGs) for taxonomic annotation, while a collection of 4.6 million unique genes was used for functional annotation. Resulting absolute abundances were normalized to TPM, and KEGG functional orthologs were mapped to pathways via MinPath [75]. The output table and mapping file were utilized for statistical analyses and data visualization in Phyloseq [69] (version 1.46.0) and microbiomeMarker [76] (version 3.20).

3.24. Bulk mRNA sequencing

Total RNA was isolated from approximately 50 mg of liver tissue using the PureLink™ RNA Mini Kit (12183018A, Invitrogen) and treated with the PureLink™ DNase Set (12185010, Invitrogen) following the manufacturer's protocol. RNA samples with an RNA Integrity Number (RIN) > 7 were used to prepare sequencing libraries with the Illumina Stranded mRNA Prep Kit (20040534, Illumina) and IDT for Illumina RNA UD Indexes (20091659, Illumina), according to the manufacturer's instructions. Paired-end sequencing (200 cycles) was performed on the NovaSeq platform. Raw fastq files were processed using the STAR [77] aligner, and gene/isoform expression levels were quantified using RSEM [78]. Computations were performed with computing resources granted by RWTH Aachen University under project rwth1786. The resulting expression matrix was used for downstream statistical analysis and data visualization using org.Mm.eg.db [79] (version 3.20), clusterProfiler [80] (version 3.20), enrichplot [81] (version 3.20), DESeq2 [71] (version 1.42.1) and ggplot2 [72] (version 3.5.0).

3.25. Quantitative real-time PCR (qPCR)

Total RNA was extracted from liver, epididymal adipose tissue, ileal, and colonic tissues using TRIzol reagent (AM9906, Invitrogen) according to the manufacturer's instructions. For 16S rRNA RT-PCR, total RNA was isolated using the PureLink™ RNA Mini Kit (12183018A, Invitrogen) with on-column DNA digestion performed using the PureLink™ DNase Set (12185010, Invitrogen), according to the manufacturer's instructions.

Following quantification using NanoDrop, RNA samples were normalized to contain 1500 ng in a final volume of 20 µL. For example, a sample with a concentration of 200 ng/µL required 7.5 µL of RNA (1500 ng / 200 ng/µL) and 2.5 µL of nuclease-free water to prepare an initial 10 µL RNA mix. The remaining components were then added from the High-Capacity cDNA Reverse Transcription Kit (4368814, Applied Biosystems): 3.2 µL of nuclease-free water, 2 μL of 10X RT Buffer, 2 μL of 10X RT Random Primers, 0.8 μL of 25X dNTP Mix, 1 μL of Multiscribe Reverse Transcriptase, and 1 μL of RNase Inhibitor, resulting in a final reaction volume of 20 μL per sample. Complementary DNA (cDNA) synthesis was carried out using the following PCR cycle (Table 5).

Table 5: PCR cycle for cDNA synthesis

	Preheat lid	99°C
1	25°C	10 minutes
2	37°C	60 minutes
3	37°C	60 minutes
4	85°C	5 minutes
5	4°C	Pause

The synthesized cDNA was diluted with nuclease-free water prior to quantitative RT-PCR, with a 1:5 dilution used for liver and gut tissue samples, and a 1:2 dilution for adipose tissue samples to account for tissue-specific cDNA yield and expression levels. For each qPCR reaction, 3 μL of the appropriately diluted cDNA was combined with 1.5 μL of forward primer and 1.5 μL of reverse primer (Table 6), along with 3 μL of SYBR™ Green Master Mix (A25742, Applied Biosystems) and 1 μL of nuclease-free water, making up a total reaction volume of 10 μL. Quantitative RT-PCR was performed using the QuantStudio™ 6 Flex Real-Time PCR System (Applied Biosystems), and the thermal cycling conditions used for amplification are summarized in Table 7.

Table 6: Primer sequences for qPCR

Gene	Forward primer sequence (5'-3')	Reverse primer sequence (5'-3')
**Ppia*	GGCAAATGCTGGACCAAAC	CATTCCTGGACCCAAAAC
Tnfα	ACTGAACTTCGGGGTGATCG	GCCATTTGGGAACTTCTCATCC
Il1b	GCAGTGGTTCGAGGCCTAAT	CTCATCACTGTCAAAAGGTGGC
Il6	CAACGATGATGCACTTGCAGA	GGTACTCCAGAAGACCAGAGG
Cyp7a1	GCACCTCGTGATCCTCTGGG	GCTCTTGGCCAGCACTCTGTA
Cyp27a1	GCCTCACCTATGGGATCTTCA	TCAAAGCCTGACGCAGATG
Srebf2	CCTAGACCTCGCCAAAGGTG	CAGGCTGTAGCGGATCACAT
Ldlr	CTGGTGACCGAAAACATCCAGT	AATCAACCCAATAGAGACGGCC
Plin2	GACCTTGTGTCCTCCGCTTAT	CAACCGCAATTTGTGGCTC
Lipa	ATTCTCAAGGCTGCACCATAG	CAAGCGTCCCAATTGAAGTAG
Dgat1	GGAATATCCCCGTGCACAA	CATTTGCTGCTGCCATGTC
Dgat2	CCGCAAAGGCTTTGTGAA	GGAATAAGTGGGAACCAGATCAG
Cd36	ATGGGCTGTGATCGGAACTG	GTCTTCCCAATAAGCATGTCTCC
Cers6	GGGATCTTAGCCTGGTTCTGG	GCCTCCGTGTTCTTCAG
Col1a	TGTGTGCGATGACGTGCAAT	GGGTCCCTCGACTCCTAC
αSMA	TGACAGAGGCACCACTGAACC	TCCAGAGTCCAGCACAATACCAGT
16s rRNA	AGAGTTTGATCCTGGCTCAG	CTGCTGCCTCCCGTAGGAGT
Leptin	TCTCCGAGACCTCCTCCATCT	TTCCAGGACGCCATCCAG
**Hprt*	TGGGCTTACCTCACTGCTTT	CTAATCACGACGCTGGGACT
Fxr	TCCAGGGTTTCAGACACTGG	GCCGAACGAAGAAACATGG
Fgf15	GGTCCCTATGTCTCCAACTGC	CTTGATGGCAATCGTCTTCAGA
Asbt	GTCTGTCCCCCAAATGCAACT	CACCCCATAGAAAACATCACCA
Ostβ	GACAAGCATGTTCCTCCTGAG	GATGCAGGTCTTCTGGTGTTTC
Mrp3	CACCATCAGCTCGGCTACAT	CAGGTCCACCCATGAGACAC
Claudin-1	TCTACGAGGGACTGTGGATG	TCAGATTCAGCAAGGAGTCG
Claudin-2	GGCTGTTAGGCACATCCAT	TGGCACCAACATAGGAACTC
Claudin-3	TCATCGGCAGCAGCATCATCAC	ACGATGGTGATCTTGGCCTTGG
ZO-1	AGGACACCAAAGCATGTGAG	GGCATTCCTGCTGGTTACA

**Ppia* was the housekeeping gene for liver and adipose tissue

**Hprt* was the housekeeping gene for colon and ileum

Table 7: qPCR cycle

Hold stage		
	50°C	2 minutes
	95°C	2 minutes
PCR stage (40 cycles)		
	95°C	1 second
	60°C	30 seconds
Melt curve stage		
	95°C	15 seconds
	60°C	1 minute
	95°C	15 seconds

3.26. Western blot PCR (WB)

Total protein was extracted from liver (~50 mg) and ileal (~20 mg) tissues by homogenizing (3 minutes at 30 frequency/s) in IGEPAL lysis buffer (50 mM Tris, 150 mM NaCl, 50 mM NaF, and 1% IGEPAL (56741-50ML, Merck) dissolved in distilled water at pH 7.4), supplemented with one tablet each of Complete Mini (11836153001, Roche) and PhosSTOP (04906837001, Roche), along with 10 µL of 1 M DTT and 10 µL of 1 M Pefablock (A154.1, Roth) per 10 mL of buffer. Following a 30-minute incubation on ice, samples were centrifuged at 4°C, 12000 rcf for 15 minutes. Supernatants were collected, and protein concentrations were quantified using the Protein Assay Dye (5000006, Bio-Rad) with BSA as the standard (0–15 µg/µL), according to the manufacturer's instructions.

Protein samples were normalized using 6X Laemmli buffer (300 mM Tris-HCl, pH 6.8; 60% glycerol; 6% SDS; 0.025% bromophenol blue; 200 mM DTT) and IGEPAL lysis buffer. Proteins were separated on ready-to-use gels (5678125, Bio-Rad) alongside a protein ladder (LC5800, Invitrogen), and transferred onto ready-to-use nitrocellulose membranes (1704159, Bio-Rad). Membranes were blocked (1 hour at room temperature) and probed with primary (4°C, overnight) and secondary antibodies (1 hour at room temperature) (Table 8), with appropriate washes using TBST, prepared by diluting 10X TBS (24.2 g Tris base, 80 g NaCl, pH adjusted to 7.6 with HCl in 1L distilled water) 1:10 in distilled water and adding 0.1% Tween-20 (1 mL/1 L solution). Bands were visualized using ECL solution (GERPN2236, Cytiva).

Table 8: Blocking solution and antibodies used in WB

Primary & Secondary antibody	Blocking solution	Primary antibody dilution	Secondary antibody dilution
Cyp7a1 (sc-518007, Santa Cruz) m-IgGκ BP-HRP (sc-516102, Santa Cruz)	5% *non-fat milk in TBST	1:200 (in Blocking Solution)	1:2000 (in Blocking Solution)
Fgf15 (sc-514647, Santa Cruz) m-IgGκ BP-HRP (sc-516102, Santa Cruz)	5% *non-fat milk in TBST	1:200 (in Blocking Solution)	1:2000 (in Blocking Solution)
Bsep (PA5-78690, Invitrogen) anti-rabbit IgG-HRP (7074, Cell Signaling Technology)	5% *non-fat milk in TBST	1:500 (in Blocking Solution)	1:2000 (in Blocking Solution)
β-actin (A5441-100UL, Merck) m-IgGκ BP-HRP (sc-516102, Santa Cruz)	5% *non-fat milk in TBST	1:5000 (in Blocking Solution)	1:2000 (in Blocking Solution)

*non-fat milk (T145.2, ROTH)

3.27. Statistical analysis

All replicates in this study were biological, with experiments repeated independently. Statistical significance was determined using one-way ANOVA, with homogeneity of variance assessed via the Brown-Forsythe and Bartlett's tests. Post-hoc analysis was performed using Tukey's multiple comparisons test (family-wise alpha = 0.05) to identify pairwise differences among the four genotypic cohorts. All analyses were conducted using GraphPad Prism software (version 10.4.1) or R studio (version 4.4.3) with R (version 4.5.0). Data were represented as scatter dot plots with mean ± standard deviation (SD), and differences were considered statistically significant at $P \leq 0.05$.

Correlations among gut microbiota, ceramide/bile acid metabolites and gene expression were calculated using Hmisc package [124] (version 5.2.2) and visualized with ggplot2 [72] (version 3.5.0)/corrplot [125] (version 0.95), highlighting significance levels with star annotations.

Multivariate Association with Linear Models (MaAsLin2 [126], v1.8.0) was used to identify significant associations between microbial features (ZOTUs) and host ceramide and bile acid metabolites. Input data included normalized microbial relative abundances and log-transformed metabolite concentrations. MaAsLin2 was run using default settings with fixed effects for experimental group and host genotype, and multiple testing correction was applied using the Benjamini–Hochberg method. Associations with FDR-adjusted p-values < 0.25 were considered significant, in accordance with MaAsLin2 guidelines.

4. RESULTS

4.1. Microbial dysbiosis synergizes with *PNPLA3*^{I148M} to drive lipid metabolic perturbations

4.1.1. Absence of *PNPLA3*^{I148M} genotype-specific signatures in gut microbiota composition

Although the complex interactions between host genetics and the gut microbiota have been widely explored, the specific influence of the *PNPLA3*^{I148M} variant on gut microbial communities remains poorly understood [82]. This is particularly notable given the widespread global prevalence of this variant and its established clinical relevance in metabolic dysfunction-associated conditions, particularly MASLD [39, 40].

To fill this gap in knowledge, I conducted a comprehensive analysis of gut microbiome data collected from 146 MASLD patients at Charité – Universitätsmedizin Berlin, examining the microbial profiles of individuals both carrying and not carrying the *PNPLA3*^{I148M} variant. This cohort consisted of 58 non-carriers and 88 carriers, including both heterozygous and homozygous individuals. I first assessed the overall microbial diversity using Bray-Curtis dissimilarity metrics, which were weighted for relative abundance, to compare the gut microbiota composition between these two groups. Surprisingly, the initial analysis revealed no significant shifts in microbial composition between carriers and non-carriers of the *PNPLA3*^{I148M} variant (Figure 8A), suggesting that, in isolation, this genetic variation may not strongly impact the gut microbiome's overall structure.

A.

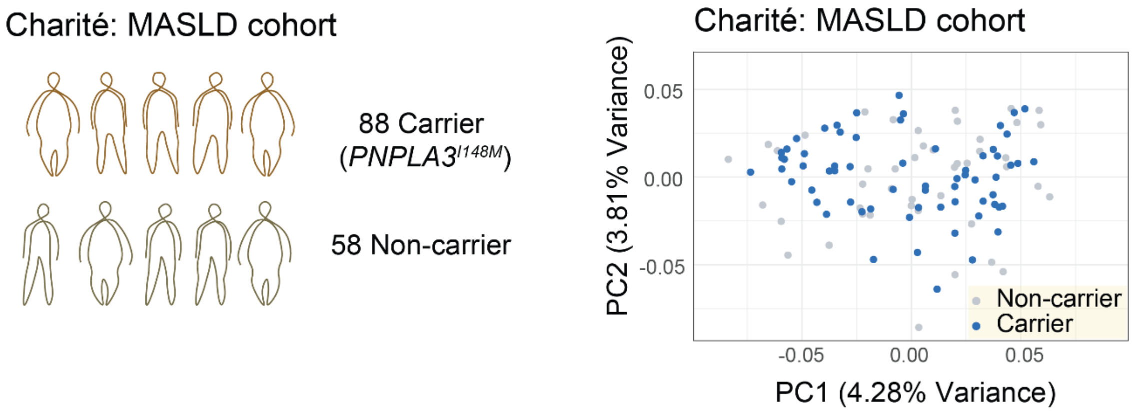

Figure 8: Gut microbiome composition is not significantly altered by *PNPLA3^{I148M}* carrier status. (A) Bray-Curtis dissimilarity analysis of fecal microbiota in 146 MASLD patients (58 non-carriers vs. 88 carriers of *PNPLA3^{I148M}*) revealed no distinct clustering by genetic variant (PERMANOVA, $p = 0.882$), suggesting limited microbial restructuring attributable to this allele alone. Individual data points represent biological replicates unless otherwise specified.

4.1.2. Dysbiosis-associated metabosensitivity in *PNPLA3^{I148M}* carriers

Given the well-established association between the *PNPLA3^{I148M}* variant and hepatic lipid accumulation, along with its link to hypertriglyceridemia [38], I aimed to investigate the role of the gut microbiome in modulating the pathophysiological consequences of this genetic variant.

The analysis indicated that the *PNPLA3^{I148M}* variant significantly modified the relationship between body mass index (BMI) and circulating triglyceride levels. Among carriers of the variant allele, mean triglyceride levels were elevated (184 ± 142 mg/dL) compared to non-carriers (156 ± 88 mg/dL) (Figure 9A), despite similar mean BMIs (31.2 ± 5.86 vs. 30.9 ± 5.25). The correlation between BMI and triglyceride levels was modestly positive in carriers (r = 0.249) but nearly absent in non-carriers (r = –0.033). In stratified linear regression analysis, BMI was a significant predictor of triglyceride levels in carriers, with each unit increase in BMI associated with a 6.56 mg/dL rise in triglycerides (95% CI: 1.04–12.07; $p = 0.021$; $R^2 = 0.062$) (Figure 9B). In contrast, this association was non-significant in non-carriers ($p = 0.804$; $R^2 = 0.001$). These findings suggest that individuals harboring the *PNPLA3*^{I148M} variant may experience greater metabolic sensitivity to adiposity, with elevated triglyceride levels emerging even at lower BMI thresholds, while non-carriers appear relatively protected from triglyceride accumulation in the context of increasing adiposity.

This metabolic vulnerability in carriers prompted further investigation into potential modulators of this phenotype. To explore this, I categorized a cohort of 50 carriers of the *PNPLA3*^{I148M} variant with available serum triglyceride and 16s rRNA data into two distinct subgroups: one with elevated triglyceride levels (>150 mg/dL) and another with lower levels (<150 mg/dL), using clinically accepted cutoffs for hypertriglyceridemia [83]. My analysis revealed a statistically significant association between serum triglyceride levels and gut microbial diversity, with triglyceride status explaining 14.54% of the variation in beta diversity ($p = 0.001$) (Figure 9C). The primary microbial axis (PC1), which accounted for 29.08% of total microbiome variation, showed a robust positive correlation with triglyceride concentrations (r = 0.68, $p = 7.04 \times 10^{-8}$), indicating that 46% of triglyceride variance could be explained by microbial variation along this axis. A similar pattern was observed for PC2 (r = 0.63, $p = 1.12 \times 10^{-6}$) (Figure 9D). Taxonomic analysis revealed that Firmicutes was inversely associated with triglyceride levels (Spearman's ρ = -0.36, $p < 0.05$), aligning with its strong negative loading on PC1 (ρ = -0.92).

These findings suggest that microbiome composition may play a pivotal role in modulating dyslipidemia in *PNPLA3*^{I148M} carriers than adiposity itself. This insight led to the hypothesis that gut microbial dysbiosis could serve as a critical trigger for metabolic dysfunction in individuals carrying the *PNPLA3*^{I148M} variant, potentially exacerbating MASLD pathogenesis. To explore the complex interplay among genetic susceptibility, microbial imbalance, and metabolic stress, a controlled murine model was established. This model was designed to examine how microbial dysbiosis triggers the onset and aggravates *PNPLA3*^{I148M}-associated MASLD-related metabolic dysfunction.

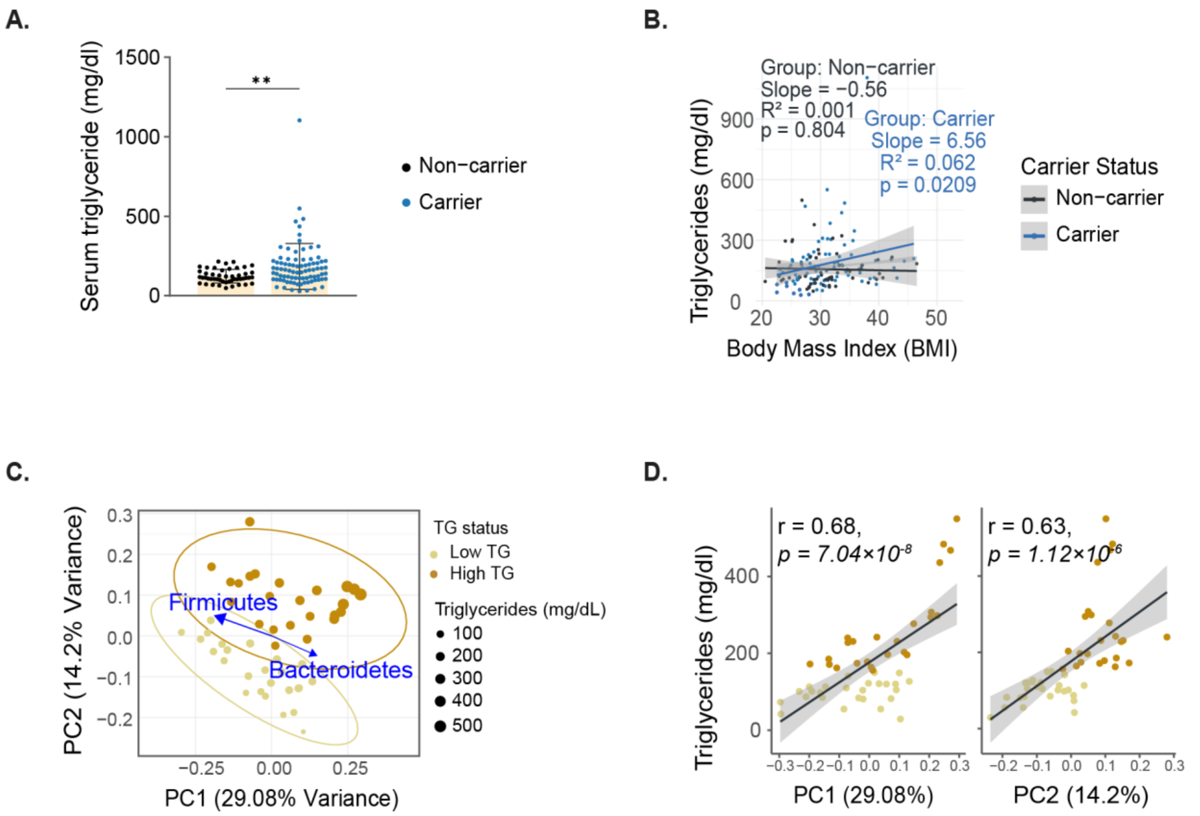

Figure 9: *PNPLA3*^{I148M} variant modifies BMI-triglyceride relationship and links gut microbiota to hypertriglyceridemia. (A) The carrier cohort of *PNPLA3*^{I148M} exhibited higher serum triglyceride level compared to the Non-carriers. (B) The association between BMI and triglycerides was stronger in carriers ($r = 0.249$, $p = 0.021$) compared to non-carriers ($r = –0.033$, $p = 0.804$), suggesting a genotype-dependent interaction. (C) In carriers, gut microbial beta diversity differed significantly by triglyceride status (PERMANOVA, $p = 0.001$), with triglyceride levels explaining 14.5% of the variation. Firmicutes emerged as the dominant phylum and was inversely associated with triglyceride levels ($\rho = –0.36$, $p < 0.05$). (D) PC1 and PC2 strongly predicted triglyceride variability. Statistical analysis for Figure 9A used an unpaired two-tailed t-test. Data are presented as scatter dot plots with individual points representing biological replicates unless otherwise noted. Significance thresholds denoted as: $*P \leq 0.05$, $**P < 0.01$, $***P < 0.001$, and $****P < 0.0001$.

4.2. Synergistic pathogenesis in MASLD: *PNPLA3^{I148M}* genotype and microbial dysbiosis converge through the gut-liver axis

4.2.1. Rationale for a dual-hit paradigm: genetic and microbial synergy

While the *PNPLA3^{I148M}* variant predisposes carriers to hepatic steatosis, its variable penetrance in humans suggests the need for secondary triggers to unmask its full pathogenicity [62, 39]. Mirroring this clinical heterogeneity, murine studies demonstrate that *Pnpla3^{I148M}* expression, though sufficient to drive hepatic lipid accumulation under obesogenic conditions, fails to recapitulate the full spectrum of MASLD pathology alone [84]. Based on my observation and established theoretical models of MASLD, I hypothesized that a 'second hit' derived from gut dysbiosis could synergize with *Pnpla3^{I148M}* to accelerate disease. *Nlrp6*, a key inflammasome regulator, emerged as an ideal candidate for this 'second hit' due to its critical role in gut-liver axis homeostasis through shaping commensal microbiota and maintaining intestinal barrier integrity [85].

The combination of *Pnpla3^{I148M}* (metabolic first hit) and *Nlrp6* deficiency (dysbiotic second hit) thus creates a transformative and clinically relevant 'dual-hit' model (Figure 10) that: (a) recapitulates human disease heterogeneity, capturing the synergy between genetic susceptibility and dysbiosis; (b) identifies actionable targets, particularly gut-derived signals that exacerbate *Pnpla3^{I148M}*-associated lipotoxicity; and (c) paves the way for precision therapies tailored to high-risk carriers with dysbiosis.

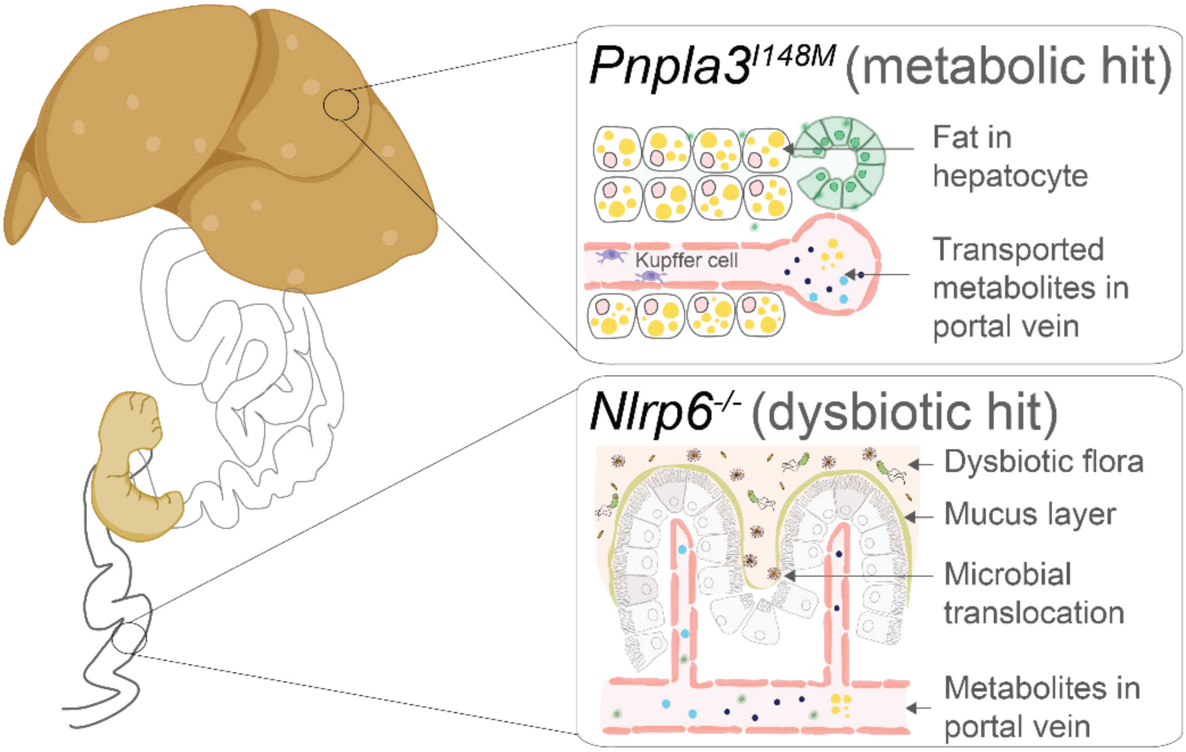

Figure 10: A 'dual-hit' model linking *Pnpla3^{I148M}* (metabolic hit) with *Nlrp6* deficiency (dysbiotic hit) to recapitulate human MASLD heterogeneity.

4.2.2. Early glucose intolerance reveals gut-liver axis vulnerability in dual-hit model

To validate this proposed 'dual-hit' hypothesis, I first analyzed metabolic parameters at a pre-symptomatic stage (16 weeks). Strikingly, even under standard CHOW diet conditions, *Pnpla3*^{I148M}_*Nlrp6*$^{-/-}$ mice exhibited impaired glucose tolerance (Figure 11A), indicating that synergistic metabolic disruption can arise prior to the onset of obesity. While absolute body weights were comparable across genotypes, *Pnpla3*^{I148M}_*Nlrp6*$^{-/-}$ cohort displayed a significantly higher white adipose tissue (WAT)-to-body weight ratio (Figure 11B-C), suggesting early adipose tissue dysfunction.

Fecal bile acid profiling revealed 3-fold increase in deoxycholic acid (DCA) in *Pnpla3*^{I148M}_*Nlrp6*$^{-/-}$ cohort (Figure 11D), a perturbation with direct clinical relevance. Notably, DCA levels showed a strong positive correlation with fasting glucose (r=0.7, $p=0.008$) (Figure 11E), implicating gut-liver axis dysfunction as the primary driver. The unexpected severity in normocaloric conditions warrants particular attention, as it parallels subclinical metabolic disturbances often seen in lean MASLD patients harboring *PNPLA3*^{I148M} risk alleles.

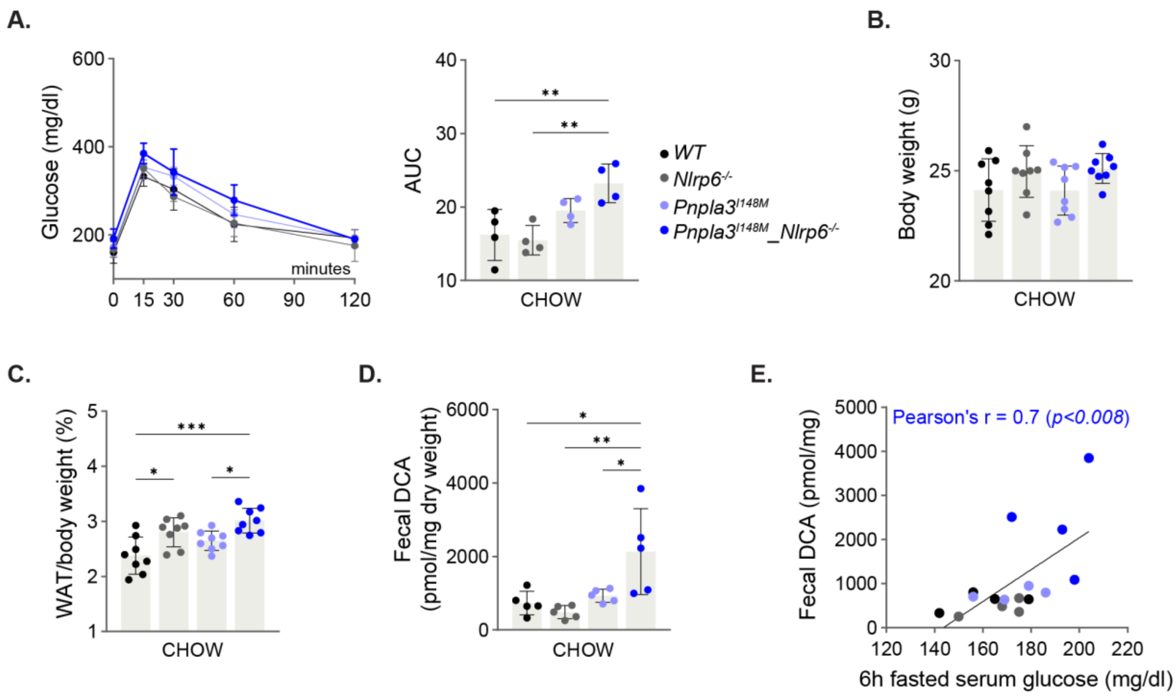

Figure 11: Early metabolic dysregulation in *Pnpla3^{I148M}_Nlrp6$^{-/-}$* cohort reveals gut-liver axis-driven pathogenesis. (A) Impaired glucose tolerance in *Pnpla3^{I148M}_Nlrp6$^{-/-}$* mice on CHOW diet (n=4). (B-C) Despite similar absolute body weights, elevated white adipose tissue (WAT)-to-body weight ratio (n=8). (D-E) Fecal DCA levels correlate with fasting glucose level (r=0.7, *p=0.008*) (n=4). Linear regression with 95% CI. Statistical analysis was performed using one-way ANOVA with Brown-Forsythe or Bartlett's test for variance homogeneity, followed by Tukey's post hoc comparisons (α = 0.05). Data are presented as scatter dot plots (mean ± SD), with individual points representing biological replicates unless otherwise noted. Significance thresholds denoted as: **P ≤ 0.05*, ***P < 0.01*, ****P < 0.001*, and *****P < 0.0001*.

4.2.3. Progressive metabolic deterioration in the genetic-dysbiotic model culminates in spontaneous MASLD

Building on the observation of early metabolic dysfunction in 16-week-old *Pnpla3*^{I148M}_*Nlrp6*$^{-/-}$ mice, longitudinal monitoring revealed progressive deterioration culminating in full MASLD pathology by 60 weeks of age, despite the absence of obesogenic high-fat diet (HFD) (Figure 12A). These mice exhibited a 30.4% increase in body weight ($p < 0.0001$), accompanied by significant adipose tissue expansion (Figure 12A-B), highlighting the onset of obesity-like features. Notably, this was paired with severe glucose intolerance, as reflected by an increase in the area under the curve (AUC) during oral glucose tolerance testing ($p < 0.0001$) (Figure 12D), indicative of systemic metabolic dysfunction.

A defining feature of the *Pnpla3*^{I148M}_*Nlrp6*$^{-/-}$ phenotype was profound gut-liver axis disruption, manifested by a marked increase in intestinal permeability (FITC-dextran assay) (Figure 12E). Hepatically, these mice exhibited significant hepatomegaly, with liver weights markedly higher than *WT*, *Nlrp6*$^{-/-}$ and *Pnpla3*^{I148M} cohorts, despite comparable caloric intake (Figure 12F-G). Histological analysis revealed severe macrovesicular steatosis (Oil Red O) and elevated hepatic triglycerides (Figure 12H-I). Concurrently, serum values of ALT and triglycerides were significantly elevated (Figure 12J), collectively demonstrating disrupted lipid metabolism and progressive hepatocellular damage.

Notably, while the *Pnpla3*^{I148M} cohort exhibited metabolic disturbances, the additional loss of *Nlrp6* synergistically drove spontaneous development of full metabolic syndrome and MASLD pathology under CHOW-fed conditions - including steatosis, glucose intolerance, and obesity without dietary provocation.

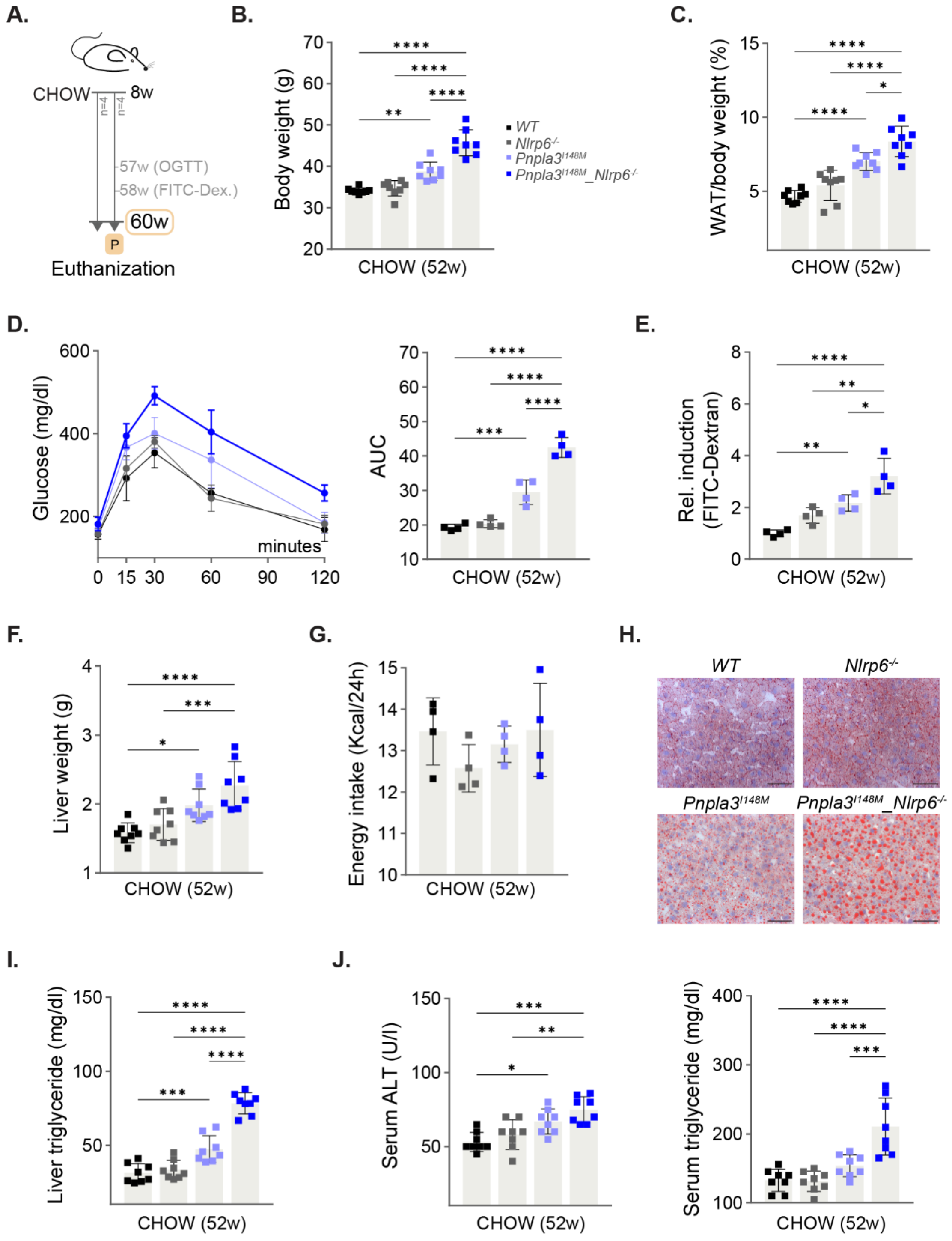

Figure 12: Spontaneous progression to full MASLD pathology in *Pnpla3^{I148M}_Nlrp6$^{-/-}$* mice under CHOW diet by 60 weeks. (A) Experimental timeline (n=8). P denotes the usage of Phenomaster. (B) Progressive body weight gain. (C) Adipose tissue expansion. (D) Worsened glucose intolerance. (E) Increased intestinal permeability. (F-I) Marked hepatomegaly despite comparable energy intake with histological evidence of hepatic lipid accumulation (ORO; scale bars, 100μm) and

elevated triglyceride level. (J) Elevated serum ALT and triglycerides. Statistical analysis was performed using one-way ANOVA with Brown-Forsythe or Bartlett's test for variance homogeneity, followed by Tukey's post hoc comparisons ($\alpha = 0.05$). Data are presented as scatter dot plots (mean ± SD), with individual points representing biological replicates unless otherwise noted. Significance thresholds denoted as: *$P \leq 0.05$, **$P < 0.01$, ***$P < 0.001$, and ****$P < 0.0001$.

4.2.4. Spontaneous MASLD progression correlates with distinct hepatic lipid species accumulation

Lipidomic profiling of age-progressed CHOW-fed *Pnpla3^{I148M}_Nlrp6$^{-/-}$* livers revealed profound disruptions in hepatic lipid homeostasis, paralleling the systemic metabolic deterioration. Notably, triglycerides (TGs) with shorter acyl chains and lower degrees of unsaturation, such as TG 50:2, TG 52:2, and TG 52:3, were significantly elevated ($p < 0.05$) (Figure 13A), suggesting impaired TG remodeling or selective retention of specific lipid species. In contrast, phosphatidylcholines (PCs), key components of lipoprotein assembly and membrane integrity, were markedly depleted (Figure 13B), indicating disrupted phospholipid metabolism, potential defects in VLDL secretion and HDL function [86]. These lipidomic abnormalities recapitulate classical features of MASLD, including hepatomegaly, macrovesicular steatosis, and elevated circulating triglycerides, demonstrating that the *Pnpla3^{I148M}_Nlrp6$^{-/-}$* genotype profoundly impairs hepatic lipid handling even in the absence of dietary fat excess. The concurrent accumulation of triglycerides and depletion of phosphatidylcholines reveals a dual lipid-handling defect: impaired lipid droplet dynamics and compromised lipoprotein secretion. Together, these findings establish the *Pnpla3^{I148M}_Nlrp6$^{-/-}$* mouse as a compelling model of spontaneous MASLD pathogenesis, where genetic predisposition, microbiome alterations, and metabolic disturbances synergistically drive disease progression.

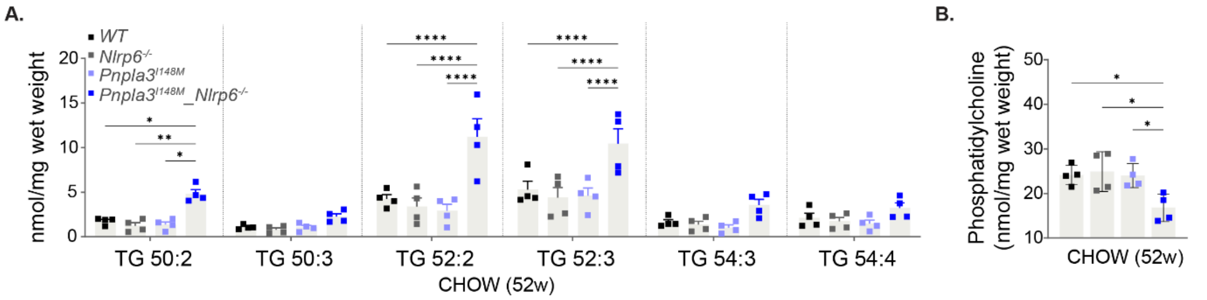

Figure 13: Lipidomic profiling reveals hepatic lipid remodeling associated with MASLD pathology in *Pnpla3^{I148M}_Nlrp6$^{-/-}$* mice (60 weeks) under CHOW diet. (A) Significant accumulation of triglyceride species (e.g., TG 50:2, TG 52:2, TG 52:3), indicating selective TG retention (n = 4). (B) Marked depletion of phosphatidylcholines in *Pnpla3^{I148M}_Nlrp6$^{-/-}$* mice (n = 4). Statistical analysis was performed using one-way ANOVA with Brown-Forsythe or Bartlett's test for variance homogeneity, followed by Tukey's post hoc comparisons (α = 0.05). Data are presented as scatter dot plots (mean ± SD), with individual points representing biological replicates unless otherwise noted. Significance thresholds denoted as: *$*P \leq 0.05$*, *$**P < 0.01$*, *$***P < 0.001$*, and *$****P < 0.0001$*.

4.3. Short-term dietary stress unmasks genetic-microbial synergy in MASLD

4.3.1. Modeling multifactorial MASLD: integrating genetics, dysbiosis, and dietary stress

Having established that *Pnpla3*^{I148M}*_Nlrp6*$^{-/-}$ mice develop spontaneous MASLD over time under CHOW-fed conditions, I next investigated whether obesogenic stress would accelerate disease progression, recapitulating the clinical exacerbation observed in genetically predisposed humans consuming diets rich in sugar and saturated fats. To model this gene-microbial interaction, I challenged mice with a high-fat diet (HFD) - a well-established paradigm that mirrors the pathophysiology of human MASLD [87]. This experimental design allowed us to: (1) decipher how genetic (*Pnpla3*^{I148M}) and microbial (*Nlrp6*$^{-/-}$-driven dysbiosis) risk factors collectively impair lipid handling under obesogenic pressure; and (2) map the resulting metabolomic perturbations (e.g., bile acids, ceramides) that propagate hepatic injury.

4.3.2. Gut barrier collapse in dual-hit mice reveals microbiome-dependent intestinal dysfunction

After 8 weeks of high-fat diet (HFD) feeding (Figure 14A), *Pnpla3*^{I148M}*_Nlrp6*$^{-/-}$ cohort exhibited distinct microbial community profiles, as revealed by Bray-Curtis dissimilarity in beta diversity analysis weighted for relative abundance (Figure 14B). This cohort showed the greatest divergence from *WT*, *Nlrp6*$^{-/-}$ and *Pnpla3*^{I148M} cohorts, while *WT* and *Pnpla3*^{I148M} cohorts displayed no significant differences—mirroring findings in human *PNPLA3*^{I148M} carriers. To ensure that differences in microbiota composition were attributable to gene–diet interactions rather than confounding factors such as cage effects or litter-specific influences, the experimental design incorporated animals obtained from multiple litters and housed across different cages.

Microbiota alterations in the *Pnpla3*^{I148M}*_Nlrp6*$^{-/-}$ cohort were accompanied by pronounced gut barrier dysfunction, a hallmark of impaired intestinal homeostasis. Mice exhibited significantly shortened colons (Figure 14C), a well-recognized indicator of chronic inflammation, alongside marked lymphocytic infiltration within the lamina propria (Figure 14D), pointing to mucosal immune activation. Functional impairment of the epithelial barrier was further demonstrated by increased translocation of FITC-dextran into the circulation (Figure 14E), reflecting heightened intestinal permeability.

At the molecular level, tight junction integrity was compromised, as evidenced by the downregulation of *Claudin* family members and *Zonula Occludens-1* (*ZO-1*) in the proximal colon (Figure 14F-G), indicating disrupted epithelial sealing. Further structural analysis using fluorescence in situ hybridization (FISH) revealed a 48.5% reduction in mucus layer thickness in *Pnpla3*^{I148M}*_Nlrp6*$^{-/-}$ cohort, accompanied by microbial encroachment with direct bacterial contact to the epithelial surface—a stark contrast to the ~18.5 μm average microbial-epithelial separation maintained in other genotypes (Figure 14H-J).

Taken together, these molecular and histological findings highlight a profound disruption of the intestinal barrier, encompassing both its physical components—tight junctions and the mucus layer—and its immunological defenses. This barrier collapse constitutes a pivotal mechanistic node in the progression of MASLD, potentially facilitating increased microbial translocation and systemic inflammation.

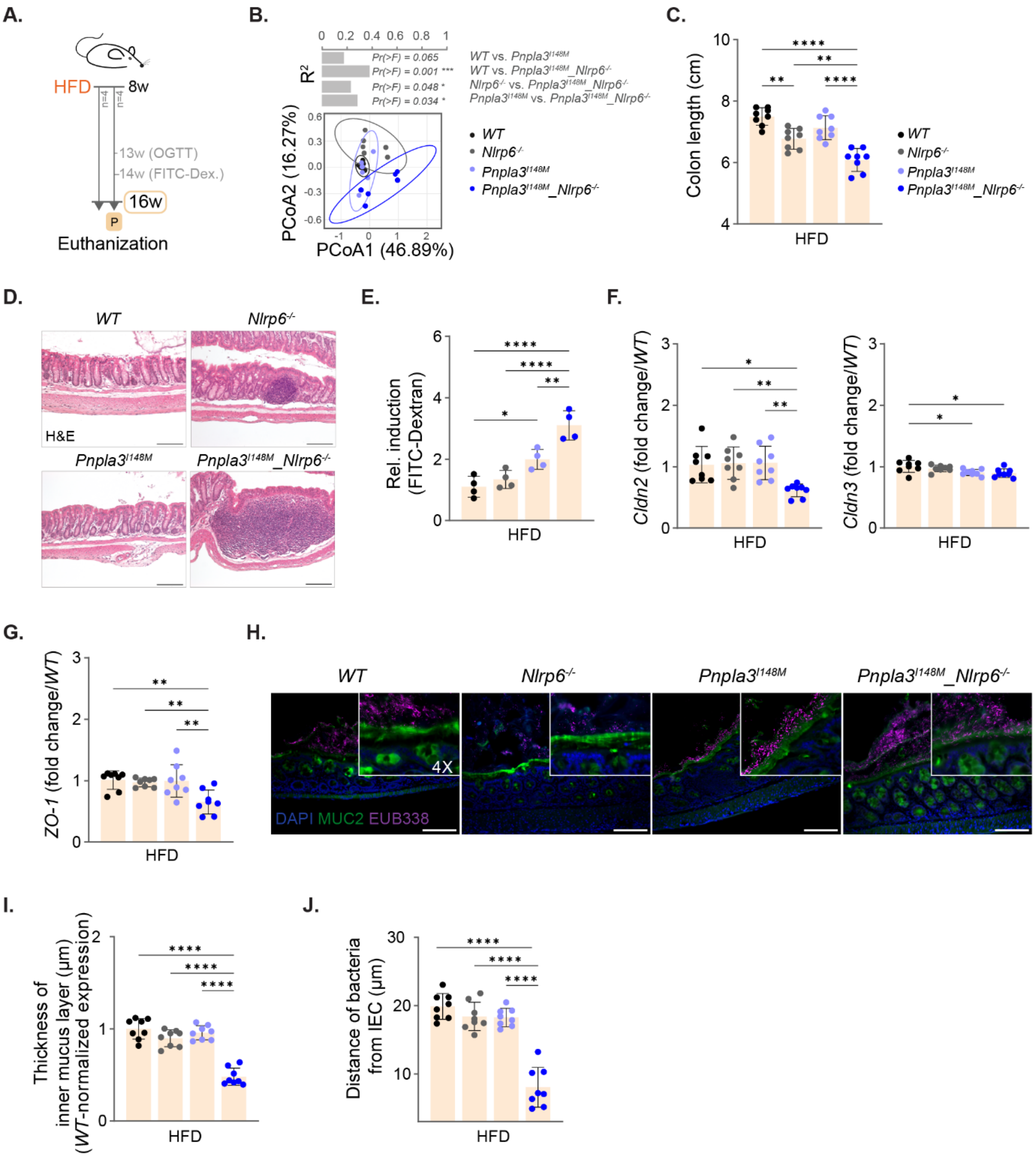

Figure 14: Gut microbiota dysbiosis and barrier dysfunction in HFD-fed *Pnpla3^{I148M}_Nlrp6$^{-/-}$* mice. (A) Experimental timeline of 8-week HFD challenge (n=8). P denotes the usage of Phenomaster. (B) Distinct microbial beta diversity (PCoA based on Bray-Curtis dissimilarity). (C-D) Colon shortening with lymphocytic infiltration in lamina propria (H&E; scale bars, 100µm). (E-G) Increased intestinal permeability and downregulation of tight junction proteins in colon. (H-J) Reduced mucus thickness and increased bacterial encroachment were demonstrated by MUC2 and EUB338 co-

staining using fluorescence in situ hybridization (FISH; scale bars, 100μm). Statistical analysis was performed using one-way ANOVA with Brown-Forsythe or Bartlett's test for variance homogeneity, followed by Tukey's post hoc comparisons (α = 0.05). Data are presented as scatter dot plots (mean ± SD), with individual points representing biological replicates unless otherwise noted. Significance thresholds denoted as: *$P \leq 0.05$*, **$P < 0.01$*, ***$P < 0.001$*, and ****$P < 0.0001$*.

4.3.3. Intestinal barrier failure drives systemic metabolic dysfunction in genetic-dysbiotic MASLD

These intestinal changes were not merely localized phenomena but were metabolically consequential, contributing to a systemic phenotype of dyslipidemia and glucose intolerance. Despite comparable daily caloric and water intake across all groups, the *Pnpla3*^{I148M}_*Nlrp6*$^{-/-}$ cohort exhibited significantly elevated serum triglycerides (Figure 15A-B), mirroring the hypertriglyceridemia observed in human *PNPLA3*^{I148M} carriers with dysbiotic flora.

In parallel, this cohort showed marked adiposity, with a 30.7% increase in white adipose tissue relative to body mass (Figure 15C), suggesting enhanced lipid storage or impaired mobilization. Importantly, this was coupled with clear signs of systemic metabolic dysfunction—fasting hyperglycemia (Figure 15D) and impaired glucose tolerance, as indicated by a 1.23-fold delay in glucose clearance during OGTT (Figure 15E).

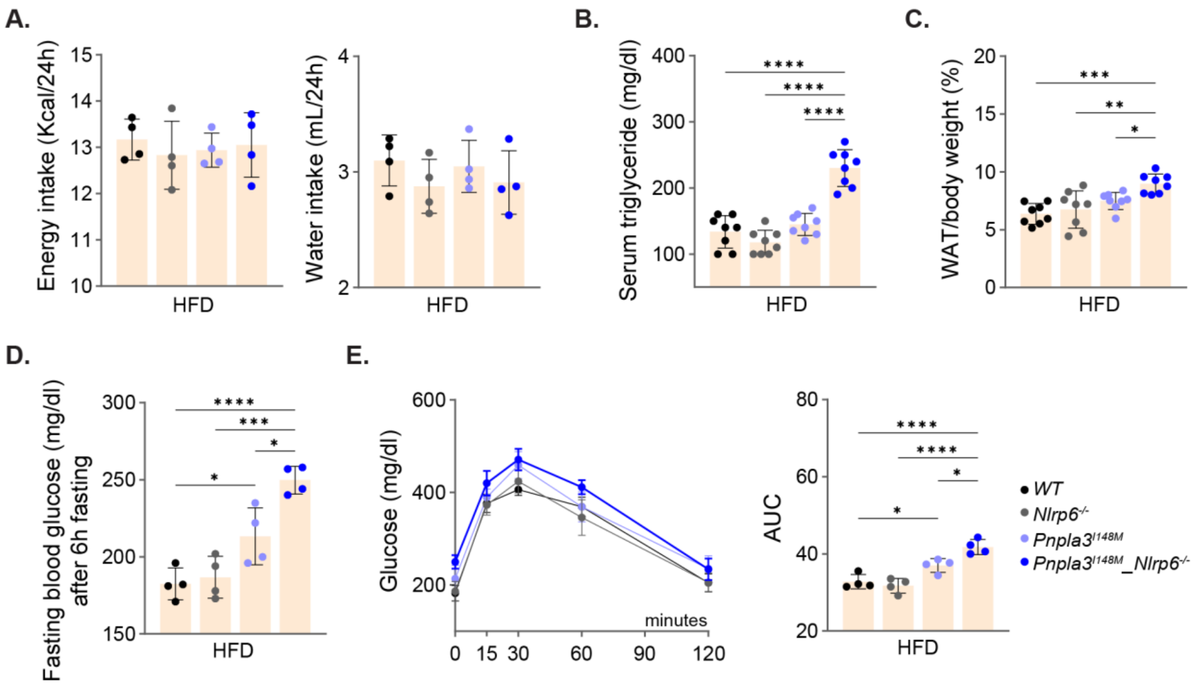

Figure 15: Dysbiosis associated onset of metabolic dysfunction in HFD-fed *Pnpla3^{I148M}_Nlrp6$^{-/-}$* mice. (A) Comparable daily energy and water intake among the genotypic cohorts. (B) Markedly elevated serum triglyceride levels. (C) Progressive adipose tissue expansion. (D-E) Fasting hyperglycemia and impaired glucose clearance. Statistical analysis was performed using one-way ANOVA with Brown-Forsythe or Bartlett's test for variance homogeneity, followed by Tukey's post hoc comparisons (α = 0.05). Data are presented as scatter dot plots (mean ± SD), with individual points representing biological replicates unless otherwise noted. Significance thresholds denoted as: **$P \leq 0.05$*, ***$P < 0.01$*, ****$P < 0.001$*, and *****$P < 0.0001$*.

4.3.4. Dual-hit pathogenesis drives inflammatory transition in genetic-dysbiotic MASLD

The *Pnpla3*^{I148M}_*Nlrp6*$^{-/-}$ cohort developed severe hepatic steatosis under obesogenic stress, as reflected by a significant increase in liver-to-body weight ratio (Figure 16A), along with extensive hepatic lipid deposition confirmed by histological analysis (Figure 16B). This accumulation of lipids was paralleled by elevated serum ALT levels (Figure 16C), indicative of hepatocellular injury. Notably, these alterations were substantially more pronounced than in *WT*, *Nlrp6*$^{-/-}$ and *Pnpla3*^{I148M} cohorts, underscoring the synergistic effect of combined genetic and microbial risk.

In addition to steatosis, livers from the *Pnpla3*^{I148M}_*Nlrp6*$^{-/-}$ cohort displayed overt inflammation, evidenced by increased hepatic expression of pro-inflammatory cytokines—including *TNFα*, *IL1β*, and *IL6* (Figure 16D), which are hallmarks of immune activation in MASLD [88]. Furthermore, flow cytometry revealed elevated neutrophil infiltration (Figure 16E), highlighting active immune cell recruitment likely driven by both lipid-mediated hepatocyte stress and microbial translocation from a compromised gut barrier. Together, these findings demonstrate that the dual-hit model not only precipitates lipid accumulation but also triggers inflammatory cascades characteristic of progressive MASLD.

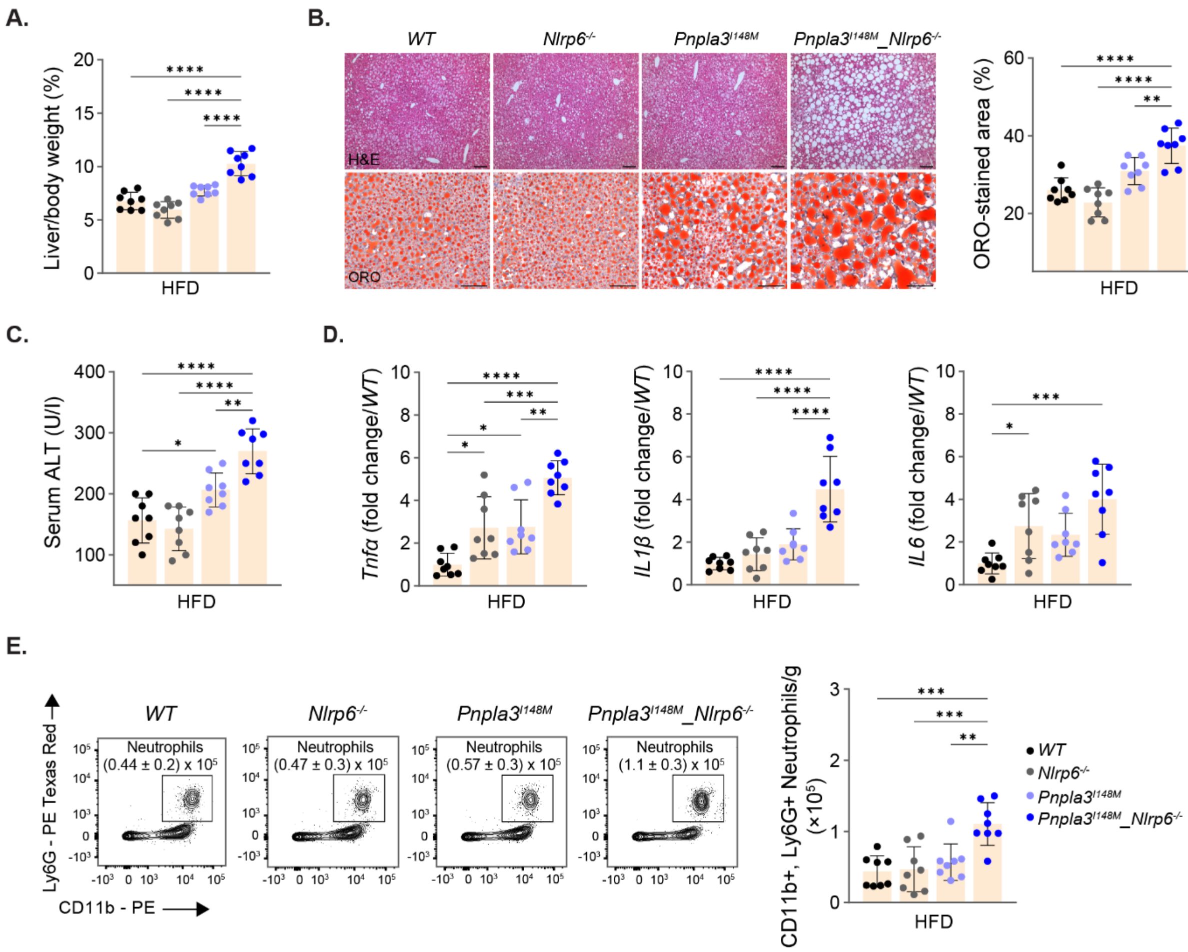

Figure 16: Dysbiosis associated metabolic dysfunction exacerbates hepatic steatosis and inflammation in HFD-fed *Pnpla3^{I148M}_Nlrp6$^{-/-}$* mice. (A-B) Increased liver-to-body weight ratio with macrovesicular steatosis (H&E; scale bars, 100µm) and lipid accumulation (ORO; scale bars, 100µm). (C) Elevated serum ALT indicates hepatocellular injury. (D-E) Upregulation of hepatic pro-inflammatory cytokines and enhanced neutrophil infiltration (characterized and quantified by flow cytometry) reflects immune activation and inflammation. Statistical analysis was performed using one-way ANOVA with Brown-Forsythe or Bartlett's test for variance homogeneity, followed by Tukey's post hoc comparisons (α = 0.05). Data are presented as scatter dot plots (mean ± SD), with individual points representing biological replicates unless otherwise noted. Significance thresholds denoted as: $*P \leq 0.05$, $**P < 0.01$, $***P < 0.001$, and $****P < 0.0001$.

4.3.5. The oxidation paradox: transcriptional adaptation without functional resolution

When exploring hepatic lipid handling in the *Pnpla3*^{I148M}_*Nlrp6*$^{-/-}$ cohort in contrast to *Pnpla3*^{I148M} cohort, a striking metabolic paradox emerged. Despite robust transcriptional upregulation of pathways essential for fatty acid catabolism [89]—namely PPAR signaling (*mmu03320*) and oxidative phosphorylation (*mmu00190*), hepatic triglyceride levels remained markedly elevated (Figure 17A-B). This disconnect implies a failure of compensatory metabolic adaptation, where transcriptional activation of lipid-oxidative pathways was functionally insufficient to counteract lipid accumulation.

Differential gene expression analysis (fold change >1, *adjusted* $p < 0.05$) revealed a pro-steatotic transcriptional signature in *Pnpla3*^{I148M}_*Nlrp6*$^{-/-}$ cohort (Figure 17C). Upregulation of *Aacs* (acetoacetyl-CoA synthetase) likely enhanced acetyl-CoA flux into de novo lipogenesis, while stable expression of *Dgat1* and *Dgat2* indicated that terminal TG synthesis was not the limiting step [89] (Figure 17C-D). Concurrently, enhanced hepatic lipid uptake was supported by elevated levels of *Cd36* (fatty acid translocase) and *Fabp4* (fatty acid-binding protein 4), both of which promote free fatty acid (FFA) import and intracellular trafficking toward TG accumulation [89] (Figure 17C, E). Interestingly, *Ces1d* (carboxylesterase 1D), a lipid droplet-associated hydrolase [89], was paradoxically upregulated, suggesting an attempted—yet ultimately inadequate—lipolytic response to counterbalance excess lipid load.

Collectively, these findings support a substrate-driven model of steatosis in the *Pnpla3*^{I148M}_*Nlrp6*$^{-/-}$ cohort, wherein transcriptional activation of lipid-oxidative pathways fails to resolve hepatic triglyceride accumulation. Compounding this metabolic dysfunction, genes linked to reactive oxygen species (ROS) generation (*mmu05208*) was markedly elevated, including key mitochondrial electron transport chain components (*Ndufs1*, *Ndufv1*, *Cyc1*) and the uncoupling protein *Ucp2* [90, 91] (Figure 17F-G). Paradoxically, despite concomitant antioxidant responses (Figure 17G), steatosis persisted—

revealing a self-reinforcing metabolic lesion characterized by: (1) impaired β-oxidation leading to cytotoxic lipid buildup, and (2) lipid-induced ROS overproduction that further exacerbated mitochondrial dysfunction [92]. This creates a vicious cycle where oxidative damage both initiates and perpetuates hepatic metabolic collapse.

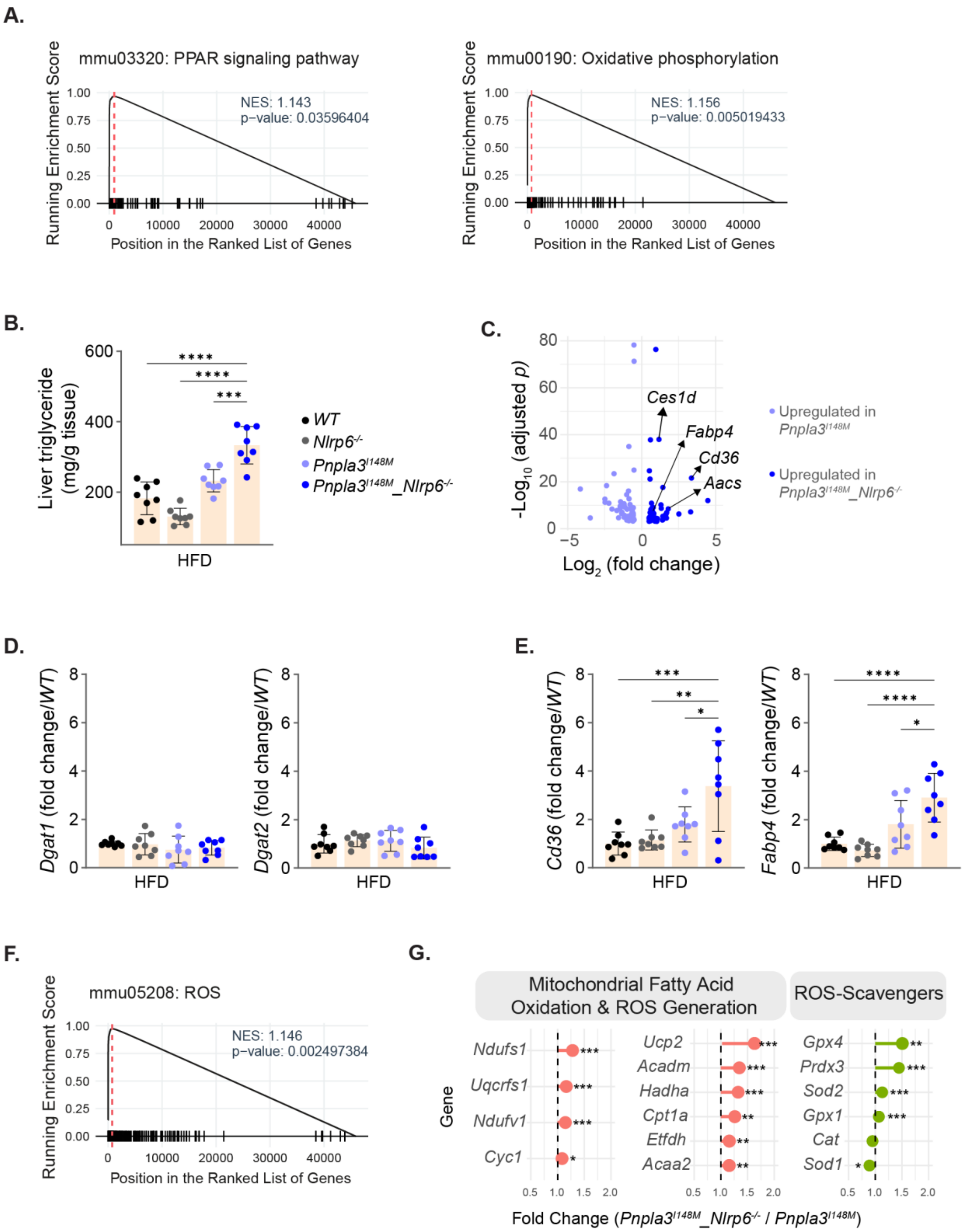

Figure 17: Compensatory metabolic signaling fails to prevent lipid accumulation and oxidative stress in HFD-fed *Pnpla3^{I148M}_Nlrp6$^{-/-}$* mice. (A-B) Despite upregulation of PPAR signaling and oxidative phosphorylation pathways (n=5), hepatic triglyceride levels remained elevated (n=8). (C-E) Hepatic expression of key lipid-handling genes revealed a pro-steatotic signature. (F-G) Induction of mitochondrial

ROS generators (n=5). Fold change >1, *adjusted* $p < 0.05$ for Figure A, C, F, G. Statistical analysis for figure B, D-E were performed using one-way ANOVA (Brown-Forsythe/Bartlett's tests for homogeneity) followed by Tukey's post-hoc comparisons ($\alpha = 0.05$). Data are shown as scatter dot plots (mean ± SD), with individual points representing biological replicates unless otherwise noted. Significance thresholds denoted as: $*P \leq 0.05$, $**P < 0.01$, $***P < 0.001$, and $****P < 0.0001$.

4.3.6. Systemic metabolic collapse extends to adipose dysfunction in dual-hit MASLD

This maladaptive cycle of lipid handling extended beyond the liver and was reflected in whole-body metabolic deterioration. Hepatic triglyceride content exhibited a strong negative correlation with systemic oxygen consumption (VO_2 ; *Pearson's* $r = –0.9$, $p < 0.0001$) (Figure 18A), accompanied by a significant reduction in whole-body energy expenditure in the *Pnpla3*^{I148M}_*Nlrp6*$^{-/-}$ cohort (Figure 18B). Notably, these systemic changes coincided with whitening of brown adipose tissue (BAT) (Figure 18C), a hallmark of thermogenic failure, indicating reduced mitochondrial density and oxidative capacity within BAT depots [93, 94]. This whitening reflects a broader collapse in energy homeostasis and suggests that impaired hepatic-mitochondrial function may send maladaptive signals to peripheral metabolic tissues, further compounding energy imbalance.

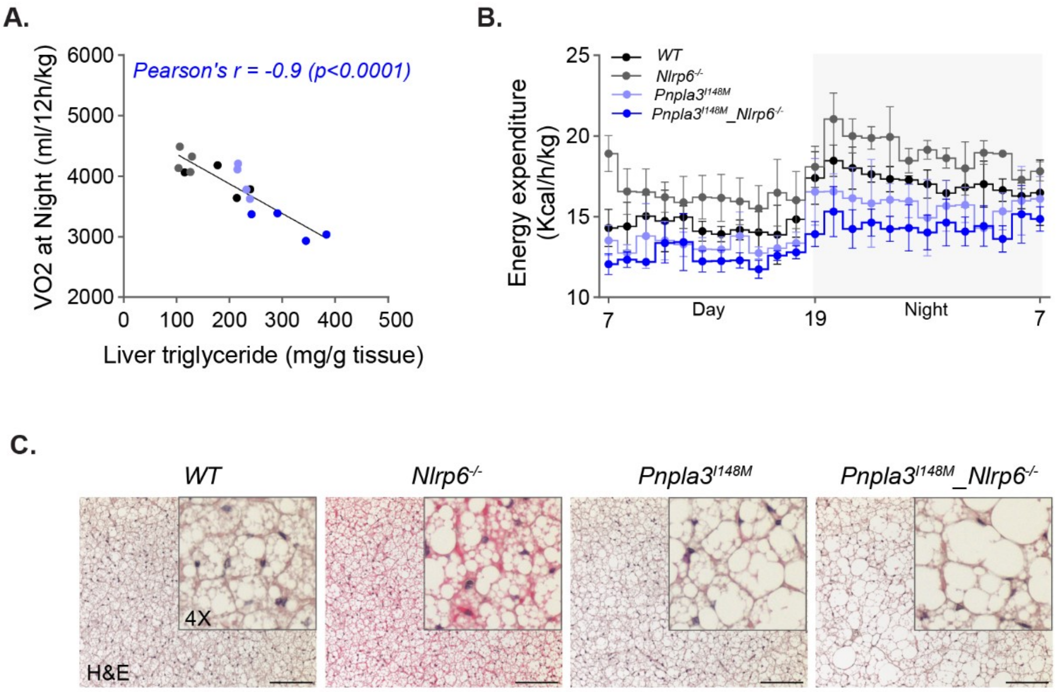

Figure 18: Hepatic lipid overload disrupts whole-body energy homeostasis in HFD-fed *Pnpla3^{I148M}_Nlrp6$^{-/-}$* mice. (A) Hepatic triglyceride negatively correlates with systemic oxygen consumption (r=-0.9, *p<0.0001*) (n=4). (B) Reduced whole-body energy expenditure reflects impaired metabolic efficiency. Data are presented as mean ± SD. (C) Whitening of BAT (H&E; scale bars, 100µm). Individual points representing biological replicates unless otherwise noted.

Thus, despite transcriptional upregulation of hepatic fatty acid oxidation and antioxidant responses, the liver remained entrenched in a state of redox-energetic failure. These findings implicate mitochondrial redox-energetic miscommunication—rather than lipid excess alone—as a central driver of progressive liver pathology and systemic metabolic compromise in this MASLD model.

4.3.7. Bile acid–ceramide dysregulation in hepatic steatosis

To investigate how the observed gut dysbiosis and intestinal barrier dysfunction exacerbate hepatic lipid accumulation and metabolic collapse in the *Pnpla3*^{I148M}*_Nlrp6*$^{-/-}$ cohort compared to *Pnpla3*^{I148M} cohort, I performed untargeted metabolomic analysis of portal vein serum (*fold change* > *1, adjusted* $p < 0.05$). This revealed significant enrichment of bile acids, including taurocholic acid (TCA), glycocholic acid (GCA), taurochenodeoxycholic acid (TCDCA), deoxycholic acid (DCA), and chenodeoxycholic acid (CDCA), alongside elevated levels of very-long-chain ceramides and dihydroceramides (Figure 19A), suggesting a gut-driven metabolic reprogramming.

Paradoxically, fecal bile acid excretion was diminished in this cohort, with selective retention of hydrophobic species like chenodeoxycholic acid (CDCA) and deoxycholic acid (DCA) (Figure 19B-C). Meanwhile, systemic bile acids were markedly elevated, particularly primary conjugated and secondary unconjugated forms, (Figure 19D). Mechanistically, this phenotype reflected disrupted enterohepatic circulation rather than synthesis overdrive, as evidenced by: (a) suppressed hepatic Cyp7a1 and Cyp27a1 despite systemic bile acid overload; (b) ileal *Fxr-Fgf15* axis activation; and (c) unaltered serum C4 (Figure 19E-G).

Critically, while ileal bile acid transporters (*Asbt*, *Ostβ*, *Mrp3*) remained intact (Figure 19E), the liver exhibited a complete rewiring of its transport apparatus: (1) impaired uptake of bile acids via *Ephx1*; (2) deficient canalicular excretion (*Abcb11*/Bsep downregulation); and (3) amplified basolateral efflux (*Abcc3-4*/*MRP3-4, Slc51b*/*Ostβ* upregulation) (Figure 19F) - collectively driving intrahepatic cholestasis and reduced biliary secretion.

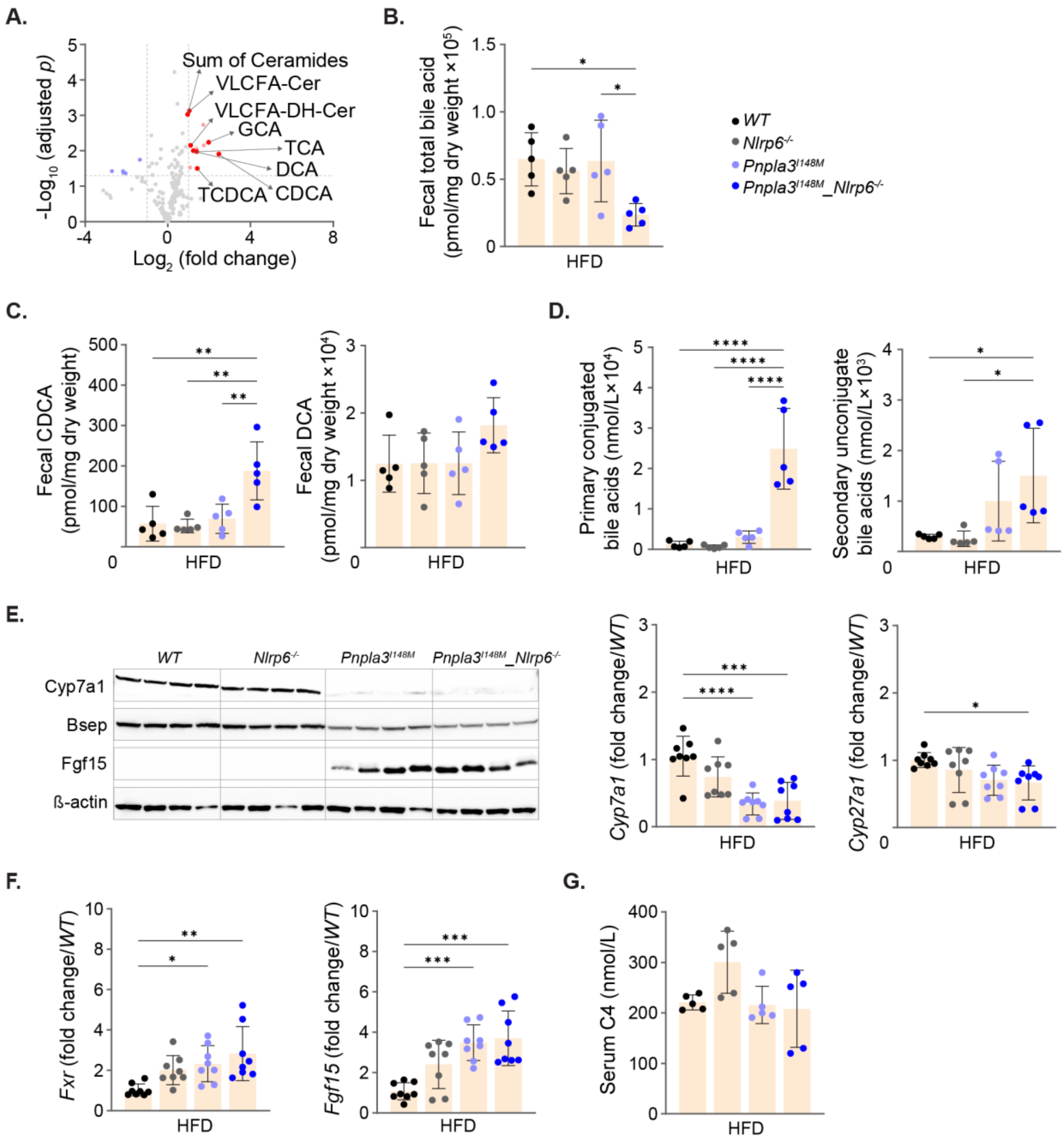
A.
Sum of Ceramides
VLCFA-Cer
VLCFA-DH-Cer
GCA
TCA
DCA
TCDCA
CDCA
-Log10 (adjusted p)
Log2 (fold change)
B.
Fecal total bile acid (pmol/mg dry weight ×10^5)
HFD
WT
Nlrp6-/-
Pnpla3I148M
Pnpla3I148M_Nlrp6-/-
C.
Fecal CDCA (pmol/mg dry weight)
Fecal DCA (pmol/mg dry weight ×10^4)
HFD
D.
Primary conjugated bile acids (nmol/L×10^4)
Secondary unconjugate bile acids (nmol/L×10^3)
HFD
E.
WT
Nlrp6-/-
Pnpla3I148M
Pnpla3I148M_Nlrp6-/-
Cyp7a1
Bsep
Fgf15
ß-actin
Cyp7a1 (fold change/WT)
Cyp27a1 (fold change/WT)
HFD
F.
Fxr (fold change/WT)
Fgf15 (fold change/WT)
HFD
G.
Serum C4 (nmol/L)
HFD

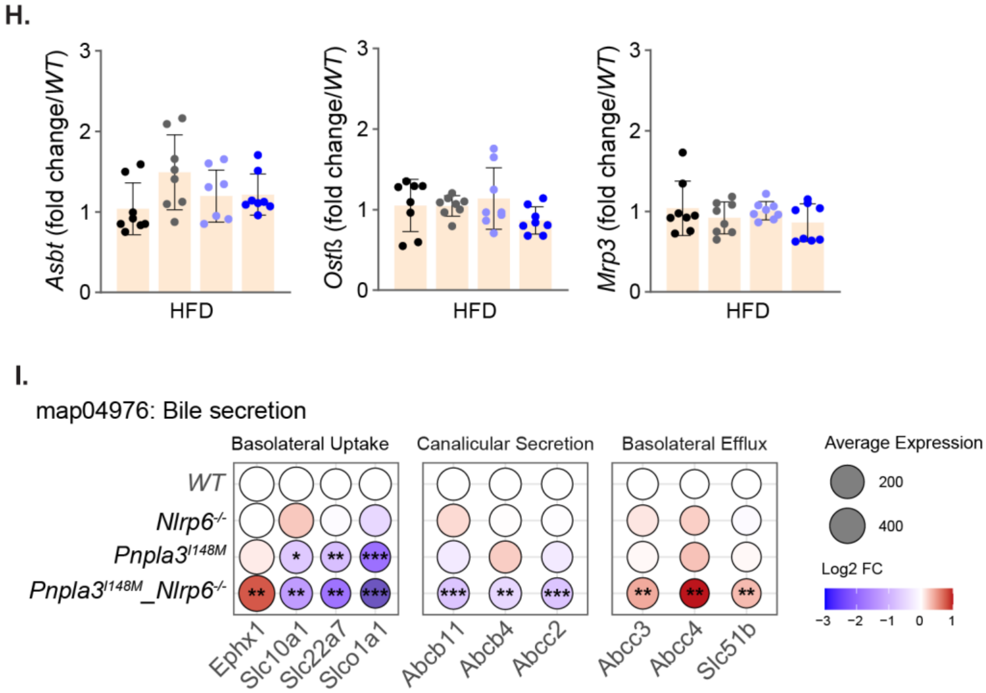

Figure 19: Gut dysbiosis alters portal vein metabolites and disrupts enterohepatic bile acid circulation in *Pnpla3^{I148M}_Nlrp6$^{-/-}$* mice. (A) Portal vein metabolomics reveal elevated bile acids and ceramides. (B-C) Fecal bile acid excretion decreases with selective retention of hydrophobic (CDCA and DCA) species. (D) Systemic bile acid overload (conjugated and unconjugated forms). (E-G) Suppressed hepatic bile-acid synthesis. (H) Intact ileal bile acid transporters. (I) Altered hepatic bile acid transport (TPM-normalized transcriptome data). Statistical analysis was performed using one-way ANOVA (Brown-Forsythe or Bartlett's test for variance homogeneity) with Tukey's post hoc test ($\alpha = 0.05$). Data are presented as scatter dot plots (mean ± SD), with individual points representing biological replicates unless otherwise noted. Significance thresholds denoted as: *$*P \leq 0.05$, $**P < 0.01$, $***P < 0.001$, and $****P < 0.0001$.

4.3.8. Dysbiosis fuels a self-amplifying metabolic lesion through bile acid–ceramide–mitochondrial axis

The observed hepatic metabolic dysfunction and the pronounced presence of hepatotoxic metabolites in the portal serum—suggested a systemic perturbation beyond intrinsic liver pathways. Given the known crosstalk between gut microbiota and hepatic metabolism, I hypothesized that gut-derived metabolites might underlie this dysregulation. To establish causal links between gut microbial remodeling and host metabolic disruptions, I integrated multi-omics analysis of matched microbiome, metagenomics, metabolomics, and transcriptome profiles from the same animals.

The *Pnpla3*^{I148M}*_Nlrp6*$^{-/-}$ cohort displayed a distinct microbiome signature when compared to *Pnpla3*^{I148M} cohort (*fold change* > 1, $p < 0.05$), enriched in *Clostridium scindens*, *Bacteroides ovatus*, *Alistipes finegoldii*, and *Oscillibacter* (*validated using EzBioCloud, confirming > 98% sequence similarity*) (Figure 20A). These species have been previously implicated in hydrophobic bile acid transformation and ceramide metabolism [95-100]. Complementary metagenomic analysis confirmed upregulation of microbial pathways involved in secondary bile acid biosynthesis (*ko00121*) and sphingolipid metabolism (*ko00600*) (Figure 20B).

Differential metabolomic profiling of portal serum revealed a marked elevation of specific ceramide species (Cer d18:1/16:0, Cer d18:1/18:0, Cer d18:1/23:0, Cer d18:1/24:0, Cer d18:1/24:1, Cer d18:1/25:0) in the *Pnpla3*^{I148M}*_Nlrp6*$^{-/-}$ cohort (Figure 20C), which positively correlated with: (1) microbial signatures (*Clostridium scindens*, *Alistipes finegoldii*, *Oscillibacter*); (2) hepatic Cers6 upregulation; and (3) mitochondrial dysfunction markers (*Ucp2*, *Hspd1*, *Ndufv1*, *Ndufs1*, *Cyc1*) (Figure 20D-E). Notably, Cer d18:1/16:0 and Cer d18:1/18:0 positively correlated with *Cpt1a* and inversely with *Cyp7a1* and *Cyp27a1* (bile acid synthesis), suggesting dual roles in metabolic impairment.

These mechanistic insights support a model in which gut microbiota–derived bile acids and ceramides coordinate a pathological metabolic axis that drives hepatic steatosis by: (1) inducing mitochondrial stress and impairing oxidative metabolism [101]; (2) suppressing Cyp7a1 to activate *Srebf2/Ldlr*-mediated lipid uptake [102-104]; and (3) upregulating *CerS6*, which promotes lipid retention via the *Plin2/Lipa* pathway [105-108] (Figure 20F).

Together, this dysbiosis-driven imbalance in the bile acid–ceramide–mitochondrial axis formed a self-sustaining pathogenic loop, amplifying hepatic injury and accelerating MASLD progression in the genetically susceptible host. Specifically, alterations in gut microbial composition led to increased production of secondary bile acids and ceramides, which entered the liver through the portal circulation and disrupted key metabolic and signaling pathways. These metabolites impaired mitochondrial function, elevated oxidative stress, and hindered lipid oxidation, thereby promoting intracellular lipid accumulation. Simultaneously, suppression of bile acid synthesis enzymes (Cyp7a1 and Cyp27a1) and activation of lipid uptake pathways (*Srebf2/Ldlr, Cd36*) further contributed to hepatic steatosis. The upregulation of *CerS6*, along with downstream targets like *Plin2* and *Lipa*, facilitated lipid droplet stability and retention, reinforcing the lipotoxic state. Altogether, this network of gut–liver interactions created a feed-forward loop in which microbial metabolites continuously fueled hepatic metabolic stress, inflammation, and lipid accumulation, driving the progression of MASLD in $Pnpla3^{I148M}$_$Nlrp6^{-/-}$ cohort.

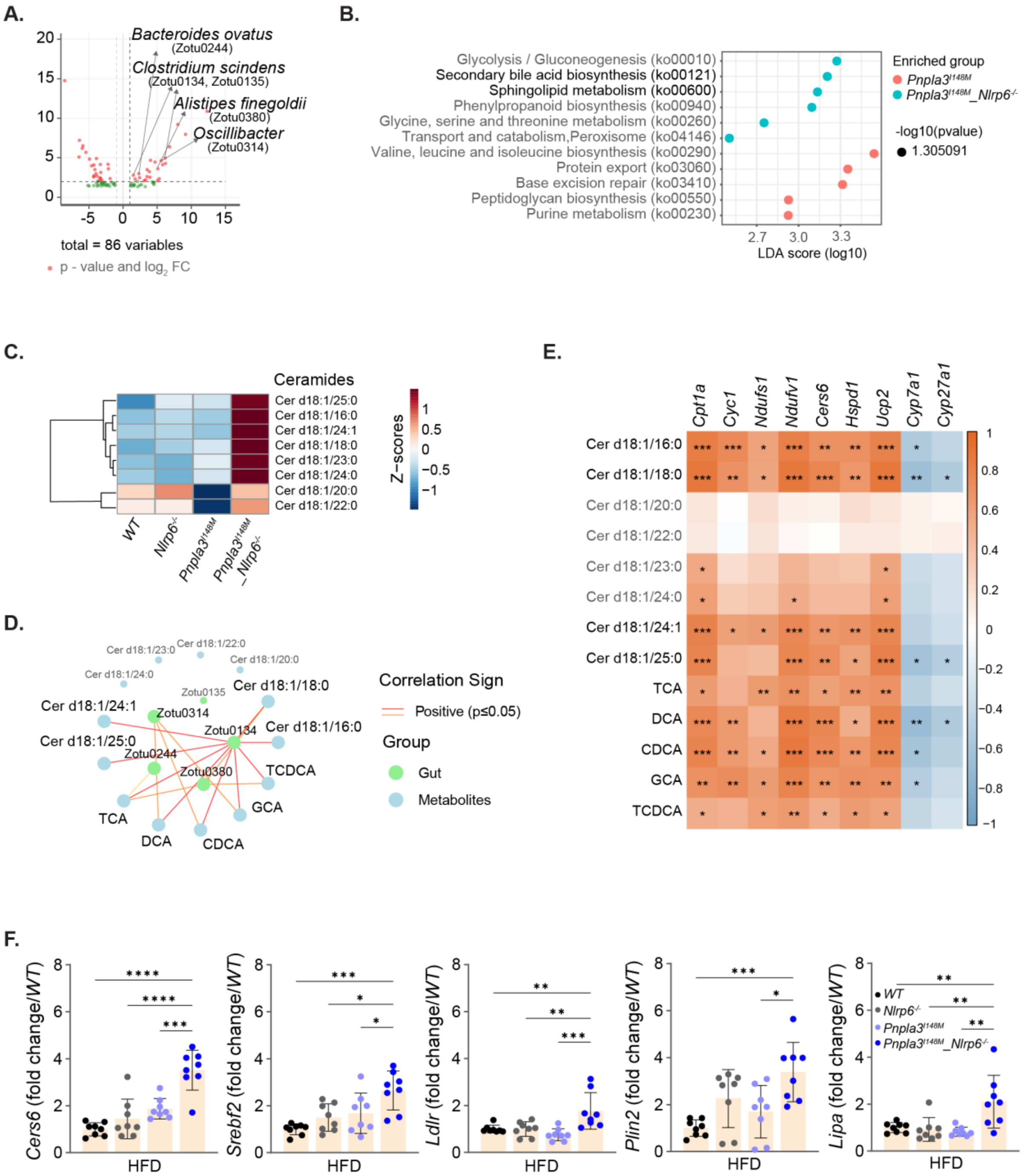

Figure 20: Microbiota-driven disruption of the bile acid–ceramide–mitochondrial axis promotes MASLD in *Pnpla3^{I148M}_Nlrp6$^{-/-}$* mice. (A) Distinct microbiome composition in *Pnpla3^{I148M}_Nlrp6$^{-/-}$* cohort compared to *Pnpla3^{I148M}*. (B) Metagenomic upregulation of microbial pathways for secondary bile acid and sphingolipid metabolism. (C-E) Elevated portal ceramide species and their correlations (Pearson, $|r| \geq 0.5$, $p < 0.05$) with microbial taxa and hepatic transcriptomes (TPM-normalized)

(n=5). (F) Hepatic expression of lipid-metabolism associated genes. Statistical analysis was performed using one-way ANOVA (Brown-Forsythe or Bartlett's test for variance homogeneity) with Tukey's post hoc test ($\alpha = 0.05$). Data are presented as scatter dot plots (mean ± SD), with individual points representing biological replicates unless otherwise noted. Significance thresholds denoted as: *$^{*}P \leq 0.05$*, *$^{**}P < 0.01$*, *$^{***}P < 0.001$*, and *$^{****}P < 0.0001$*.

4.4. Gut microbiota dependency in MASLD pathogenesis

4.4.1. Gut microbiota depletion with antibiotics reverses metabolic disturbances

To investigate whether the observed metabolic disturbances were dependent on the gut microbiota, mice of all genotypes were treated with a broad-spectrum antibiotic (AB) cocktail via drinking water for eight weeks, in parallel with HFD feeding (Figure 21A). Following completion of the treatment, successful microbiota depletion was quantitatively confirmed through comprehensive alpha diversity analysis, which revealed statistically significant reductions in both Shannon ($p < 0.0001$) and Chao1 ($p < 0.0001$) indices compared to untreated HFD-fed cohorts (Figure 21B).

AB-treated mice of all genotypes demonstrated a significant reduction in liver weight and hepatic triglyceride content, with an average decrease of 38% compared to untreated HFD-fed cohorts (Figure 21C-D). Importantly, this effect occurred despite comparable food and water intake between groups (Figure 21E), ruling out differences in caloric intake as the cause. Biochemically, serum ALT levels were significantly reduced (Figure 21F), reflecting attenuated liver injury.

Portal serum metabolomics demonstrated significant downregulation of steatotic metabolites in AB-treated *Pnpla3*^{I148M}*_Nlrp6*$^{-/-}$ cohort compared to HFD-treated counterpart, revealing three key microbial-dependent pathways: (1) bile acid metabolism (reduced non-12α-OH species, DCA, TCA, TDCA, GCA, TLCA), (2) sphingolipid signaling (decreased pathogenic ceramides), and (3) bacterial co-metabolite production (lowered TMAO and p-Cresol-SO4) (Figure 21G).

To assess microbial–metabolite associations, MaAsLin2 was applied. Relative abundances of the microbiota signature (e.g., *Clostridium scindens*, *Alistipes finegoldii*, *Oscillibacter*) that was previously identified from HFD-fed *Pnpla3*^{I148M}*_Nlrp6*$^{-/-}$ cohort—were modeled as predictors for the metabolites in a combined dataset of both HFD-fed and HFD+AB-treated cohorts (n=40). This analysis revealed significant and suggestive associations predominantly involving bile acids. Specifically, the relative abundance of *Clostridium scindens* (zotu0134) was positively associated with increased levels of DCA (β = 0.804, *p.adj* = 0.036) while *Oscillibacter* (zotu0314) was also positively associated with increased levels of DCA (β = 0.783, *p.adj* = 0.031) and CDCA (β = 0.187, *p.adj* = 0.036), suggesting a potential microbial influence on bile acid metabolism (Figure 21H).

Strikingly, these microbial-driven metabolic changes translated to systemic improvements. Energy expenditure was significantly increased, accompanied by a reduction in overall fat mass and evidence of browning in BAT (Figure 21I-K), despite continued exposure to the HFD. These changes were further associated with improved glucose tolerance (Figure 21L), suggesting a broader amelioration of metabolic health following microbiota depletion.

These findings collectively demonstrate that the metabolic disturbances observed in *Pnpla3*^{I148M}*_Nlrp6*$^{-/-}$ mice—including hepatic steatosis, mitochondrial dysfunction, and systemic metabolic collapse—are fundamentally dependent on the gut microbiota. Antibiotic-mediated depletion not only reversed key pathological features (e.g., bile acid dysregulation, ceramide accumulation, and liver injury) but also restored systemic energy homeostasis, highlighting the microbiota’s causal role in driving disease progression. The strong microbial-metabolite associations further pinpoint specific taxa as modulators of this pathogenic axis.

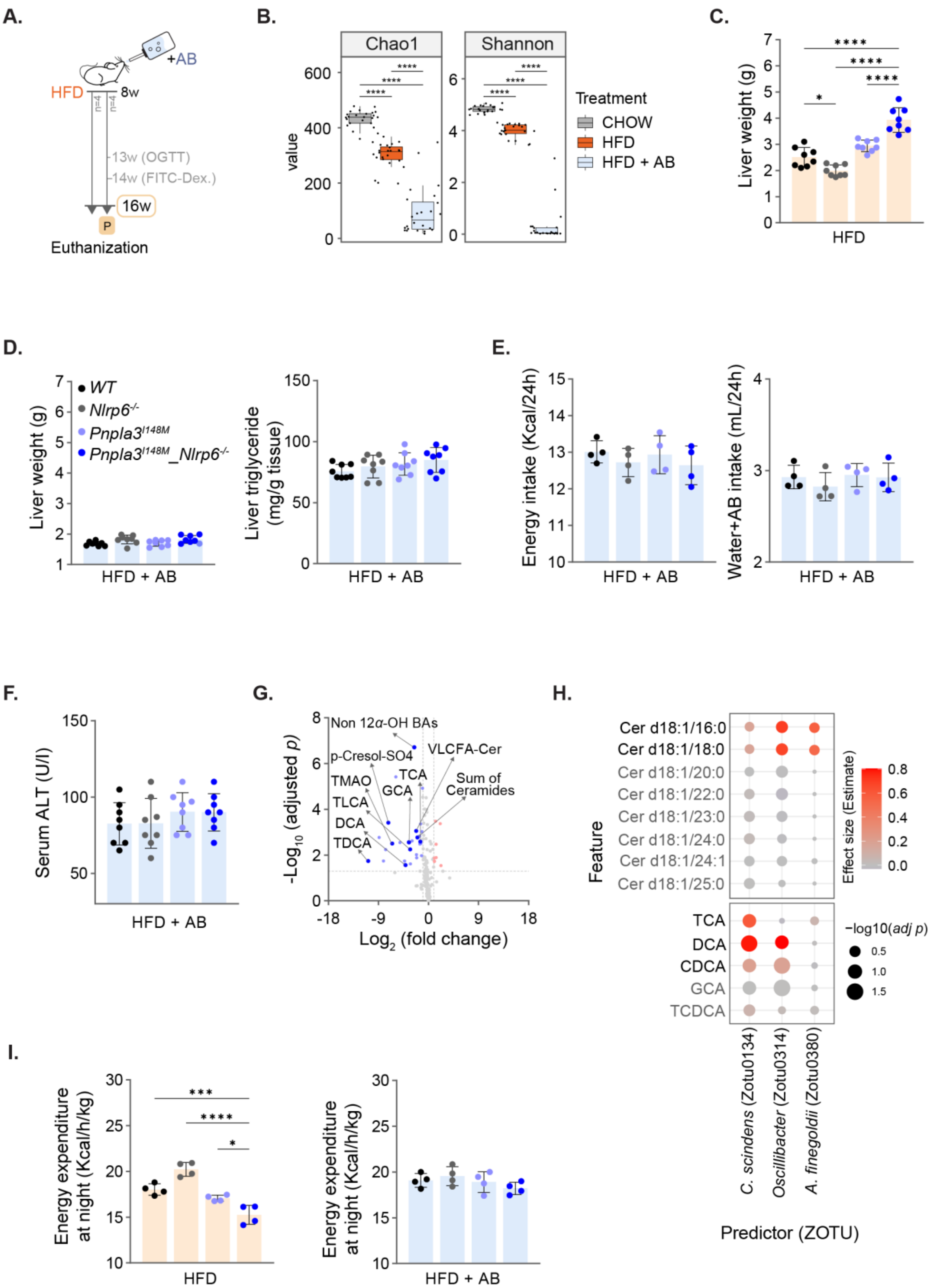
A.
+AB
HFD
8w
n=4
n=4
13w (OGTT)
14w (FITC-Dex.)
16w
P
Euthanization
B.
Chao1
Shannon
value
Treatment
CHOW
HFD
HFD + AB
C.
Liver weight (g)
HFD
D.
WT
Nlrp6-/-
Pnpla3I148M
Pnpla3I148M_Nlrp6-/-
Liver weight (g)
HFD + AB
Liver triglyceride (mg/g tissue)
HFD + AB
E.
Energy intake (Kcal/24h)
HFD + AB
Water+AB intake (mL/24h)
HFD + AB
F.
Serum ALT (U/l)
HFD + AB
G.
-Log10 (adjusted p)
Log2 (fold change)
Non 12α-OH BAs
p-Cresol-SO4
VLCFA-Cer
TMAO
TCA
GCA
Sum of Ceramides
TLCA
DCA
TDCA
H.
Feature
Cer d18:1/16:0
Cer d18:1/18:0
Cer d18:1/20:0
Cer d18:1/22:0
Cer d18:1/23:0
Cer d18:1/24:0
Cer d18:1/24:1
Cer d18:1/25:0
TCA
DCA
CDCA
GCA
TCDCA
Effect size (Estimate)
−log10(adj p)
C. scindens (Zotu0134)
Oscillibacter (Zotu0314)
A. finegoldii (Zotu0380)
Predictor (ZOTU)
I.
Energy expenditure at night (Kcal/h/kg)
HFD
Energy expenditure at night (Kcal/h/kg)
HFD + AB

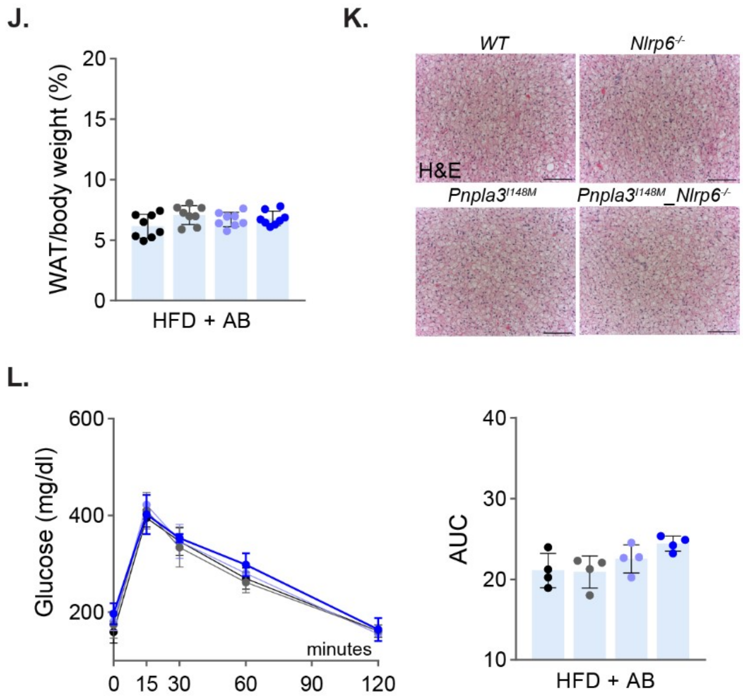

Figure 21: Antibiotic-mediated microbiota depletion attenuates MASLD progression and restores metabolic balance in *Pnpla3^{I148M}_Nlrp6$^{-/-}$* mice.

(A) Experimental design: 8-week AB treatment during HFD feeding (n=8). P denotes Phenomaster. (B) Effective microbiota depletion confirmed by reduced alpha diversity (Shannon and Chao1 indices). (C-D) Decreased liver weight and hepatic triglyceride content following AB treatment compared to untreated HFD-cohorts. (E) Comparable food and water intake. (F) Reduced serum ALT levels. (G) Portal metabolomics revealed downregulation of microbial-dependent metabolites. (H) MaAsLin2 analysis identified microbial predictors of steatotic metabolites (n=40). (I-K) Increased energy expenditure, reduced adiposity, and browning of BAT (H&E; scale bars, 100µm). (L) Improved glucose tolerance despite continued HFD exposure. Statistical analysis was performed using one-way ANOVA (Brown-Forsythe or Bartlett's test for variance homogeneity) with Tukey's post hoc test ($\alpha = 0.05$). Data are presented as scatter dot plots (mean ± SD), with individual points representing biological replicates unless otherwise noted. Significance thresholds denoted as: *$P \leq 0.05$*, **$P < 0.01$*, ***$P < 0.001$*, and ****$P < 0.0001$*.

4.4.2. Dysbiotic microbiota transfer induces metabolic dysfunction and liver injury

Having established that microbiota depletion ameliorates metabolic dysfunction, I next sought to determine whether transfer of a dysbiotic microbiota could conversely induce disease phenotypes. Therefore, I performed dysbiotic fecal microbiota transplantation (dFMT) using stool samples from HFD-fed *Pnpla3*^{I148M}*_Nlrp6*$^{-/-}$ donor mice (Figure 22A). This horizontal microbiota transfer allowed to validate whether reintroducing a pathologically altered microbial community, characterized by dysbiosis and disrupted bile acid metabolism, was sufficient to reproduce key features of metabolic disease in genetically distinct recipients. To facilitate efficient and stable colonization, antibiotic-pretreated *WT* and *Pnpla3*^{I148M} recipient mice were co-housed throughout the dFMT procedure. Control animals received PBS under identical housing and handling conditions, serving as a baseline to account for procedural and environmental variables unrelated to microbiota transfer.

Following transplantation, dFMT recipients exhibited significantly elevated serum FITC-dextran fluorescence compared to PBS-treated controls (Figure 22B), indicating enhanced intestinal permeability. Histological analysis further revealed a visibly thinned colonic inner mucus layer (Figure 22C), reinforcing the presence of barrier dysfunction. Supporting this, the detectable presence of bacterial 16S rRNA in liver tissues of dFMT recipients (Figure 22D) provided direct evidence of microbial translocation across the compromised gut-liver axis. Strikingly, dFMT induced liver weight and hepatic triglyceride accumulation to levels comparable to the original donor mice (Figure 22E-F), indicating functional transmission of the metabolic phenotype. This was accompanied by a significant increase in serum ALT levels and a notable impairment in glucose tolerance (Figure 22G-H), both hallmark features of metabolic dysfunction observed in HFD-fed *Pnpla3*^{I148M}*_Nlrp6*$^{-/-}$ cohort.

Collectively, these findings provide compelling evidence that the dysbiotic microbiota, together with its altered bile acid pool, acts as a key pathogenic driver of gut barrier breakdown, systemic metabolic disturbance, and liver injury. These results highlight the transmissibility and sufficiency of the dysbiotic state in shaping host metabolic outcomes, particularly under conditions of dietary stress.

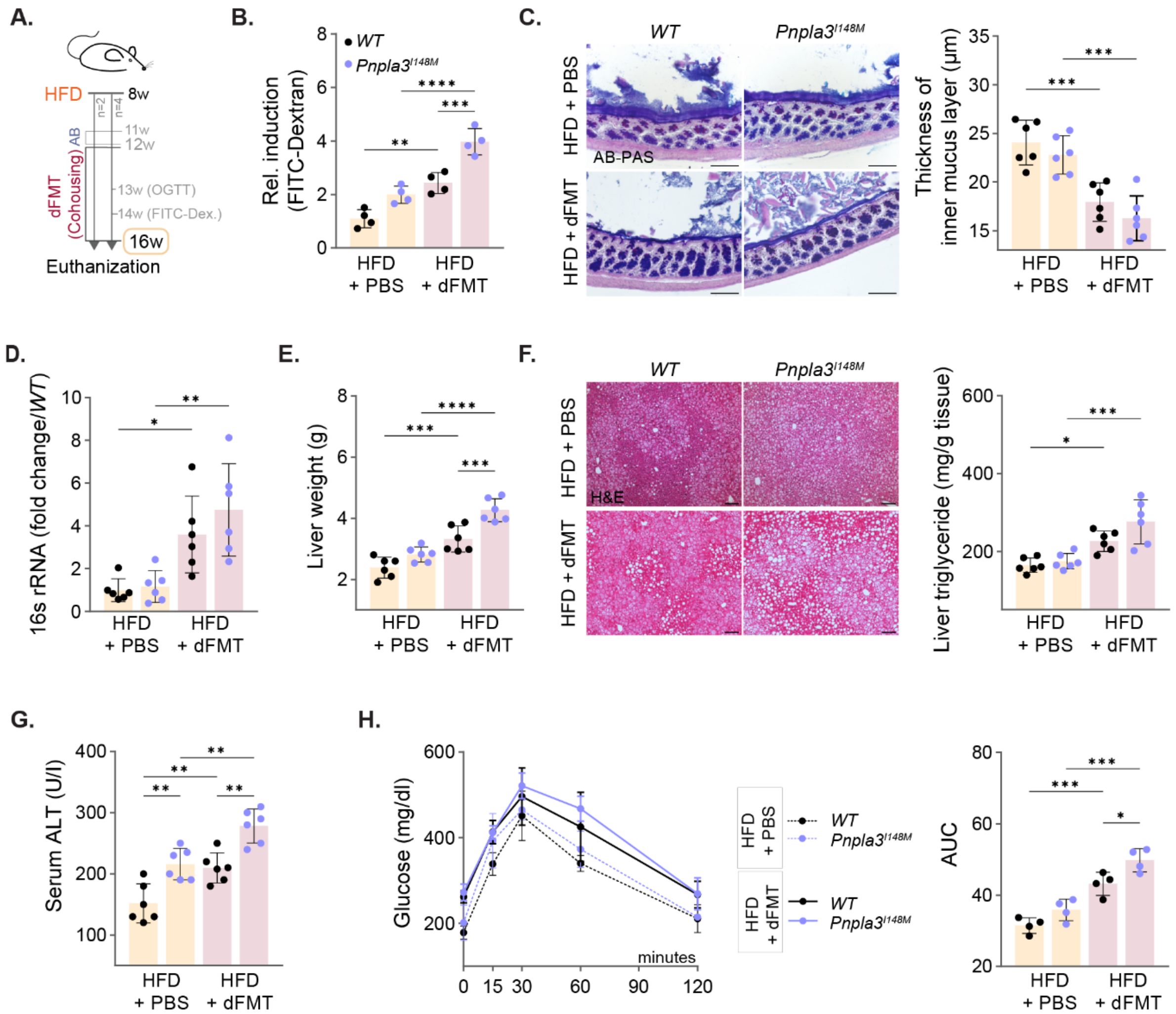

Figure 22: Dysbiotic microbiota transfer recapitulates gut barrier dysfunction and MASLD features in recipient mice. (A) Experimental design of dysbiotic fecal microbiota transplantation (dFMT) from HFD-fed *Pnpla3*^{I148M}_*Nlrp6*$^{-/-}$ donors to antibiotic-pretreated *WT* and *Pnpla3*^{I148M} recipients (n=6). (B) Increased serum FITC-dextran levels in dFMT recipients. (C) Histological evidence of inner mucus layer thinning in the colon post-dFMT (AB-PAS; scale bars, 100µm). (D) Detection of bacterial 16S rRNA in liver tissue confirms microbial translocation. (E-F) Restoration

of liver weight together with hepatic steatosis (H&E; scale bars, 100μm) and triglycerides to donor levels in dFMT recipients. (G-H) Elevated serum ALT and impaired glucose tolerance highlight recapitulation of metabolic dysfunction. Statistical analysis was performed using one-way ANOVA (Brown-Forsythe or Bartlett's test for variance homogeneity) with Tukey's post hoc test ($\alpha = 0.05$). Data are presented as scatter dot plots (mean ± SD), with individual points representing biological replicates unless otherwise noted. Significance thresholds denoted as: *$P \leq 0.05$, **$P < 0.01$, ***$P < 0.001$, and ****$P < 0.0001$.

4.5. Long-term dietary insult drives progressive MASLD pathogenesis

Extending high-fat diet (HFD) feeding to 52 weeks (Figure 23A) triggered severe metabolic deterioration, demonstrating the time-dependent escalation of diet-induced pathology. The dramatic expansion of both subcutaneous (inguinal) and visceral (epididymal) fat depots, paired with uncontrolled weight gain (Figure 23B), revealed a breakdown in lipid metabolism and energy regulation. Concurrently, worsening glucose intolerance signaled advancing insulin resistance (Figure 23C), setting the stage for systemic metabolic failure.

In the *Pnpla3*^{I148M}_*Nlrp6*$^{-/-}$ cohort, this dysfunction progressed to irreversible hepatic damage, with striking manifestations: (1) fibrosis and tumorigenesis, indicating late-stage MASH (Metabolic Dysfunction-Associated Steatohepatitis) and reflecting the advanced pathological progression of MASLD; (2) elevated serum ALT, confirming hepatocellular injury; and (3) severe hypertriglyceridemia (~300 mg/dL) (Figure 23D-F), suggesting that chronic dietary stress synergizes with genetic susceptibility to accelerate MASLD progression.

These findings underscore that chronic HFD exposure, in the context of genetic susceptibility initiates a pathogenic cascade driven by early gut microbial remodeling. This dysbiosis disrupts the bile acid–ceramide–mitochondrial axis, creating a self-reinforcing cycle of metabolic dysfunction: impaired hepatic lipid oxidation, exacerbated lipotoxicity, and progressive mitochondrial stress. Over time, this cycle promotes obesity, systemic metabolic collapse, and end-organ damage, fostering a pro-oncogenic microenvironment in the liver. The reversibility of these phenotypes upon microbiota depletion highlights the central role of gut-derived signals in disease progression and positions the microbiome as a promising therapeutic target to intercept *Pnpla3*^{I148M}-driven hepatocarcinogenesis.

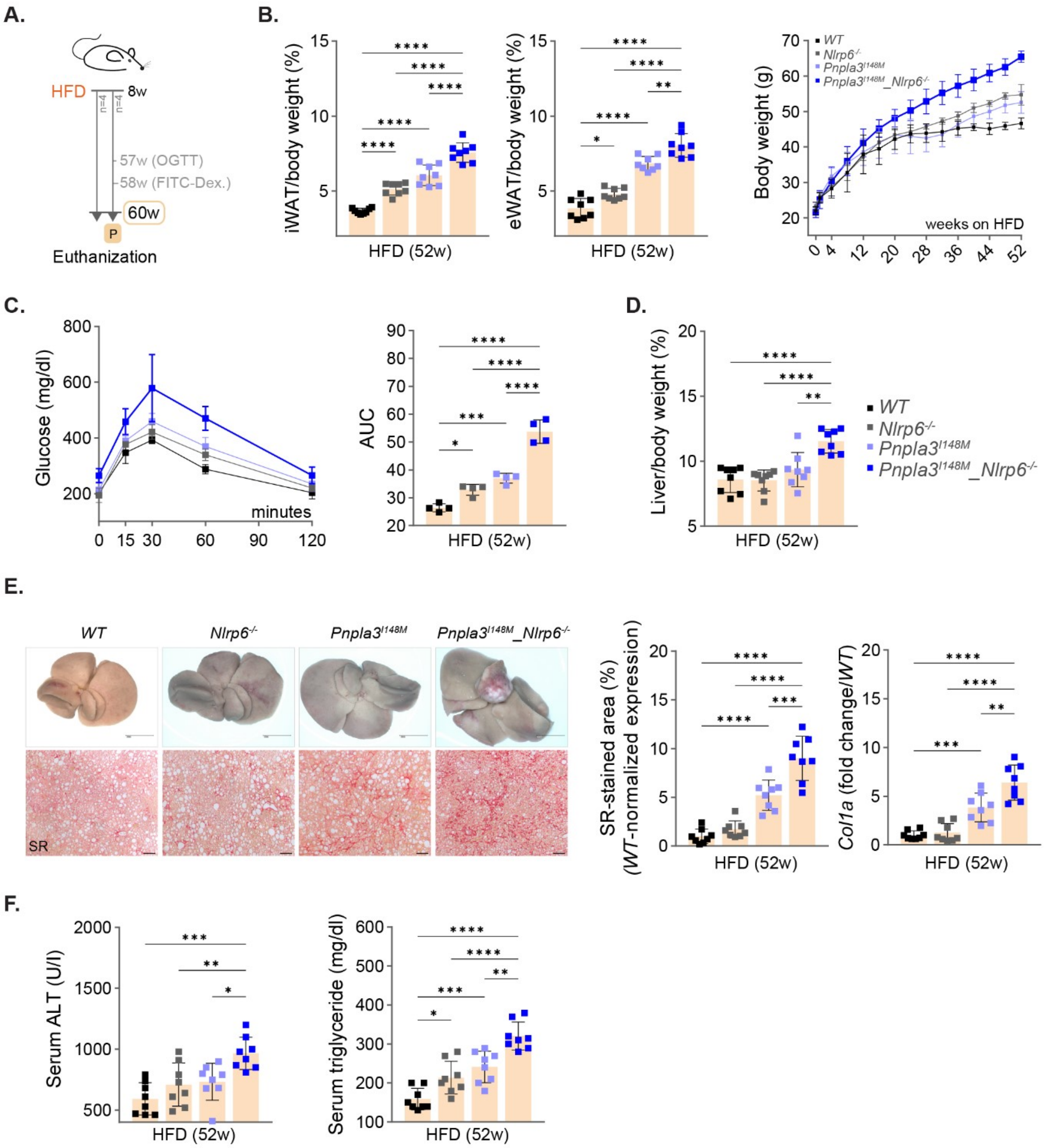

Figure 23: Chronic high-fat diet exacerbates MASLD progression to MASH, fibrosis, and tumorigenesis in *Pnpla3^{I148M}_Nlrp6$^{-/-}$* mice. (A) Experimental timeline of prolonged high-fat diet (HFD) feeding (n=8). P denotes the usage of Phenomaster. (B) Excessive adipose tissue accumulation (inguinal and epididymal fat) and body weight gain. (C) Progressive glucose intolerance. (D-E) Liver pathology in *Pnpla3^{I148M}_Nlrp6$^{-/-}$* cohort: fibrosis (SR; scale bars, 100µm) and tumorigenesis indicating advanced MASH. (F) Elevated serum ALT as a marker of hepatocellular injury and severe hypertriglyceridemia indicative of systemic lipid metabolic collapse.

Statistical analysis was performed using one-way ANOVA (Brown-Forsythe or Bartlett's test for variance homogeneity) with Tukey's post hoc test ($\alpha = 0.05$). Data are presented as scatter dot plots (mean ± SD), with individual points representing biological replicates unless otherwise noted. Significance thresholds denoted as: *$P \leq 0.05$, **$P < 0.01$, ***$P < 0.001$, and ****$P < 0.0001$.

4.6. Gut microbes at the therapeutic crossroads of MASLD

4.6.1. Genotype-specific responses to *Akkermansia* treatment

To assess the influence of microbiota in MASLD progression, I implemented therapeutic strategies aimed at modulating the gut microbial ecosystem in *Pnpla3*^{I148M}_*Nlrp6*$^{-/-}$ cohort. Although the abundance of *Akkermansia muciniphila* (Akk) did not significantly change among untreated HFD-fed cohorts, I explored the therapeutic potential of pasteurized Akk along with its Amuc_1100 protein (Figure 24A), known to enhance gut barrier function and mitigate metabolic inflammation [109]. I opted against broad-spectrum antibiotics to assess whether the effects of preexisting dysbiotic microbial flora could be counteracted.

Both treatment regimens substantially improved gut barrier integrity and mitigated metabolic disturbances, as evidenced by reduced gut permeability, body and liver weight gain (Figure 24B-D), and decreased hepatic lipid accumulation compared to untreated HFD-fed controls (Figure 24E). However, these benefits exhibited clear genotype-specific differences: while *WT* and *Nlrp6*$^{-/-}$ cohorts demonstrated pronounced metabolic improvements, *Pnpla3*^{I148M} and *Pnpla3*^{I148M}_*Nlrp6*$^{-/-}$ cohorts retained significantly elevated hepatic triglyceride levels and persistent steatosis. These findings suggest that the *Pnpla3*^{I148M} risk variant imposes a genetic constraint on the efficacy of microbiota-targeted interventions, limiting full metabolic recovery despite improvements in gut homeostasis.

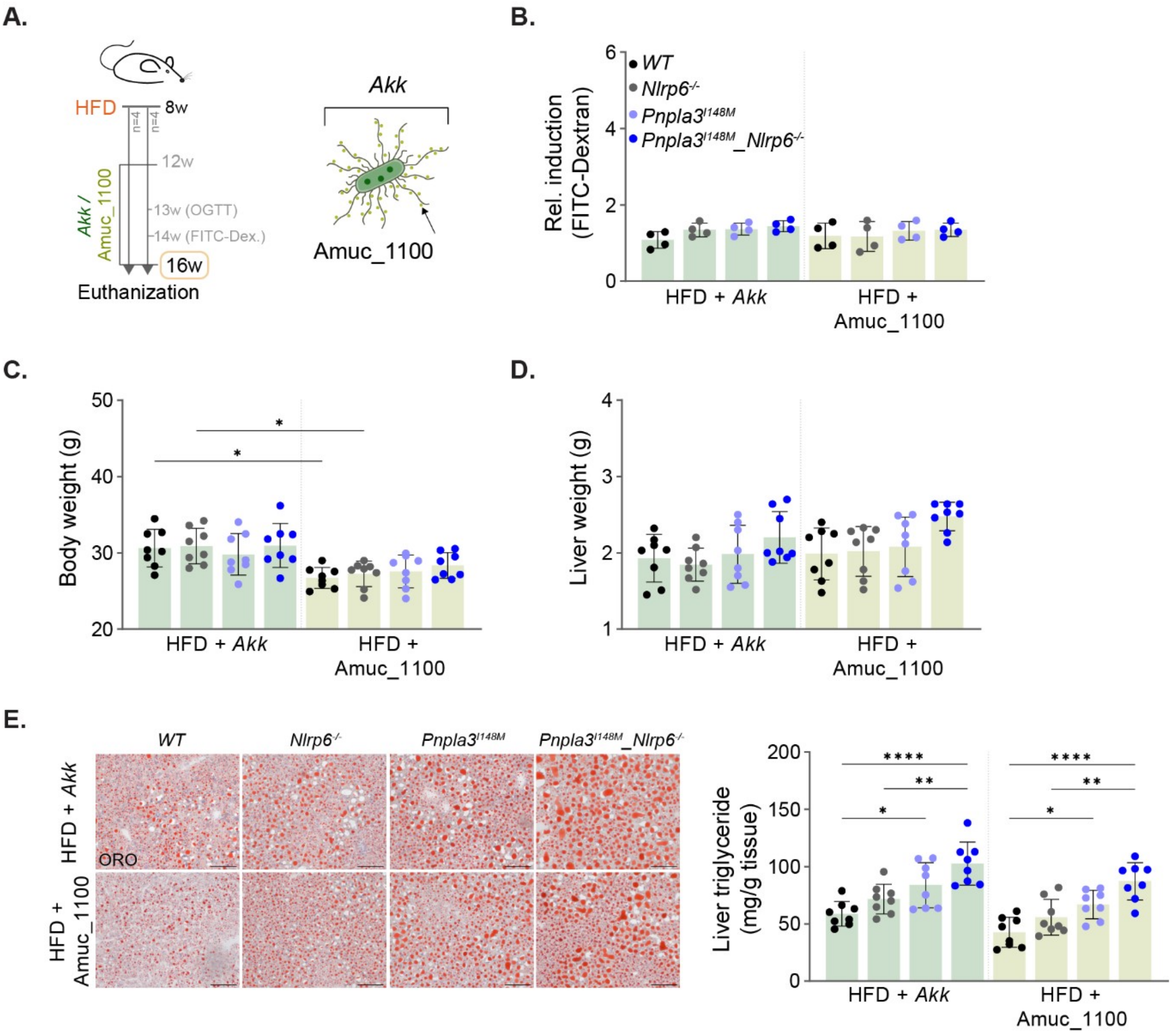

Figure 24: Microbiota-targeted therapy with pasteurized *Akkermansia muciniphila* and Amuc_1100 protein improves gut integrity and metabolic health in a genotype-dependent manner. (A) Experimental design: therapeutic intervention using pasteurized *A. muciniphila* and Amuc_1100 protein in HFD-fed mice (n=8). (B-D) Reduced gut permeability, body weight, and liver weight following treatment. (E) Decreased hepatic lipid accumulation, with differential effect in *Pnpla3I148M* and *Pnpla3*^{I148M}*_Nlrp6*$^{-/-}$ cohorts (ORO; scale bars, 100µm). Statistical analysis was performed using one-way ANOVA (Brown-Forsythe or Bartlett's test for variance homogeneity) with Tukey's post hoc test (α = 0.05). Data are presented as scatter dot plots (mean ± SD), with individual points representing biological replicates unless otherwise noted. Significance thresholds denoted as: **P ≤ 0.05*, ***P < 0.01*, ****P < 0.001*, and *****P < 0.0001*.

4.6.2. eFMT's full-spectrum microbial reinforcement

16s rRNA microbial profiling in mice identified a marked reduction in bile salt hydrolase (BSH)-expressing Firmicutes in HFD-fed cohorts relative to CHOW-fed cohorts [110] (Figure 25A). This finding was consistent with patterns observed in human carriers.

While single-strain interventions showed genotype-constrained benefits, I next implemented eubiotic fecal microbiota transplantation (eFMT) to determine whether complete ecological restoration with increased the proportion of Firmicutes could bypass genetic susceptibility in *Pnpla3*^{I148M} carriers. This approach allowed me to test whether wholesale microbiome reconstitution might compensate for host genetic risk factors in MASLD pathogenesis.

Aligning with circadian microbial rhythms, I collected the donor fecal material for eFMT from CHOW-fed *WT* mice at 7.00 – 7.10 AM - the documented peak of Firmicutes abundance [111] (Figure 25B) - targeting three specific outcomes: (1) reestablishment of BSH-capable taxa, (2) microbial community rehabilitation, and (3) assessment of metabolic rescue capacity in genetically susceptible hosts.

The eFMT intervention successfully reconstituted gut microbial architecture, evidenced by Firmicutes expansion and enhanced Chao1 diversity indices (Figure 25A, 25C), effectively normalizing the dysbiotic profile. This approach outperformed previously employed pasteurized Akk and Amuc_1100 based strategies, demonstrating comprehensive metabolic improvements including: decreased hepatic lipid accumulation, and strengthened intestinal barrier integrity (Figure 25D). Metabolomic analysis of portal circulation revealed eFMT-mediated metabolic reprogramming in *Pnpla3*^{I148M}_*Nlrp6*$^{-/-}$ cohort compared to their HFD-fed counterparts, characterized by: (1) depletion of hepatotoxic bile acid species (including TCA, DCA, GCA, and 12α-OH derivatives) and ceramides including Cer(d18:1/16:0) and Cer(d18:1/18:0); (2) elevation of protective lipid species (MUFA/PUFA triglycerides, ω-3 fatty acids) and microbial-modulated anti-inflammatory metabolites (3-indolepropionic acid) (Figure 25E-F). This was accompanied by a marked improvement in the hepatic inflammatory microenvironment, characterized by: (1) significant downregulation of pro-inflammatory cytokines (*TNF-α*, *IL-1β*, and *IL-6*); and (2) reduced neutrophil infiltration - suggesting a transition toward an immune-tolerant hepatic niche. (Figure 25G-H).

This intervention also led to significant improvements in adipose tissue function, as evidenced by a reduction in adipocyte hypertrophy and the restoration of leptin signaling to more physiological levels (Figure 25I-J). These changes suggest improved adipose tissue homeostasis and endocrine function, both of which are critical in modulating systemic metabolic health [32].

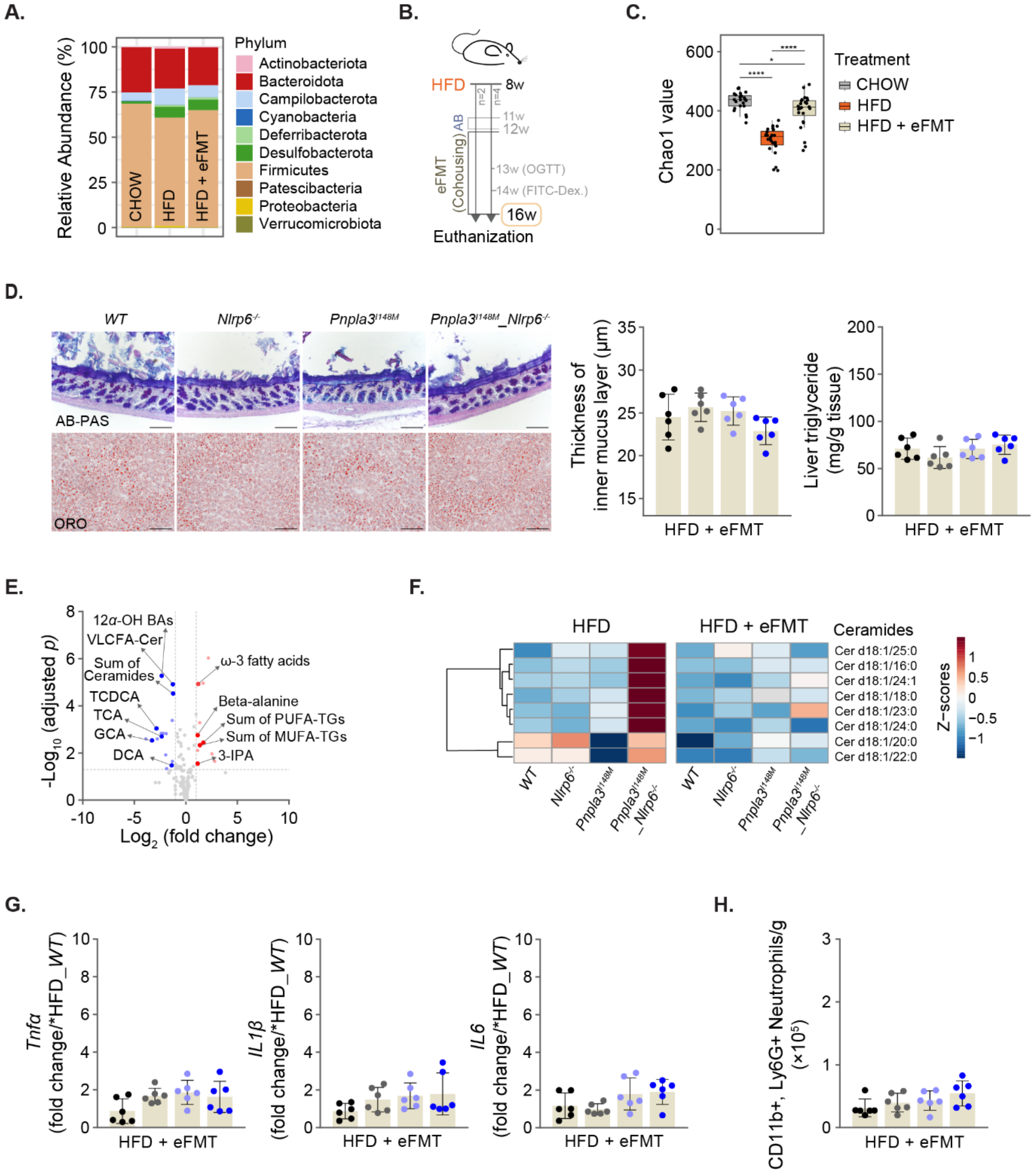
A.
Relative Abundance (%)
CHOW
HFD
HFD + eFMT
Phylum
Actinobacteriota
Bacteroidota
Campilobacterota
Cyanobacteria
Deferribacterota
Desulfobacterota
Firmicutes
Patescibacteria
Proteobacteria
Verrucomicrobiota
B.
HFD
8w
11w
12w
13w (OGTT)
14w (FITC-Dex.)
16w
eFMT (Cohousing) AB
Euthanization
C.
Chao1 value
Treatment
CHOW
HFD
HFD + eFMT
D.
WT
Nlrp6-/-
Pnpla3I148M
Pnpla3I148M_Nlrp6-/-
AB-PAS
ORO
Thickness of inner mucus layer (μm)
Liver triglyceride (mg/g tissue)
HFD + eFMT
E.
-Log10 (adjusted p)
Log2 (fold change)
12α-OH BAs
VLCFA-Cer
Sum of Ceramides
TCDCA
TCA
GCA
DCA
ω-3 fatty acids
Beta-alanine
Sum of PUFA-TGs
Sum of MUFA-TGs
3-IPA
F.
HFD
HFD + eFMT
Ceramides
Cer d18:1/25:0
Cer d18:1/16:0
Cer d18:1/24:1
Cer d18:1/18:0
Cer d18:1/23:0
Cer d18:1/24:0
Cer d18:1/20:0
Cer d18:1/22:0
Z-scores
G.
Tnfα (fold change/*HFD_WT)
IL1β (fold change/*HFD_WT)
IL6 (fold change/*HFD_WT)
HFD + eFMT
H.
CD11b+, Ly6G+ Neutrophils/g (×10^5)
HFD + eFMT

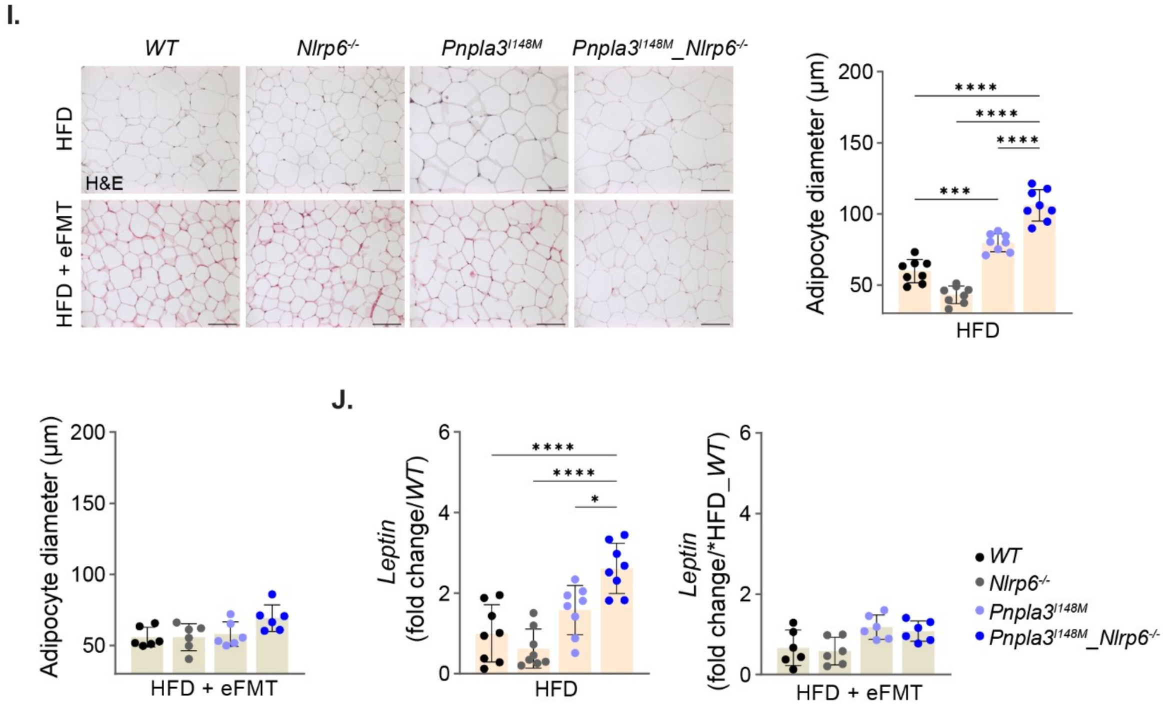

Figure 25: Eubiotic fecal microbiota transplantation (eFMT) restores microbial ecology and reverses MASLD phenotypes in *Pnpla3^{I148M}_Nlrp6$^{-/-}$* mice. (A–C) eFMT from CHOW-fed *WT* donors reestablishes bile salt hydrolase–expressing Firmicutes and improves alpha diversity (n=6). (D) eFMT enhances gut barrier integrity (AB-PAS; scale bars, 100μm) and reduces hepatic steatosis (ORO; scale bars, 100μm). (E-F) Portal metabolomics reveal depletion of pathogenic bile acids and ceramides with increased protective lipids and anti-inflammatory metabolites. (G-H) Hepatic cytokine expression is reduced with less neutrophil infiltration. (I-J) eFMT improves adipose tissue architecture (H&E; scale bars, 100μm) and leptin signaling. Statistical analysis was performed using one-way ANOVA (Brown-Forsythe or Bartlett's test for variance homogeneity) with Tukey's post hoc test (α = 0.05). Data are presented as scatter dot plots (mean ± SD), with individual points representing biological replicates unless otherwise noted. Significance thresholds denoted as: **P ≤ 0.05*, ***P < 0.01*, ****P < 0.001*, and *****P < 0.0001*.

4.6.3. Mechanistic basis for eFMT's superior efficacy over *Akkermansia* and Amuc_1100 in genetically susceptible hosts

The differential therapeutic outcomes between *Akkermansia muciniphila* (Akk) supplementation and eubiotic fecal microbiota transplantation (eFMT) stem from genetic susceptibility. Pasteurized Akk and its Amuc_1100 protein are primarily aimed at enhancing mucosal barrier integrity and reducing localized gut inflammation [109]. While these interventions improved gut permeability and partially alleviated metabolic disturbances such as weight gain and hepatic lipid accumulation, they failed to counteract the combined effects of *Pnpla3*^{I148M} genetic predisposition and dietary stress [44].

In contrast, following eFMT, LEfSe analysis identified significant differences in microbial taxa between the HFD and HFD+eFMT groups in *Pnpla3*^{I148M}_*Nlrp6*$^{-/-}$ cohorts (LDA score > 1, $p < 0.05$) (*validated using EzBioCloud, confirming > 98% sequence similarity*) (Figure 26A). eFMT induced broad-spectrum microbial reconstitution, reintroducing functionally diverse taxa that mitigated pathological signatures of metabolic dysregulation. Notably, this included: (1) butyrate producers such as *Pseudobutyrivibrio ruminis* and *Intestinimonas butyriciproducens*, which enhance gut barrier integrity, reduce systemic inflammation, and support lipid metabolism [127-128]; (2) immunoregulatory species such as *Lactobacillus johnsonii* and *Lactobacillus reuteri*, which modulate bile acid metabolism via bile salt hydrolase (BSH) activity and reinforce mucosal immune tolerance [129-130]; (3) tryptophan-metabolizing bacteria such as *Clostridium sporogenes*, which produce 3-indolepropionic acid (IPA)—a potent reliever of oxidative stress that promotes hepatic homeostasis [131]. Complementing these microbial shifts, metagenomic analyses further demonstrated a significant upregulation of metabolic pathways involved in fatty acid degradation (*ko00071*) and butanoate metabolism (*ko00650*) (Figure 26B). These changes coincided with an associated downregulation of pathways previously described as driving factors of MASLD in the 'dual model'.

As a metabolic consequence of eFMT, the liver underwent a profound metabolic rewiring, enhancing pathways related to fat metabolism—including *mmu01212*, *mmu04975*, and *mmu04979*—and increasing thermogenesis (*mmu04714*) (Figure 26C). This hepatic adaptation likely served as a compensatory mechanism to counteract lipid accumulation and metabolic stress despite HFD-feeding. Additionally, there is a notable downregulation of reactive oxygen species (ROS) production alongside suppression of the inflammation-associated PI3K–Akt signaling pathway (*mmu04151*) (Figure 26C), further supporting a reduction in oxidative damage and inflammatory signaling.

Taken together, these findings underscore the superior efficacy of eFMT in genetically susceptible hosts by facilitating a multifaceted restoration of gut microbial diversity and function, which in turn drives beneficial metabolic and immunological adaptations within the host. This integrated microbial-host interaction appears essential for overcoming the limitations of targeted probiotic supplementation strategies such as those involving *Akkermansia muciniphila* and its Amuc_1100 protein.

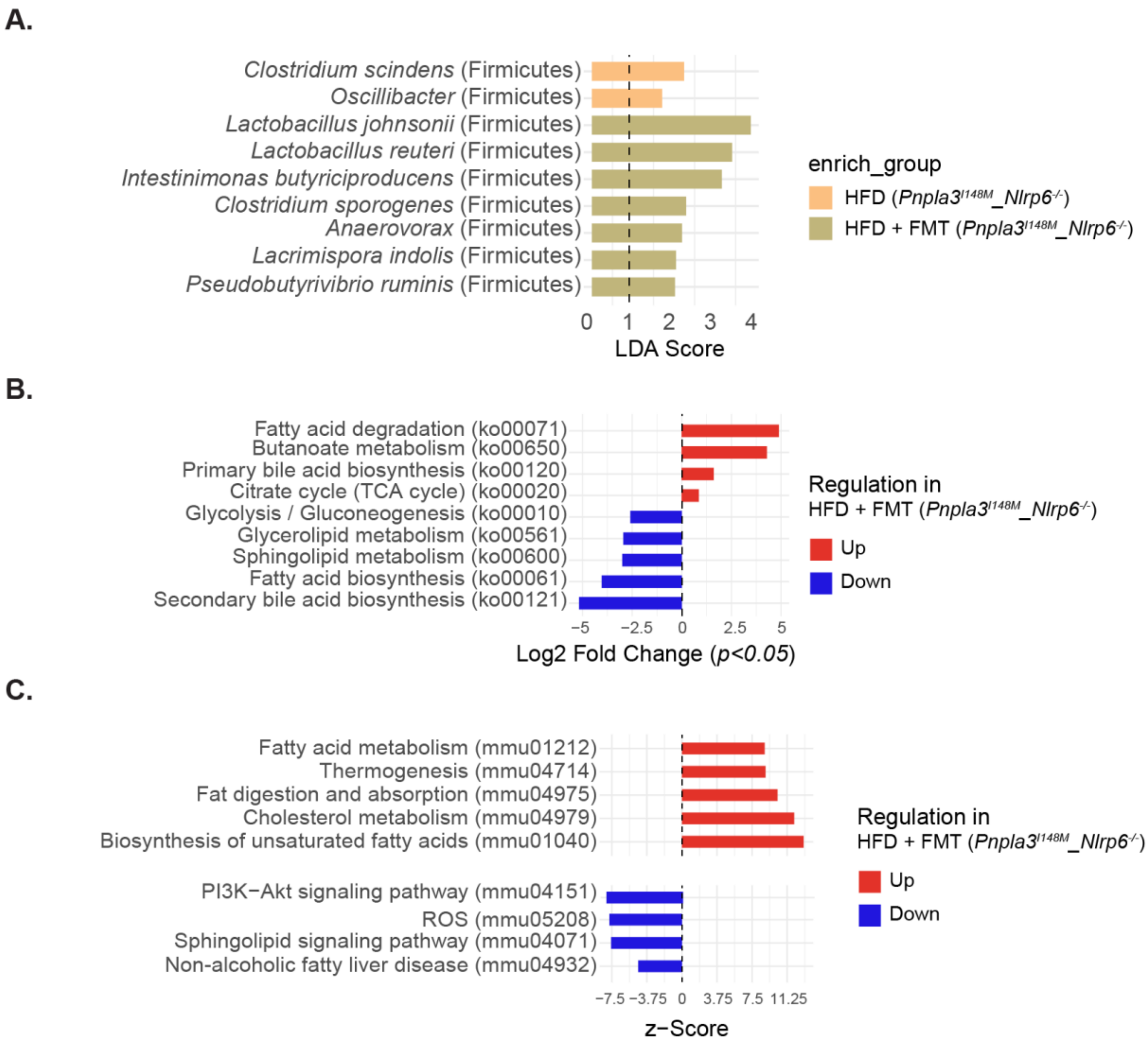

Figure 26: eFMT introduces broad microbial reconstitution and metabolic rewiring in *Pnpla3^{I148M}_Nlrp6$^{-/-}$* mice. (A) LEfSe analysis showing significant shifts in microbial taxa between HFD and HFD+eFMT treated *Pnpla3^{I148M}_Nlrp6$^{-/-}$* cohorts. (B) Metagenomic pathways upregulated by eFMT (*p<0.05*). (C) Hepatic metabolic adaptations post-eFMT (TPM-normalized counts).

5. DISCUSSION

5.1. *PNPLA3^{I148M}* and gut microbiota: a conditional metabolic partnership

The *PNPLA3^{I148M}* variant has been widely implicated in hepatic lipid accumulation and MASLD progression [39, 40], yet the influence of gut microbiota composition on disease manifestation remained unclear prior to this study. The analysis of 146 MASLD patients revealed no significant differences in microbial diversity between *PNPLA3^{I148M}* carriers and non-carriers, suggesting that this genetic variant alone is insufficient to reshape the landscape of the gut microbiome. This finding aligns with broader literature indicating that host genetics typically exert only modest effects on microbial communities unless interacting with environmental factors such as diet or metabolic disease [112, 113]. However, while the *PNPLA3^{I148M}* variant may not directly alter microbiota structure, it creates a latent metabolic vulnerability that becomes clinically apparent under dysbiotic conditions. This was particularly evident in carriers with hypertriglyceridemia (>150 mg/dL), where gut microbial composition accounted for 14.54% of the variation in serum triglyceride levels. These observations position *PNPLA3^{I148M}* as a genetic amplifier of dysbiosis-induced metabolic dysfunction, explaining why some carriers develop severe MASLD despite minimal traditional risk factors [50].

The interaction between *PNPLA3^{I148M}* and adiposity further underscores its context-dependent pathogenicity. In non-carriers, BMI showed almost no correlation with triglyceride levels, whereas in carriers, each unit increase in BMI was associated with a 6.56 mg/dL rise in triglycerides ($p = 0.021$). This finding mirrors clinical reports of "lean MASLD," where *PNPLA3^{I148M}* carriers exhibit metabolic disturbances at lower BMIs than non-carriers [39, 40, 114]. The variant’s ability to enhance lipid sensitivity suggests that it may exacerbate the metabolic consequences of obesity-related dysbiosis, creating a feedforward loop of hepatic lipid accumulation and systemic inflammation. Collectively, these results highlight the importance of considering both genetic and microbial risk factors in MASLD stratification.

5.2. Dual-hit pathogenesis: synergy between genetics and dysbiosis

The development of MASLD has long been conceptualized as a "two-hit" process, with initial steatosis followed by inflammatory injury [52-60]. This study extends this paradigm by demonstrating that genetic susceptibility (*Pnpla3*^{I148M}) and metagenomic disturbances can synergize to drive disease even in the absence of dietary excess. The *Pnpla3*^{I148M}*_Nlrp6*$^{-/-}$ mouse model was specifically designed to test this interaction, as *Nlrp6* loss promotes dysbiosis and disrupts gut barrier function [85], mimicking common features of human MASLD. Remarkably, these mice developed glucose intolerance by 16 weeks on a CHOW diet and progressed to full MASLD pathology, including steatosis, inflammation, and hypertriglyceridemia by 60 weeks. This spontaneous disease progression underscores the sufficiency of genetic-microbial synergy to trigger MASLD without the need for exogenous dietary insults, providing a compelling model for studying "MASLD" in humans.

Lipidomic analysis of age-progressed *Pnpla3*^{I148M}*_Nlrp6*$^{-/-}$ livers revealed profound disturbances in hepatic lipid metabolism, characterized by the accumulation of triglycerides (e.g., TG 50:2, TG 52:2) and depletion of phosphatidylcholines. This pattern suggests dual defects in lipid droplet dynamics and lipoprotein secretion, consistent with the known role of PNPLA3 in hydrolyzing triglycerides and remodeling lipid droplets [38]. The depletion of phosphatidylcholines may further impair hepatic lipid export, exacerbating steatosis. These findings align with prior work showing that *PNPLA3*^{I148M} disrupts lipid droplet turnover and promotes lipid retention in hepatocytes, but they also highlight how dysbiosis amplifies these effects by altering systemic lipid metabolism [38, 100]. The *Pnpla3*^{I148M}*_Nlrp6*$^{-/-}$ model thus provides a unique platform for dissecting the mechanistic links between gut microbiota, hepatic lipid handling, and genetic risk, offering insights that could inform personalized therapeutic strategies for MASLD patients.

5.3. Dietary stress accelerates metabolic collapse via gut-liver axis disruption

While the *Pnpla3*^{I148M}*_Nlrp6*$^{-/-}$ mice developed MASLD spontaneously, high-fat diet (HFD) feeding dramatically accelerated disease progression, recapitulating the clinical exacerbation seen in genetically predisposed individuals consuming obesogenic diets [62]. Within just 8 weeks of HFD, these mice exhibited severe gut barrier dysfunction, including mucus layer thinning, bacterial encroachment onto the epithelial surface, and downregulation of tight junction proteins. These structural defects were accompanied by functional impairment, as evidenced by increased intestinal permeability and microbial translocation to the liver. The resulting endotoxemia likely fueled hepatic inflammation, with elevated *TNFα*, *IL-1β*, and *IL-6* and neutrophil infiltration, creating a pro-inflammatory milieu.

A striking paradox emerged in the hepatic transcriptional response to HFD: despite upregulation of PPAR signaling and oxidative phosphorylation pathways, triglyceride levels remained persistently elevated. This disconnect suggests that while the liver attempts to compensate for lipid overload by activating catabolic pathways, mitochondrial dysfunction prevents effective lipid clearance [115]. Key enzymes in β-oxidation were insufficiently expressed, while mitochondrial ROS generators were upregulated, creating a state of redox-energetic failure [116]. This metabolic gridlock was further reflected in whole-body energy metabolism, with reduced oxygen consumption (VO_2) and whitening of brown adipose tissue, indicating a systemic collapse in metabolic flexibility. These findings underscore the centrality of mitochondrial dysfunction in *PNPLA3*^{I148M}–associated MASLD pathogenesis and suggest that therapeutic strategies targeting both lipid metabolism and mitochondrial health may be required to break the cycle of steatosis and inflammation.

5.4. Bile acids and ceramides: microbial mediators of hepatic injury

The gut microbiome exerts profound influence over host metabolism through the production of bioactive metabolites [117], and this current study identified bile acids and ceramides as key mediators of *PNPLA3*^{I148M}-associated MASLD. In *Pnpla3*^{I148M}_*Nlrp6*$^{-/-}$ mice, portal blood was enriched in conjugated primary bile acids (TCA, GCA) and very-long-chain ceramides, while fecal excretion of hydrophobic bile acids (CDCA, DCA) was reduced. This profile points to dysbiosis-driven alterations in bile acid metabolism, likely mediated by microbes such as Clostridium scindens and Bacteroides ovatus, which encode bile salt hydrolases and 7α-dehydroxylases [95-97, 118]. These bacterial enzymes deconjugate and transform primary bile acids into secondary forms, altering their signaling properties and solubility [118]. The retention of hydrophobic bile acids in the gut lumen may further damage the intestinal barrier, perpetuating a cycle of inflammation and metabolic dysfunction [119].

Ceramide accumulation, another hallmark of the *Pnpla3*^{I148M}_*Nlrp6*$^{-/-}$ phenotype, has been linked to glucose intolerance and mitochondrial dysfunction in prior studies [120]. My data suggest that microbial-derived ceramides contribute to hepatic lipid accumulation by impairing β-oxidation and promoting lipid droplet formation. The concurrent depletion of protective phospholipids (e.g., phosphatidylcholines) exacerbates this effect, as these lipids are essential for VLDL assembly and lipid export. Together, these findings position bile acids and ceramides as critical nodes in the gut-liver axis, offering potential targets for therapeutic intervention. Notably, antibiotic treatment reversed these metabolic disturbances, while fecal microbiota transplantation from dysbiotic donors (dFMT) recapitulated them in naïve recipients, providing direct evidence of microbial causality.

5.5. Therapeutic implications: targeting the gut microbiome

The therapeutic arm of this study underscores the promising potential of microbiome-targeted interventions in the management of MASLD, particularly among individuals carrying the *PNPLA3*^{I148M} variant. While pasteurized *Akkermansia muciniphila* and its Amuc_1100 protein improved gut barrier function, their benefits were attenuated in *Pnpla3*^{I148M} carriers. This attenuation points to a gene-microbiome interaction in which the host's genetic background modulates, and potentially constrains, the efficacy of microbial therapies.

In contrast, eubiotic fecal microbiota transplantation (eFMT) using stool from metabolically healthy donors yielded striking metabolic improvements, especially in *Pnpla3*^{I148M} mice. These benefits included reduced hepatic fat accumulation (steatosis), normalization of dysregulated bile acid profiles, and a marked reduction in hepatic and systemic inflammation. The success of eFMT is likely attributable to its capacity to re-establish a diverse and resilient microbial ecosystem capable of restoring metabolic equilibrium across multiple physiological axes. Unlike single-strain interventions, eFMT introduces a broad repertoire of microbial taxa that can synergistically modulate bile acid transformation, ceramide biosynthesis, short-chain fatty acid production, and immune regulation—all critical pathways in the gut-liver axis.

These findings have important clinical implications. First, they suggest that *PNPLA3*^{I148M} carriers may require more comprehensive microbiome restoration than non-carriers to achieve metabolic improvement. Second, they highlight the need for personalized approaches that consider both genetic and microbial risk factors. Future studies should explore whether targeted modulation of bile acid or ceramide metabolism through probiotics, prebiotics, or pharmacological agents can complement microbiome-based therapies in high-risk individuals.

5.6. Limitations and future directions

While this study provides valuable insights into the role of gut dysbiosis in *PNPLA3*^{I148M}-associated MASLD, several limitations must be acknowledged. First, although the murine model successfully recapitulates key aspects of human disease, translational relevance may be limited by species-specific differences in bile acid metabolism (e.g., predominance of taurine-conjugated species in mice) and gut microbiome composition. Second, while the human cohort was carefully phenotyped, the sample size, particularly for subgroup analyses, may restrict the detection of subtle gene-microbiome interactions and limit generalizability across diverse populations. Additionally, preclinical findings with microbiome-modulating therapies like eFMT, though promising, require validation in human trials, especially given challenges in donor selection and engraftment stability [121].

Despite these constraints, the findings open several critical avenues for future research. Comprehensive multi-omics studies in larger, genotyped cohorts could pinpoint microbial and metabolic drivers of disease progression in *PNPLA3*^{I148M} carriers. Humanized mouse models and organoid systems may bridge the gap between mechanistic discoveries and clinical applications. Most urgently, the dysbiosis associated triglyceride shifts observed in both mice and humans highlight the need for clinical trials targeting the gut-liver axis in *PNPLA3*^{I148M} carriers, particularly lean MASLD patients, who currently lack effective therapies. By integrating genetic stratification with microbiome profiling, this work lays the foundation for precision medicine approaches in MASLD.

5.7. Clinical translation and precision medicine potential

These findings underscore the potential of integrating genetic and microbial profiling into precision medicine strategies for MASLD. The observed synergy between *PNPLA3*^{I148M} and dysbiosis challenges the adequacy of current one-size-fits-all management approaches and highlights the need for stratified interventions [122, 123]. Three major translational avenues emerge from this work.

First, the triglyceride-associated microbial signatures identified in *PNPLA3*^{I148M} carriers which accounted for 14.54% of the variance in microbial composition, offer promise as non-invasive biomarkers. These could aid in early risk stratification and longitudinal monitoring, particularly in individuals with normal BMI but high genetic risk.

Second, the observed differential therapeutic responses, especially the attenuated efficacy of *Akkermansia muciniphila* in *Pnpla3*^{I148M} models, support the development of genotype-guided microbiome interventions. This paves the way for tailored treatment strategies that consider host–microbiome–genetic interactions to optimize efficacy and minimize therapeutic failure.

Third, these data indicate that dysbiosis can precede overt metabolic dysfunction in genetically susceptible individuals. This temporal window offers an opportunity for early microbiome modulation, potentially through dietary, probiotic, or pharmacological interventions to prevent disease onset or halt progression before irreversible hepatic injury occurs.

To enable these innovations in clinical practice, several challenges must be addressed. These include the need for standardized, clinically validated microbiome profiling platforms; scalable, affordable genotyping tools; and integration of multi-omics data into routine diagnostic workflows. Moreover, regulatory frameworks for live biotherapeutics and microbiome-based diagnostics will need to evolve in parallel with scientific advances. If addressed thoughtfully, these efforts could usher in a new era of personalized MASLD care, transforming early detection, prevention, and therapeutic precision for at-risk populations.

6. CONCLUSION

This study sheds light on the complex and dynamic interplay between host genetics and the gut microbiome in the pathogenesis of metabolic dysfunction-associated steatotic liver disease (MASLD). I demonstrate that the *PNPLA3*^{I148M} variant, while not inherently disruptive to gut microbial composition, creates a latent metabolic vulnerability that is unmasked under conditions of dysbiosis. Through integrative clinical and experimental approaches, I reveal a synergistic "dual-hit" model, where the convergence of *Pnpla3*^{I148M} and microbial imbalance, exemplified by *Nlrp6* deficiency, drives spontaneous MASLD development independent of dietary overload. This gut-liver axis disruption is further aggravated by HFD exposure, leading to hallmark features of advanced metabolic dysfunction, including altered bile acid signaling, ceramide accumulation and impaired mitochondrial β-oxidation. These findings underscore the central role of gene–microbiome interactions in shaping hepatic vulnerability and disease progression.

Encouragingly, my preclinical therapeutic studies demonstrate that targeting the microbiome, particularly through eubiotic fecal microbiota transplantation can effectively reverse key metabolic and inflammatory derangements. However, the attenuated response in *Pnpla3*^{I148M} carriers highlights the necessity of personalized interventions that account for host genetic background.

By bridging molecular genetics, microbial ecology, and systems metabolism, this work not only advances our understanding of MASLD pathogenesis but also lays the groundwork for more effective and personalized therapeutic strategies in a growing global health challenge.

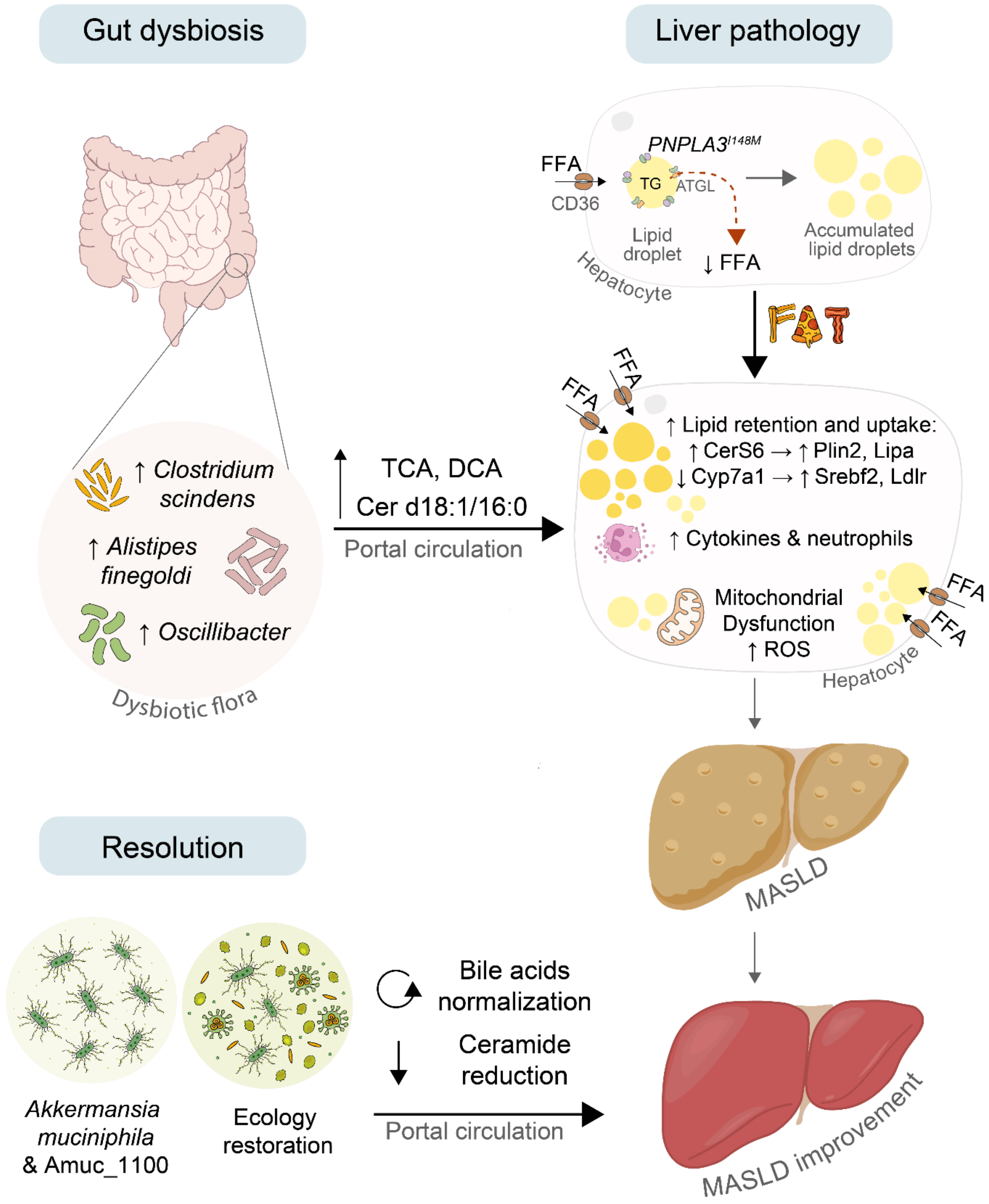

Figure 27: Graphical abstract illustrating gut-liver axis dysregulation in *PNPLA3*^{I148M}-associated MASLD.

The *PNPLA3*^{I148M} variant impairs hepatic triglyceride (TG) hydrolysis, limiting the release of free fatty acids (FFAs) for energy generation or export to peripheral tissues, thereby promoting the accumulation of intracellular lipid droplets.

In the context of obesogenic stress and gut dysbiosis—marked by the pathogenic expansion of *Clostridium scindens*, *Alistipes finegoldii*, and *Oscillibacter*—gut barrier integrity is compromised, allowing translocation of harmful microbial metabolites (e.g., taurocholic acid [TCA], deoxycholic acid [DCA], ceramide d18:1/16:0) into the portal circulation. These metabolites exacerbate lipid retention by suppressing Cyp7a1 while activating Srebf2/Ldlr (lipid influx) and CerS6→Plin2/Lipa (lipid droplet stabilization), with CD36 further amplifying fatty acid uptake. The convergence of *PNPLA3*^{I148M} genetic predisposition and gut-derived metabolic insults triggers macrovesicular steatosis, mitochondrial dysfunction, and ROS-driven inflammation, accelerating MASLD progression.

Therapeutic supplementation with pasteurized *Akkermansia muciniphila*, its outer membrane protein Amuc_1100, and restoration of microbial ecology via eubiotic fecal microbiota transplantation (eFMT) reestablishes gut-liver axis homeostasis, normalizes metabolite flux, and ameliorates hepatic injury.

7. REFERENCES

1. Santos, A. A. et al. Spatial metabolomics and its application in the liver. *Hepatology* 79, 1158–1179 (2024).
2. Trefts, E., Gannon, M. & Wasserman, D. H. The liver. Curr. Biol. 27, R1147–R1151 (2017).
3. Goedeke, L. & Fernández-Hernando, C. Regulation of cholesterol homeostasis. Cell. Mol. Life Sci. 69, 915–930 (2012).
4. Rui, L. Energy metabolism in the liver. *Compr. Physiol.* 4, 177–197 (2014).
5. Houten, S.M. & Wanders, R.J.A. A general introduction to the biochemistry of mitochondrial fatty acid β-oxidation. *J. Inherit. Metab. Dis.* 33, 469–477 (2010).
6. Gibbons, G.F. et al. Synthesis and function of hepatic very-low-density lipoprotein. *Biochem. Soc. Trans.* 32, 59–64 (2004).
7. Adiels, M. et al. Overproduction of very low-density lipoproteins is the hallmark of the dyslipidemia in the metabolic syndrome. *Arterioscler. Thromb. Vasc. Biol.* 28, 1225–1236 (2008).
8. Mansbach, C.M. & Gorelick, F. Development and physiological regulation of intestinal lipid absorption. *Am. J. Physiol. Gastrointest. Liver Physiol.* 293, G645–G650 (2007).
9. Browning, J.D. & Horton, J.D. Molecular mediators of hepatic steatosis and liver injury. *J. Clin. Invest.* 114, 147–152 (2004).
10. Samuel, V.T. & Shulman, G.I. Mechanisms for insulin resistance: common threads and missing links. *Cell* 148, 852–871 (2012).
11. Devarbhavi, H. et al. Global burden of liver disease: 2023 update. *J. Hepatol.* 79, 516–537 (2023).
12. Jacobsen, K. H. Globalization and the changing epidemiology of hepatitis A virus. *Cold Spring Harb. Perspect. Med*. 8 (2018).
13. Rehm, J. et al. Alcohol as a risk factor for liver cirrhosis: a systematic review and meta-analysis. *Drug Alcohol Rev.* 29, 437–445 (2010).
14. Younossi, Z. M. et al. The global epidemiology of nonalcoholic fatty liver disease (NAFLD) and nonalcoholic steatohepatitis (NASH): a systematic review. *Hepatology* 77, 1335–1347 (2023).
15. Yip, T. C. et al. Geographical similarity and differences in the burden and genetic predisposition of NAFLD. *Hepatology* 77, 1404–1427 (2023).
16. Popkin, B.M. & Slining, M.M. New dynamics in global obesity facing low- and middle-income countries. *Obes. Rev.* 14, 11–20 (2013).
17. Softic, S. et al. Fructose and hepatic insulin resistance. *Crit. Rev. Clin. Lab. Sci.* 57, 308–322 (2020).
18. GBD 2016 Alcohol Collaborators. Alcohol use and burden for 195 countries and territories, 1990-2016. *Lancet* 392, 1015–1035 (2018).
19. Targher, G. et al. Risk of cardiovascular disease in patients with nonalcoholic fatty liver disease. *N. Engl. J. Med.* 363, 1341–1350 (2010).

20. Estes, C. et al. Modeling the epidemic of nonalcoholic fatty liver disease demonstrates an exponential increase in burden of disease. *Hepatology* **67**, 123–133 (2018).
21. Hotamisligil, G.S. Inflammation, metaflammation and immunometabolic disorders. *Nature* 542, 177–185 (2017).
22. Friedman, S.L. et al. Mechanisms of NAFLD development and therapeutic strategies. *Nat. Med.* 24, 908–922 (2018).
23. Younossi, Z. M. et al. The global epidemiology of nonalcoholic fatty liver disease (NAFLD) and nonalcoholic steatohepatitis (NASH): a systematic review. *Hepatology* 77, 1335–1347 (2023).
24. Ruze, R. et al. Obesity and type 2 diabetes mellitus: connections in epidemiology, pathogenesis, and treatments. Front. Endocrinol. 14, 1161521 (2023).
25. Loomba, R., Friedman, S. L. & Shulman, G. I. Mechanisms and disease consequences of nonalcoholic fatty liver disease. Cell 184, 2537–2564 (2021).
26. Schwabe, R. F., Tabas, I. & Pajvani, U. B. Mechanisms of fibrosis development in nonalcoholic steatohepatitis. Gastroenterology 158, 1913–1928 (2020).
27. Le, M. H. et al. 2019 Global NAFLD Prevalence: a systematic review and meta-analysis. Clin. Gastroenterol. Hepatol. 20, 2809–2817.e2828 (2022).
28. Wong, V.W. et al. Changing epidemiology, global trends and implications for outcomes of NAFLD. J. Hepatol. 79, 842–852 (2023).
29. Younossi, Z. et al. Nonalcoholic Steatohepatitis Is the Fastest Growing Cause of Hepatocellular Carcinoma in Liver Transplant Candidates. Clin. Gastroenterol. Hepatol. 17, 748–755 (2019).
30. Estes, C. et al. Modeling NAFLD disease burden in China, France, Germany, Italy, Japan, Spain, United Kingdom, and United States for the period 2016-2030. J. Hepatol. 69, 896–904 (2018).
31. European Association for the Study of the Liver (EASL), European Association for the Study of Diabetes (EASD) & European Association for the Study of Obesity (EASO). EASL-EASD-EASO Clinical Practice Guidelines on the management of metabolic dysfunction-associated steatotic liver disease (MASLD). J. Hepatol. 81, 492–542 (2024).
32. Perry, R.J. et al. Hepatic acetyl CoA links adipose tissue inflammation to hepatic insulin resistance and type 2 diabetes. Cell 160, 745–758 (2015).
33. Samuel, V.T. & Shulman, G.I. Nonalcoholic Fatty Liver Disease as a Nexus of Metabolic and Hepatic Diseases. Cell Metab. 27, 22–41 (2018).
34. Singh, S. et al. Fibrosis progression in nonalcoholic fatty liver vs nonalcoholic steatohepatitis: a systematic review and meta-analysis of paired-biopsy studies. Clin. Gastroenterol. Hepatol. 13, 643–e40 (2015).
35. Ekstedt, M. et al. Fibrosis stage is the strongest predictor for disease-specific mortality in NAFLD after up to 33 years of follow-up. Hepatology 61, 1547–1554 (2015).
36. Sookoian, S. & Pirola, C.J. Genetic predisposition in nonalcoholic fatty liver disease. Clin. Mol. Hepatol. 23, 1–12 (2017).

37. Mann, J.P. & Anstee, Q.M. NAFLD: PNPLA3 and obesity: a synergistic relationship in NAFLD. Nat. Rev. Gastroenterol. Hepatol. 14, 506–507 (2017).
38. Johnson, S.M. et al. PNPLA3 is a triglyceride lipase that mobilizes polyunsaturated fatty acids to facilitate hepatic secretion of large-sized very low-density lipoprotein. Nat. Commun. 15, 4847 (2024).
39. Romeo, S. et al. Genetic variation in PNPLA3 confers susceptibility to nonalcoholic fatty liver disease. Nat. Genet. 40, 1461–1465 (2008).
40. Krawczyk, M. et al. Toward Genetic Prediction of Nonalcoholic Fatty Liver Disease Trajectories: PNPLA3 and Beyond. Gastroenterology 158, 1865–1880 (2020).
41. Stender, S. et al. Adiposity amplifies the genetic risk of fatty liver disease conferred by multiple loci. Nat. Genet. 49, 842–847 (2017).
42. Younes, R. & Bugianesi, E. NASH in Lean Individuals. Semin. Liver Dis. 39, 86–95 (2019).
43. Dongiovanni, P. et al. PNPLA3 I148M polymorphism and progressive liver disease. World J. Gastroenterol. 19, 6969–6978 (2013).
44. Luukkonen, P. K. et al. Human PNPLA3-I148M variant increases hepatic retention of polyunsaturated fatty acids. JCI Insight 4, e127902 (2019).
45. Schnabl, B., Damman, C. J. & Carr, R. M. Metabolic dysfunction-associated steatotic liver disease and the gut microbiome: pathogenic insights and therapeutic innovations. J. Clin. Invest. 135, e186423 (2025).
46. Robinson, M. W., Harmon, C. & O'Farrelly, C. Liver immunology and its role in inflammation and homeostasis. Cell. Mol. Immunol. 13, 267–276 (2016).
47. Scheithauer, T. P. M. et al. Gut microbiota as a trigger for metabolic inflammation in obesity and type 2 diabetes. Front. Immunol. 11, 571731 (2020).
48. Silveira, M. A. D. et al. The gut-liver axis: host microbiota interactions shape hepatocarcinogenesis. Trends Cancer 8, 583–597 (2022).
49. Loomba, R. et al. Gut microbiome-based metagenomic signature for non-invasive detection of advanced fibrosis in human nonalcoholic fatty liver disease. Cell Metab. 25, 1054–1062.e5 (2017).
50. Caussy, C. et al. A gut microbiome signature for cirrhosis due to nonalcoholic fatty liver disease. Nat. Commun. 10, 1406 (2019).
51. Le Chatelier, E. et al. Richness of human gut microbiome correlates with metabolic markers. Nature 500, 541–546 (2013).
52. Tilg, H. & Moschen, A. R. Evolution of inflammation in nonalcoholic fatty liver disease: the multiple parallel hits hypothesis. Hepatology 52, 1836–1846 (2010).
53. Neuschwander-Tetri, B. A. Hepatic lipotoxicity and the pathogenesis of nonalcoholic steatohepatitis: the central role of nontriglyceride fatty acid metabolites. Hepatology 52, 774–788 (2010).
54. Schnabl, B. & Brenner, D. A. Interactions between the intestinal microbiome and liver diseases. Gastroenterology 146, 1513–1524 (2014).

55. Henao-Mejia, J. et al. Inflammasome-mediated dysbiosis regulates progression of NAFLD and obesity. Nature 482, 179–185 (2012).
56. Dao, M. C. et al. Akkermansia muciniphila and improved metabolic health during a dietary intervention in obesity: relationship with gut microbiome richness and ecology. Gut 65, 426–436 (2016).
57. Li, D. & Wu, M. Pattern recognition receptors in health and diseases. Signal Transduct. Target. Ther. 6, 291 (2021).
58. Neel, J. V. Diabetes mellitus: a "thrifty" genotype rendered detrimental by "progress"?. Am. J. Hum. Genet. 14, 353–362 (1962).
59. Speliotes, E. K. et al. PNPLA3 variants specifically confer increased risk for histologic nonalcoholic fatty liver disease but not metabolic disease. Hepatology 52, 904–912 (2010).
60. Dongiovanni, P. et al. Causal relationship of hepatic fat with liver damage and insulin resistance in nonalcoholic fatty liver. J. Intern. Med. 283, 356–370 (2018).

61. Valenzuela, D. M. et al. High-throughput engineering of the mouse genome coupled with high-resolution expression analysis. Nat. Biotechnol. 21, 652–659 (2003).
62. Smagris, E. et al. Pnpla3I148M knockin mice accumulate PNPLA3 on lipid droplets and develop hepatic steatosis. Hepatology 61, 108–118 (2015).
63. National Research Council. Guide for the Care and Use of Laboratory Animals. National Research Council, Washington, DC, USA (2011).
64. Plovier, H. et al. A purified membrane protein from Akkermansia muciniphila or the pasteurized bacterium improves metabolism in obese and diabetic mice. Nat. Med. 23, 107–113 (2017).
65. Virtue, S. & Vidal-Puig, A. GTTs and ITTs in mice: simple tests, complex answers. Nat. Metab. 3, 883–886 (2021).
66. Caporaso, J. G. et al. Global patterns of 16S rRNA diversity at a depth of millions of sequences per sample. Proc. Natl Acad. Sci. USA 108 (Suppl 1), 4516–4522 (2011).
67. Edgar, R. C. & Flyvbjerg, H. Error filtering, pair assembly and error correction for next-generation sequencing reads. Bioinformatics 31, 3476–3482 (2015).
68. Quast, C. et al. The SILVA ribosomal RNA gene database project: improved data processing and web-based tools. Nucleic Acids Res. 41 (D1), D590–D596 (2013).
69. McMurdie, P. J. & Holmes, S. phyloseq: an R package for reproducible interactive analysis and graphics of microbiome census data. PLoS ONE 8, e61217 (2013).
70. Oksanen, J. et al. vegan: Community Ecology Package. R package version 2.6-4 (2022).
71. Love, M. I., Huber, W. & Anders, S. Moderated estimation of fold change and dispersion for RNA-seq data with DESeq2. Genome Biol. 15, 550 (2014).

72. Wickham, H. ggplot2: Elegant Graphics for Data Analysis. (Springer-Verlag, New York, 2016).
73. Clum, A. et al. DOE JGI Metagenome Workflow. mSystems 6, e00804-20 (2021).
74. Lesker, T. R. et al. An Integrated Metagenome Catalog Reveals New Insights into the Murine Gut Microbiome. Cell Rep. 30, 2909–2922.e6 (2020).
75. Ye, Y. & Doak, T. G. A parsimony approach to biological pathway reconstruction/inference for genomes and metagenomes. PLoS Comput. Biol. 5, e1000465 (2009).
76. Cao, Y. et al. microbiomeMarker: an R/Bioconductor package for microbiome marker identification and visualization. Bioinformatics 2022, btac438 (2022).
77. Dobin, A. et al. STAR: ultrafast universal RNA-seq aligner. Bioinformatics 29, 15–21 (2013).
78. Li, B. & Dewey, C. N. RSEM: accurate transcript quantification from RNA-Seq data with or without a reference genome. BMC Bioinformatics 12, 323 (2011).
79. Carlson, M. et al. org.Mm.eg.db: Bioconductor organism annotation package for Mouse.
80. Yu, G., Wang, L. G., Han, Y. & He, Q. Y. clusterProfiler: an R package for comparing biological themes among gene clusters. Omics: A Journal of Integrative Biology 16, 284–287 (2012).
81. Yu, G. enrichplot: Visualization of Functional Enrichment Result. R package version 1.26.6 (2025).

82. Ha, S., Wong, V. W., Zhang, X. & Yu, J. Interplay between gut microbiome, host genetic and epigenetic modifications in MASLD and MASLD-related hepatocellular carcinoma. Gut 74, 141–152 (2024).
83. Alberti, K. G., Zimmet, P., Shaw, J. & IDF Epidemiology Task Force Consensus Group. The metabolic syndrome—a new worldwide definition. Lancet 366, 1059–1062 (2005).
84. Su, H. et al. Long-term hypercaloric diet exacerbates metabolic liver disease in PNPLA3 I148M animals. Liver Int. 43, 1699–1713 (2023).
85. Elinav, E. et al. NLRP6 inflammasome regulates colonic microbial ecology and risk for colitis. Cell 145, 745–757 (2011).
86. Cole, L. K., Vance, J. E. & Vance, D. E. Phosphatidylcholine biosynthesis and lipoprotein metabolism. Biochim. Biophys. Acta 1821, 754–761 (2012).
87. Im, Y. R. et al. A systematic review of animal models of NAFLD finds high-fat, high-fructose diets most closely resemble human NAFLD. Hepatology (Baltimore, Md.) 74, 1884–1901 (2021).
88. De Ponti, F. F., Liu, Z. & Scott, C. L. Understanding the complex macrophage landscape in MASLD. JHEP Rep. 6, 101196 (2024).
89. Christofides, A., Konstantinidou, E., Jani, C. & Boussiotis, V. A. The role of peroxisome proliferator-activated receptors (PPAR) in immune responses. Metabolism 114, 154338 (2021).

90. Pan, A. et al. The mitochondrial β-oxidation enzyme HADHA restrains hepatic glucagon response by promoting β-hydroxybutyrate production. Nat. Commun. 13, 386 (2022).
91. Xu, Z. et al. ACAA2 protects against cardiac dysfunction and lipid peroxidation in renal insufficiency with the treatment of S-nitroso-L-cysteine. Biomolecules 15, 364 (2025).
92. Hauck, A. K. & Bernlohr, D. A. Oxidative stress and lipotoxicity. J. Lipid Res. 57, 1976–1986 (2016).
93. Kimura, H. et al. Treatment with atrial natriuretic peptide induces adipose tissue browning and exerts thermogenic actions in vivo. Sci. Rep. 11, 17466 (2021).
94. Park, A., Kim, K., Park, I. et al. Mitochondrial matrix protein LETMD1 maintains thermogenic capacity of brown adipose tissue in male mice. Nat. Commun. 14, 3746 (2023).
95. Studer, N. et al. Functional intestinal bile acid 7α-dehydroxylation by Clostridium scindens associated with protection from Clostridium difficile infection in a gnotobiotic mouse model. Front. Cell. Infect. Microbiol. 6, 191 (2016).
96. Ridlon, J. M. et al. Clostridium scindens: a human gut microbe with a high potential to convert glucocorticoids into androgens. J. Lipid Res. 54, 2437–2449 (2013).
97. Brown, E. M. et al. Bacteroides-derived sphingolipids are critical for maintaining intestinal homeostasis and symbiosis. Cell Host Microbe 25, 668–680.e7 (2019).
98. Johnson, E. L. et al. Sphingolipids produced by gut bacteria enter host metabolic pathways impacting ceramide levels. Nat. Commun. 11, 2471 (2020).
99. Song, X. et al. Microbial bile acid metabolites modulate gut RORγ$^+$ regulatory T cell homeostasis. Nature 577, 410–415 (2020).
100. Brown, E. M., Clardy, J. & Xavier, R. J. Gut microbiome lipid metabolism and its impact on host physiology. Cell Host Microbe 31, 173–186 (2023).
101. Chaurasia, B. & Summers, S. A. Ceramides in metabolism: key lipotoxic players. Annu. Rev. Physiol. 83, 303–330 (2021).
102. Goodwin, B. et al. A regulatory cascade of the nuclear receptors FXR, SHP-1, and LRH-1 represses bile acid biosynthesis. Mol. Cell 6, 517–526 (2000).
103. Horton, J. D., Goldstein, J. L. & Brown, M. S. SREBPs: activators of the complete program of cholesterol and fatty acid synthesis in the liver. J. Clin. Invest. 109, 1125–1131 (2002).
104. Jeon, T. I., Zhu, B., Larson, J. L. & Osborne, T. F. SREBP-2 regulates gut peptide secretion through intestinal bitter taste receptor signaling in mice. J. Clin. Invest. 118, 3693–3700 (2008).
105. McManaman, J. L. et al. Perilipin-2-null mice are protected against diet-induced obesity, adipose inflammation, and fatty liver disease. J. Lipid Res. 54, 1346–1359 (2013).

106. Dempsey, J. L., Ioannou, G. N. & Carr, R. M. Mechanisms of lipid droplet accumulation in steatotic liver diseases. Semin. Liver Dis. 43, 367–382 (2023).
107. Li, F. & Zhang, H. Lysosomal acid lipase in lipid metabolism and beyond. Arterioscler. Thromb. Vasc. Biol. 39, 850–856 (2019).
108. Trigatti, B. L., Krieger, M. & Rigotti, A. Influence of the HDL receptor SR-BI on lipoprotein metabolism and atherosclerosis. Arterioscler. Thromb. Vasc. Biol. 23, 1732–1738 (2003).
109. Belzer, C. & de Vos, W. M. Akkermansia muciniphila: From gut microbiota to host health. Nat. Microbiol. 6, 1449–1458 (2012).
110. Bourgin, M. et al. Bile salt hydrolases: at the crossroads of microbiota and human health. Microorganisms 9, 1122 (2021).
111. Bokoliya, S. C., Dorsett, Y., Panier, H. & Zhou, Y. Procedures for fecal microbiota transplantation in murine microbiome studies. Front. Cell. Infect. Microbiol. 11, 711055 (2021).

112. Rothschild, D. et al. Environment dominates over host genetics in shaping human gut microbiota. Nature 555, 210–215 (2018).
113. Lang, S. et al. Combined analysis of gut microbiota, diet and PNPLA3 polymorphism in biopsy-proven non-alcoholic fatty liver disease. Liver Int. 41, 1576–1591 (2021).
114. Sato-Espinoza, K. et al. Update in lean metabolic dysfunction-associated steatotic liver disease. World J. Hepatol. 16, 452–464 (2024).
115. Moschandrea, C. et al. Mitochondrial dysfunction abrogates dietary lipid processing in enterocytes. Nature 625, 385–392 (2024).
116. Zhelev, Z. et al. Over-reduced state of mitochondria as a trigger of "β-oxidation shuttle" in cancer cells. Cancers 14, 871 (2022).
117. Koh, A. & Bäckhed, F. From association to causality: the role of the gut microbiota and its functional products on host metabolism. Mol. Cell 78, 584–596 (2020).
118. Lucas, L. N. et al. Investigation of bile salt hydrolase activity in human gut bacteria reveals production of conjugated secondary bile acids. bioRxiv (2025).
119. Tilg, H., Adolph, T. E. & Trauner, M. Gut-liver axis: Pathophysiological concepts and clinical implications. Cell Metab. 34, 1700–1718 (2022).
120. Diaz-Vegas, A. et al. Mitochondrial electron transport chain, ceramide, and coenzyme Q are linked in a pathway that drives insulin resistance in skeletal muscle. eLife 12, RP87340 (2023).
121. Woodworth, M. H. et al. Challenges in fecal donor selection and screening for fecal microbiota transplantation: A review. Gut Microbes 8, 225–237 (2017).
122. Attar, B. M. & Van Thiel, D. H. Current concepts and management approaches in nonalcoholic fatty liver disease. The Sci. World J. 2013, 481893 (2013).
123. Schattenberg, J. M. et al. A multistakeholder approach to innovations in NAFLD care. Commun. Med. 3, 1 (2023).

124. Harrell, F. E. Jr. Hmisc: Harrell Miscellaneous. R package version 5.2-2, https://CRAN.R-project.org/package=Hmisc (2025).
125. Wei, T. & Simko, V. corrplot: Visualization of a Correlation Matrix. R package version 0.95, https://github.com/taiyun/corrplot (2024).
126. Mallick, H. et al. Multivariable association discovery in population-scale meta-omics studies. PLoS Comput. Biol. 17, e1009442 (2021).
127. Schoch, C. L. et al. NCBI Taxonomy: a comprehensive update on curation, resources and tools. Database 2020, baaa062 (2020).
128. Rampanelli, E. et al. Gut bacterium Intestinimonas butyriciproducens improves host metabolic health: evidence from cohort and animal intervention studies. Microbiome 13, 15 (2025).
129. Tomusiak-Plebanek, A., Mruk, M., Rząca, S., Strus, M. & Arent, Z. In vitro assessment of anti-Campylobacter activity of Lactobacillus strains isolated from canine rectal swabs. BMC Vet. Res. 18, 112 (2022).
130. Foley, M. H. et al. Lactobacillus bile salt hydrolase substrate specificity governs bacterial fitness and host colonization. Proc. Natl Acad. Sci. USA 118, e2017709118 (2021).
131. Sinha, A. K. et al. Dietary fibre directs microbial tryptophan metabolism via metabolic interactions in the gut microbiota. Nat. Microbiol. 9, 1964–1978 (2024).

8. RESEARCH DISSEMINATION

Journal Articles

- Mainz, R. E., Albers, S., **Haque, M.**, Sonntag, R., Treichel, N. S., Clavel, T., Latz, E., Schneider, K. M., Trautwein, C. & Otto, T. NLRP6 inflammasome modulates disease progression in a chronic-plus-binge mouse model of alcoholic liver disease. Cells 11, 182 (2022).

- Su, H., **Haque, M.**, Becker, S., Edlund, K., Duda, J., Wang, Q., Reißing, J., Marschall, H. U., Candels, L. S., Mohamed, M., Sjöland, W., Liao, L., Drexler, S. A., Strowig, T., Rahnenführer, J., Hengstler, J. G., Hatting, M. & Trautwein, C. Long-term hypercaloric diet exacerbates metabolic liver disease in PNPLA3 I148M animals. Liver Int. 43, 1699–1713 (2023).

Conference Posters

- CRC1382: GUT-LIVER AXIS Symposium, 2022, Aachen, Germany. **M. Haque**, H. Su, C. Trautwein. "Functional impact of genetic risk factors for disease progression within the gut-liver axis - results from the *Pnpla3*^{I148M} and *Nlrp6*$^{-/-}$ model of NAFLD" (A08).

- 39. Jahrestagung der Deutschen Arbeitsgemeinschaft zum Studium der Leber 2023, Berlin, Germany. C. Trautwein, H. Su, **M. Haque**, et al. (2023). "PNPLA3 I148M polymorphism aggravates metabolic liver disease under long-term high-fat diet". Z Gastroenterol, 61(01): e30. Poster Visit Session III: Metabolism (incl. NAFLD), 27 January 2023. DOI: 10.1055/s-0042-1759992.

- EASL Congress 2023, Vienna, Austria. H. Su, **M. Haque**, S. Becker, K. Edlund, et al. (2023). "WED-470 PNPLA3 I148M substitution exacerbates NAFLD under a long-term high fat diet". J Hepatol, 78(Supplement 1), S1–S1314. Poster Session, 21–24 June 2023.

- 41. Jahrestagung der Deutschen Arbeitsgemeinschaft zum Studium der Leber 2025, München, Germany. T. B. Raju, A. V. Beckmann, **M. Haque**, et al. (2025). "P3.18 Machine learning identifies microbiome associations with MASLD biomarkers". Z Gastroenterol, 63(01). Poster Session, 14-15 February 2025. DOI: 10.1055/s-0044-1801108.

Oral Presentations

- International Symposium 'Gut-Liver Axis' 2022, RWTH Aachen University, Germany, 06-07 October 2022. **M. Haque**, M. Hatting, J. Reißing, H. Su, C. Trautwein. "Functional impact of *Pnpla3*^{I148M} and *Nlrp6*$^{-/-}$ in NAFLD progression within gut-liver axis" (A08). CRC1382 Collaborative Research Centre.

- CRC1382: GUT-LIVER AXIS Symposium 2023, Aachen, Germany. **M. Haque**, J. Reißing, H. Su, C. Trautwein. "Role of Gut Integrity in *PNPLA3*^{I148M}-Susceptible NAFLD Progression" (A08). RWTH Aachen University.

9. STATUTORY DECLARATION

I, Madhuri Haque, hereby solemnly and sincerely declare the following:

Originality of work

The doctoral dissertation titled "***PNPLA3^{I148M}*-Associated MASLD Susceptibility: The Pivotal Role of Microbiota-Driven Metabolic Dysregulation**" is my own original work, conducted independently unless otherwise explicitly acknowledged. No part of this dissertation has been previously submitted for any degree or academic qualification at this or any other institution.

Third-party contributions

- Supervision:
  - Primary supervisor: Prof. Dr. Kai Markus Schneider, MD, PhD, Department of Gastroenterology, Metabolic Diseases, and Intensive Care Medicine (Medical Clinic III), University Hospital Aachen.
  - Academic mentorship: Prof. Dr. Lars Mathias Blank, Institute of Applied Microbiology, RWTH Aachen University.
- Research facilities:
  - The research was conducted at the Department of Gastroenterology, Metabolic Diseases, and Intensive Internal Medicine (Medical Clinic III), and the animal facility of University Hospital Aachen, utilizing institutional resources as described in Chapter 3.

- Collaborators:
  - Charité-MASLD cohort: Münevver Demir (Department of Hepatology and Gastroenterology, Charité – Universitätsmedizin Berlin).

  - 16S/metagenomic sequencing: Till Robin Lesker & Till Strowig (Helmholtz Centre for Infection Research, Braunschweig).
  - Bile acid profiling: Antonio Molinaro (University of Gothenburg).
  - Metabolomics: Ulrike Rolle-Kampczyk & Martin von Bergen (University of Leipzig).
  - Lipidomics: Gerhard Liebisch (University of Regensburg).
  - Pasteurized *Akkermansia* and Amuc_1100: Anneleen Seger & Willem M. de Vos (Wageningen University).
  - High-Performance Computing (HPC): RWTH Aachen University (Project ID: rwth1786).

- Commercial assistance:
  No paid services (e.g., editing, consulting, or ghostwriting) were used. All external contributions, including reagent synthesis (e.g., primers or antibodies), have been appropriately cited.

Experimental execution

- Design & grant writing: Madhuri Haque & Kai Markus Schneider.
- Animal experiments: Madhuri Haque.
- Sample collection & processing: Madhuri Haque.
- Experimental procedures: Madhuri Haque (with technical contributions from collaborators listed in "Third-party contributions")
- Data generation, collection, processing & visualization: Madhuri Haque.

Declaration of integrity

I affirm that the content, findings, and conclusions presented in this dissertation represent my original work, conducted with academic rigor and integrity. All aspects of the research, including experimental design, data analysis, interpretation, and scholarly writing, were carried out independently unless otherwise explicitly acknowledged.

This dissertation has not been submitted—either in whole or in part—for any other academic degree or qualification. All external contributions, supervisory support, and third-party resources have been duly credited in accordance with academic standards.

I accept full responsibility for the accuracy, ethical compliance, and originality of the research presented herein, and I certify that all sources have been transparently cited to uphold the highest standards of scholarly honesty.

Madhuri Haque

Date: _______________

Signature: __________________________

10. ACKNOWLEDGEMENTS

First and foremost, I would like to express my heartfelt gratitude to my supervisor, Prof. Dr. Kai Markus Schneider, for his unwavering support, thoughtful guidance, and constant encouragement throughout every phase of this doctoral journey. His sharp scientific insight, steady patience, and genuine belief in my potential were a source of both strength and inspiration. Working under his mentorship not only shaped the scientific foundation of this dissertation but also profoundly influenced my personal and professional growth.

I am also deeply thankful to Prof. Dr. Lars Mathias Blank for his generous mentorship and for fostering an environment where interdisciplinary collaboration and curiosity could truly thrive. His thoughtful input and continuous support helped shape the trajectory of this work in meaningful ways.

To my wonderful collaborators across institutions—thank you for generously sharing your expertise; your thoughtful input and support have been instrumental to this work. My heartfelt thanks go to the Department of Gastroenterology, Metabolic Diseases, and Intensive Care Medicine (Medical Clinic III) and the animal facility at the University Hospital Aachen for providing an inspiring research environment, as well as the infrastructure and resources necessary to carry out this work. A special thanks to the technical and administrative staff, whose reliability and kindness made a world of difference.

Finally, to my family: your unwavering support, patience, and belief in me have sustained me throughout this journey. In moments of doubt and difficulty, your presence—whether near or far—offered strength and reassurance. Your encouragement provided the resolve to persevere, and your steadfast faith reminded me of my ability to overcome challenges. This accomplishment is not mine alone, it is a testament to your love, your sacrifices, and your faith in me.

I am endlessly grateful, and I share this achievement with all of you.